

## **Copyright Warning & Restrictions**

The copyright law of the United States (Title 17, United States Code) governs the making of photocopies or other reproductions of copyrighted material.

Under certain conditions specified in the law, libraries and archives are authorized to furnish a photocopy or other reproduction. One of these specified conditions is that the photocopy or reproduction is not to be “used for any purpose other than private study, scholarship, or research.” If a user makes a request for, or later uses, a photocopy or reproduction for purposes in excess of “fair use” that user may be liable for copyright infringement,

This institution reserves the right to refuse to accept a copying order if, in its judgment, fulfillment of the order would involve violation of copyright law.

**Please Note: The author retains the copyright while the New Jersey Institute of Technology reserves the right to distribute this thesis or dissertation**

Printing note: If you do not wish to print this page, then select “Pages from: first page # to: last page #” on the print dialog screen

The Van Houten library has removed some of the personal information and all signatures from the approval page and biographical sketches of theses and dissertations in order to protect the identity of NJIT graduates and faculty.

## **ABSTRACT**

### **MITOCHONDRIA IMAGING AND TARGETED CANCER TREATMENT**

**by**  
**Tinghan Zhao**

Mitochondria are essential organelles as the site of respiration in eukaryotic cells and are involved in many crucial functions in cell life. Dysfunction of mitochondrial metabolism and irregular morphology have been frequently found in human cancers. The capability of imaging mitochondria as well as regulating their microenvironment is important both scientifically and clinically. Mitochondria penetrating peptides (MPPs), certain peptides that are composed of cationic and hydrophobic amino acids, are good candidates for mitochondria targeting. Herein, a novel MPP, D-arginine-phenylalanine-D-arginine-phenylalanine-D-arginine-phenylalanine-NH<sub>2</sub> (rFrFrF), is conjugated with a rhodamine-based fluorescent chromophore (TAMRA). The TAMRA-rFrFrF probe exhibits advantageous properties for long-term mitochondria tracking of up to three days with low cytotoxicity and high biocompatibility. Mitochondria isolation experiments further confirmed the mitochondria targeting of the TAMRA-rFrFrF probe with minimal perturbation of mitochondrial function.

Mitochondrial function and metabolism are centrally involved in cancer initiation, tumorigenesis, growth, survival, and metastasis. Dysfunction of mitochondria, especially mitochondrial membrane hyperpolarization, plays a key role in drug resistance during cancer treatment. We report a boron-dipyrromethene (BODIPY) triarylsulfonium-based molecule (BD-PAG) as an opto-biomodulator (MOB) to target mitochondria and modulate mitochondrial pH. Significantly, our BD-PAG MOB demonstrates the

reduction of drug resistance in cancer cell lines by regulating the mitochondrial pH and depolarizing the mitochondrial membrane.

**MITOCHONDRIA IMAGING AND  
TARGETED CANCER TREATMENT**

**by  
Tinghan Zhao**

**A Dissertation  
Submitted to the Faculty of  
New Jersey Institute of Technology  
in Partial Fulfillment of the Requirements for the Degree of  
Doctor of Philosophy in Chemistry**

**Department of Chemistry and Environmental Science**

**December 2019**

Copyright © 2019 by Tinghan Zhao

ALL RIGHTS RESERVED

**APPROVAL PAGE**

**MITOCHONDRIA IMAGING AND  
TARGETED CANCER TREATMENT**

**Tinghan Zhao**

---

Dr. Kevin D. Belfield, Dissertation Advisor Date  
Dean of College of Science and Liberal Art, and Professor of Chemistry and  
Environmental Science, NJIT

---

Dr. James Haorah, Committee Member Date  
Associate Professor of Biomedical Engineering, NJIT

---

Dr. Yong I. Kim, Committee Member Date  
Assistant Professor of Chemistry and Environmental Science, NJIT

---

Dr. Mengyan Li, Committee Member Date  
Assistant Professor of Chemistry and Environmental Science, NJIT

---

Dr. Yuanwei Zhang, Committee Member Date  
Assistant Professor of Chemistry and Environmental Science, NJ

## BIOGRAPHICAL SKETCH

**Author:** Tinghan Zhao  
**Degree:** Doctor of Philosophy  
**Date:** December 2019

### Undergraduate and Graduate Education:

- Doctor of Philosophy in Chemistry, New Jersey Institute of Technology, Newark, NJ, 2019
- Master of Medicine in Surgery, China Medical University, Shenyang, Liaoning, China, 2015
- Bachelor of Medicine in Clinical Medicine, Capital Medical University, Beijing, China, 2010

**Major:** Chemistry

### Presentations and Publications:

Sambath K.; Zhao T.; Wan Z.; Zhang Y. Photo-uncaging of BODIPY oxime ester for histone deacetylases induced apoptosis in tumor cells. *Chem. Commun.* **2019**, DOI: 10.1039/c9cc07199g.

Zhao T.; Liu X.; Singh S.; Liu X.; Zhang Y.; Sawada J.; Komatsu M.; Belfield K. D. Mitochondria penetrating peptide-conjugated TAMRA for live-cell long-term tracking. *Bioconjug. Chem.* **2019**, *30*, 2312-2316.

Zhao T.; Singh S.; Zhang Y.; Belfield K. D. Novel mitochondria penetrating peptide for live-cell long-term tracking of mitochondria. *Optics in the Life Sciences Congress 2019*, OSA Optical Molecular Probes, Imaging and Drug Delivery, paper OM3D.5

Song S.; Cheng J.; Liu N.; Zhao T. Diagnosis and treatment of pancreatic metastases in 22 patients: a retrospective study. *World J. Surg. Oncol.* **2014**, *12*, 299

## ACKNOWLEDGMENT

First of all, I want to give special thanks to my advisor, Kevin Belfield. He is not only the academic advisor for me, but also the source of support, inspiration, and power to me. During my Ph.D study, Dr. Belfield gave me so much help and guidance in research. Besides, he encouraged me to participate in so many great conference and scientific events, and he would never hesitate to give good reference for me at any time. In summary, Dr. Belfield's exceptional enthusiasm and positive attitude towards research was the driving forces of my graduate career at New Jersey Institute Technology, and I would not be able to finish my doctoral study without his help.

I want to also thank every member in my Committee for their patience, professional advice and help: Dr. Yuanwei Zhang, Dr. Yong Kim, Dr. Mengyan Li and Dr. James Haorah. Especially Dr. Yuanwei Zhang, is more than a mentor to me. He helped me with all my projects. He passed on his knowledge and experience to me without conditions. I also appreciate the National Science Foundation for the funding and support for my research.

During my doctoral study, members in our group became my best partners. We belong to a friendly and united group. I highly believe that even after graduation, we will still be good friends for our whole life. Sweety Singh, Mehruh Nahar Uddin, Xiangshan Liu, Zhangxiong Wan, Jie Dou, Shupei Yu and former members Dr. Xinglei Liu, they all helped me a lot not only on research but also in my life. Especially Dr. Xinglei Liu, taught so many tricks and skills, that I could not learn from books or classes. I will remember everyone in this lab; those who helped me and supported me during the last four and half years.

Last, but not the least, my parents and wife are my strongest backers. I appreciate their understanding, support and unconditional love for me. I would not have such a wonderful life without them. And I will try my best to pay back their love.

## TABLE OF CONTENTS

Chapter	Page
1 INTRODUCTION.....	1
1.1 Introduction of Mitochondria.....	1
1.1.1 Mitochondria.....	1
1.1.2 Morphology of Mitochondria.....	2
1.2 Function of Mitochondria.....	4
1.2.1 Bioenergetic Metabolism.....	4
1.2.2 Regulation of Cell Death Signaling.....	5
1.2.3 ROS Generation.....	6
1.3 Mitochondria and Cancer .....	6
2 MITOCHONDRIA PENETRATING PEPTIDE FOR LIVE- CELL LONG-TERM TRACKING.....	8
2.1 Introduction.....	9
2.2 Experimental Section.....	12
2.2.1 Material and Peptide Synthesis.....	12
2.2.2 Photophysical Properties Measurements.....	12
2.2.3 Cell Culture.....	12
2.2.4 Cell Viability.....	13
2.2.5 Oxygen Consumption Rate (OCR) Measurement.....	14
2.2.6 Colocalization Study.....	14
2.2.7 Mitochondria Uptake Measurement.....	15

**TABLE OF CONTENTS**  
**(Continued)**

<b>Chapter</b>	<b>Page</b>
2.3 Results and Discussion.....	16
2.3.1 Cell Viability.....	16
2.3.2 Cellular Uptake and Colocalization.....	17
2.3.3 Time Dependent Colocalization.....	20
2.3.4 Isolated Mitochondria Uptake.....	28
2.3.5 Oxygen Consumption Rate (OCR).....	31
2.4 Conclusion.....	32
<b>3 MITOCHONDRIAL PH REGULATING AND THE ROLE IN REDUCING DRUG RESISTANCE.....</b>	<b>33</b>
3.1 Introduction.....	34
3.2 Results and Discussion.....	36
3.2.1 Cell Viability.....	36
3.2.2 Cellular Uptake and Colocalization.....	38
3.2.3 Mitochondrial pH.....	40
3.2.4 Mitochondrial Membrane Potential.....	41
3.2.5 Irradiation Time Dependent Time Lapse Cell Imaging.....	42
3.2.6 Caspase 3/9 Assay.....	44
3.2.7 Combined Drug Therapy.....	45
3.3 Materials and Methods.....	46
3.3.1 Materials and General Equipments.....	48

**TABLE OF CONTENTS**  
**(Continued)**

<b>Chapter</b>	<b>Page</b>
3.3.2 Cell Culture.....	48
3.3.3 Dark Cell Viability.....	48
3.3.4 Time Dependent Cell Viability and Combined drug therapy.....	49
3.3.5 Cellular Uptake and Colocalization .....	50
3.3.6 Mitochondrial pH Measurement.....	50
3.3.7 Mitochondrial Membrane Potential Measurement.....	51
3.3.8 Time Lapse and Z-stack Cell Imaging.....	51
3.3.9 Caspase 3 and Caspase 9 measurements.....	52
3.4 Conclusion.....	52
<b>4 PHOTO-UNCAGING OF BODIPY OXIME EASTER FOR HISTONE DEACETYLASES INDUCED APOPTOSIS IN TUMOR CELLS.....</b>	<b>54</b>
4.1 Introduction.....	54
4.2 Results and Discussion.....	57
4.2.1 Synthetic Strategy.....	57
4.2.2 Photophysical Properties.....	58
4.2.3 Photolysis Analysis.....	64
4.2.4 Cellular Uptake and Cell Imaging.....	65
4.2.5 Dark Cell Viability and Photo-toxicity.....	66
4.3 Methods.....	69
4.3.1 Materials.....	69

**TABLE OF CONTENTS**  
**(Continued)**

<b>Chapter</b>	<b>Page</b>
4.3.2 Synthesis of BODIPY Core.....	70
4.3.3 Synthesis of BODIPY Aldehyde (1).....	71
4.3.4 Synthesis of BODIPY-oxime Parent Compound (2).....	73
4.3.5 Synthesis of BODIPY Oxime Esters (3a, 3b).....	74
4.3.6 Photophysical Property Measurement.....	78
4.3.7 Preparative Photolysis.....	81
4.3.8 Cell Culture and Cellular Uptake.....	81
4.3.9 Cell Viability and Photolysis Cytotoxicity.....	82
4.4 Conclusion.....	83
REFERENCES.....	85

## LIST OF TABLES

<b>Table</b>	<b>Page</b>
4.1 Photophysical Properties for Compound <b>3a</b> and <b>3b</b> .....	59

## LIST OF FIGURES

<b>Figure</b>	<b>Page</b>
1.1 Structure of mitochondria.....	2
1.2 Mitochondria fission and fusion.....	3
1.3 Mitochondria TCA cycle.....	5
2.1 Molecular structure and spectra.....	11
2.2 Molecular structure of TAMRA-rFrFrF and mitochondria penetration.....	11
2.3 Cell viability of HeLa cells.....	16
2.4 Cell viability of LLC-PK1 cells.....	17
2.5 Cell viability of HeLa cells treated with Mitotracker Green and Red.....	17
2.6 Cellular uptake imaging .....	18
2.7 Colocalization of LT Green.....	19
2.8 Colocalization of ER Green.....	20
2.9 Time dependent HeLa cell colocalization.....	23
2.10 Time dependent LLC-PK1 cell colocalization.....	25
2.11 Time dependent MT-Green cell imaging.....	26
2.12 Time dependent cell imaging.....	27
2.13 HeLa cells mitochondria uptake TAMRA-rFrFrF measurement.....	29
2.14 LLC cells mitochondria uptake TAMRA-rFrFrF measurement.....	30
2.15 Oxygen consumption rates.....	31
3.1 Molecular structure and spectra.....	35
3.2 Dark cell viability.....	36

## LIST OF FIGURES

Figure	Page
3.3 Irradiation time dependent cell viability of HeLa cells.....	37
3.4 Irradiation time dependent cell viability of MCF-7 cells.....	37
3.5 Cellular uptake image.....	38
3.6 Colocalization of BD-PAG in HeLa cells.....	39
3.7 Colocalization of BD-PAG in MCF-7 cells.....	39
3.8 Mitochondrial pH in HeLa cell.....	40
3.9 Mitochondrial membrane potential in HeLa cell.....	41
3.10 20 $\mu$ M of BD-PAG treated time lapse cell imaging.....	42
3.11 Time lapse and Z-stack cell imaging.....	43
3.12 Irradiation time dependent caspase 3/9 assay.....	45
3.13 Irradiation time dependent combined drug therapy on HeLa cells.....	46
3.14 Irradiation time dependent combined drug therapy on MCF-7 cells.....	47
4.1 Schematic representation.....	56
4.2 Synthesis route of BODIPY oxime ester <b>3a</b> and <b>3b</b> .....	58
4.3 Normalized absorption and emission spectra of compound <b>3a</b> and <b>3b</b> .....	59
4.4 UV-Vis spectra of photorelease from compound <b>3a</b> and <b>3b</b> .....	60
4.5 LC-MS profile of time-dependent photo-uncaging <b>3a</b> .....	62
4.6 $^1\text{H}$ NMR spectra of <b>3a</b> , 2-cyano-BODIPY photo-byproduct.....	62
4.7 $^1\text{H}$ , $^{13}\text{C}$ NMR and Mass spectra of 2-cyano-BODIPY photo-byproduct.....	64

## LIST OF FIGURES

Figure	Page
4.8 Time course of photolysis for the oxime ester <b>3a</b> .....	65
4.9 Possible photo-uncaging mechanism of N-O bond cleavage of <b>3a</b> .....	65
4.10 Cellular uptake image.....	66
4.11 Dark and photo-toxicity.....	68
4.12 Photo-toxicity of 2-cyano-BODIPY.....	69
4.13 <sup>1</sup> H NMR of BODIPY core compound.....	71
4.14 <sup>13</sup> C NMR of BODIPY core compound.....	71
4.15 <sup>1</sup> H NMR of aldehyde BODIPY compound <b>1</b> .....	72
4.16 <sup>13</sup> C NMR of aldehyde BODIPY compound <b>1</b> .....	72
4.17 MS spectrum of aldehyde BODIPY compound .....	73
4.18 <sup>1</sup> H NMR of BODIPY compound <b>2</b> .....	74
4.19 <sup>13</sup> C NMR of BODIPY compound <b>2</b> .....	74
4.20 <sup>1</sup> H NMR of BODIPY compound <b>3a</b> .....	75
4.21 <sup>13</sup> C NMR of BODIPY compound <b>3a</b> .....	76
4.22 MS spectrum of BODIPY compound <b>3a</b> .....	76
4.23 <sup>1</sup> H NMR of BODIPY compound <b>3b</b> .....	77
4.24 <sup>13</sup> C NMR of BODIPY compound <b>3b</b> .....	78

# CHAPTER 1

## INTRODUCTION

### 1.1 Introduction of Mitochondria

#### 1.1.1 Mitochondria

Mitochondria are double-membrane-bound essential organelles, serving as the site of respiration within eukaryotic cells that generate ATP from energy-rich molecules.<sup>1</sup> Mitochondrial structures are comprised of four compartments; outer membrane, inner boundary membrane, intermembrane space, and matrix.<sup>2</sup> The outer mitochondrial membrane (OMM) is porous and freely traversed by ions and small molecules through pore-forming membrane proteins (porins), that separates the inside of the organelle from the cytoplasm. The inner mitochondrial membrane (IMM) possesses a several-fold larger surface than the outer membrane, resulting in an invaginated membrane and the cristae that harbors the oxidative phosphorylation enzyme complex. The oxidative phosphorylation enzyme complex is a series of enzymes forming an electron transport chain (ETC) to transfer electrons from electron donors to electron acceptors via redox reactions, and couples this electron transfer with the transfer of protons across the membrane to facilitate the synthesis of adenosine triphosphate (ATP).

Due to the porosity of OMM and the ion selectivity of ETC, an electrochemical membrane potential of about -180 mV builds up across the inner mitochondrial membrane. The mitochondrial matrix is more viscous than cytoplasm, and contains a mixture of enzymes, special mitochondrial ribosomes, tRNA, and several copies of the mitochondrial DNA genome. The major functions of enzymes present in the matrix are

oxidation of pyruvate and fatty acids, and the citric acid cycle, which is the synthesis of ATP.<sup>3-9</sup>

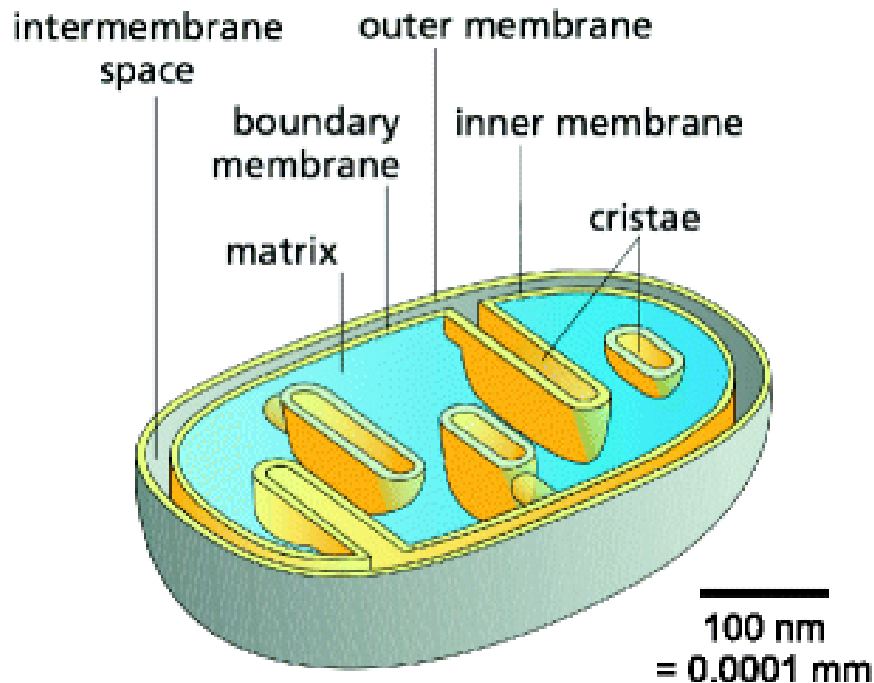


**Figure 1.1** Structure of mitochondria.

*Source: Kühlbrandt, W. BMC Biol. 2015, 13, 89.*

### 1.1.2 Morphology of Mitochondria

Mitochondrial morphologies vary widely in different cell types or cell conditions. Fibroblast mitochondria, for example, are usually long filamentous-like, whereas hepatocyte mitochondria are more uniformly punctate-like.<sup>10, 11</sup> Their shapes change continually through the combined actions of fission, fusion, and degradation. Mitochondria are highly dynamic and can change in number and morphology within a cell during development, the cell cycle, and even when exposed to various toxic conditions. These dynamic processes are critical for maintaining a healthy functional mitochondrial network.<sup>12, 13</sup>

Mitochondrial fission and fusion processes are both mediated by guanosine triphosphatases (GTPases) in the dynamin family that divide and fuse the two lipid bilayers that surround mitochondria.<sup>14</sup> Fission is mediated by a cytosolic dynamin family member (Drp1), recruited from the cytosol to form spirals around mitochondria that constrict to sever both inner and outer membranes. Fusion between OMMs is mediated by membrane-anchored dynamin family members Mfn1 and Mfn2, whereas fusion between IMM is mediated by a single dynamin family member Opa1.<sup>15-17</sup> Mitochondrial fission is critical for maintaining adequate mitochondria during cell growth and division. Mitochondrial fusion is not essential for cell life, however it is essential for cell development.<sup>18, 19</sup>

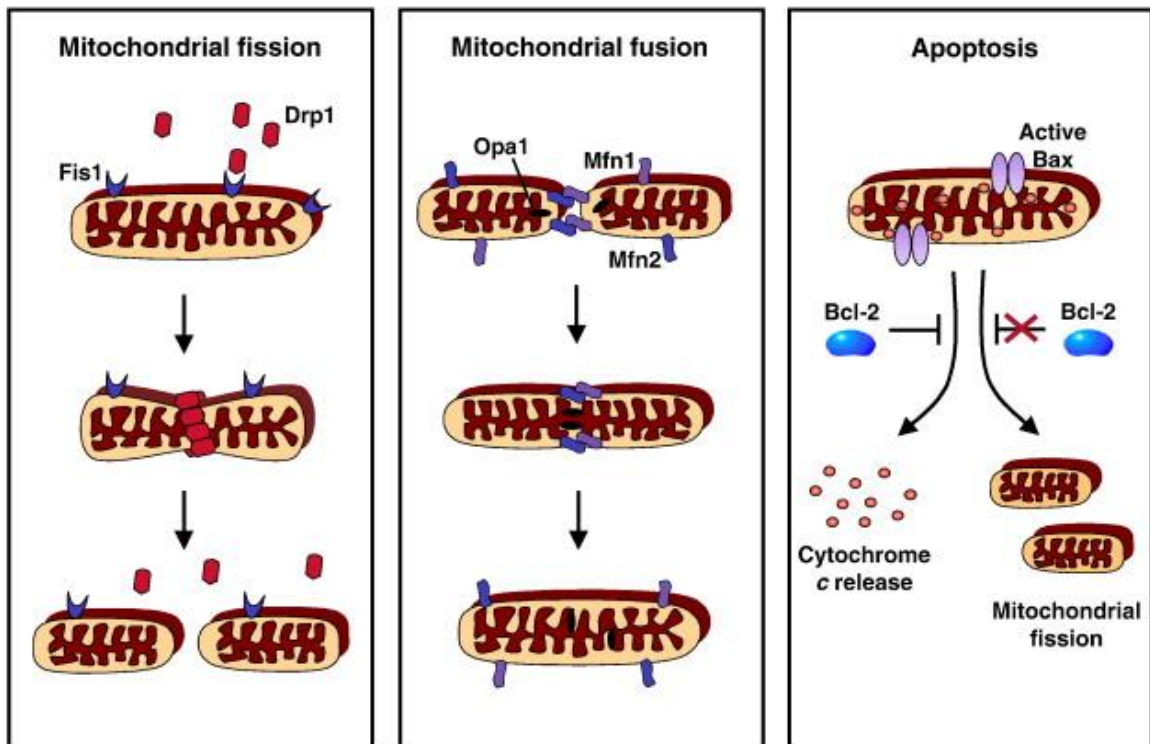


**Figure 1.2** Mitochondria fission and fusion.

Source: Sheridan, C.; Martin, S. J. *Mitochondrion* 2010, 10, 640-8.

## 1.2 Function of Mitochondria

### 1.2.1 Bioenergetic Metabolism

The most prominent roles of mitochondria are to produce the energy currency of the cell, ATP, through respiration, and to regulate cellular metabolism. The main reactions involved in ATP production are tricarboxylic acid (TCA) cycle, which occurs in the mitochondrial matrix. Pyruvate is actively transported across the inner mitochondrial membrane after undergoing glycolysis in the cytosol, and into the matrix where pyruvate dehydrogenase facilitates its conversion to acetyl-CoA.<sup>20, 21</sup>

In the TCA cycle, the acetyl group of acetyl-CoA is transferred to oxaloacetate, forming citrate. In a series of enzymatic steps, citrate is oxidized back to oxaloacetate, with the excess carbon carried away as two molecules of carbon dioxide, and the electrons removed in the process passed to the cofactors nicotinamide adenine dinucleotide (NADH) and flavin adenine dinucleotide (FADH<sub>2</sub>). Meanwhile the free energy liberated is carried by NADH and FADH<sub>2</sub> to the mitochondrial ETC. All the intermediates such as citrate, iso-citrate, alpha-ketoglutarate, succinate, fumarate, malate, and oxaloacetate are regenerated during each turn of the cycle.<sup>22, 23</sup>

In the ETC, electrons removed from the TCA cycle by NADH and FADH<sub>2</sub> are used to power the pumping of protons from the matrix to the intermembrane space, generating a potential difference across the inner mitochondrial membrane. This potential difference is ultimately used to power the synthesis of ATP in the final step of oxidative phosphorylation (OXPHOS).<sup>24, 25</sup>

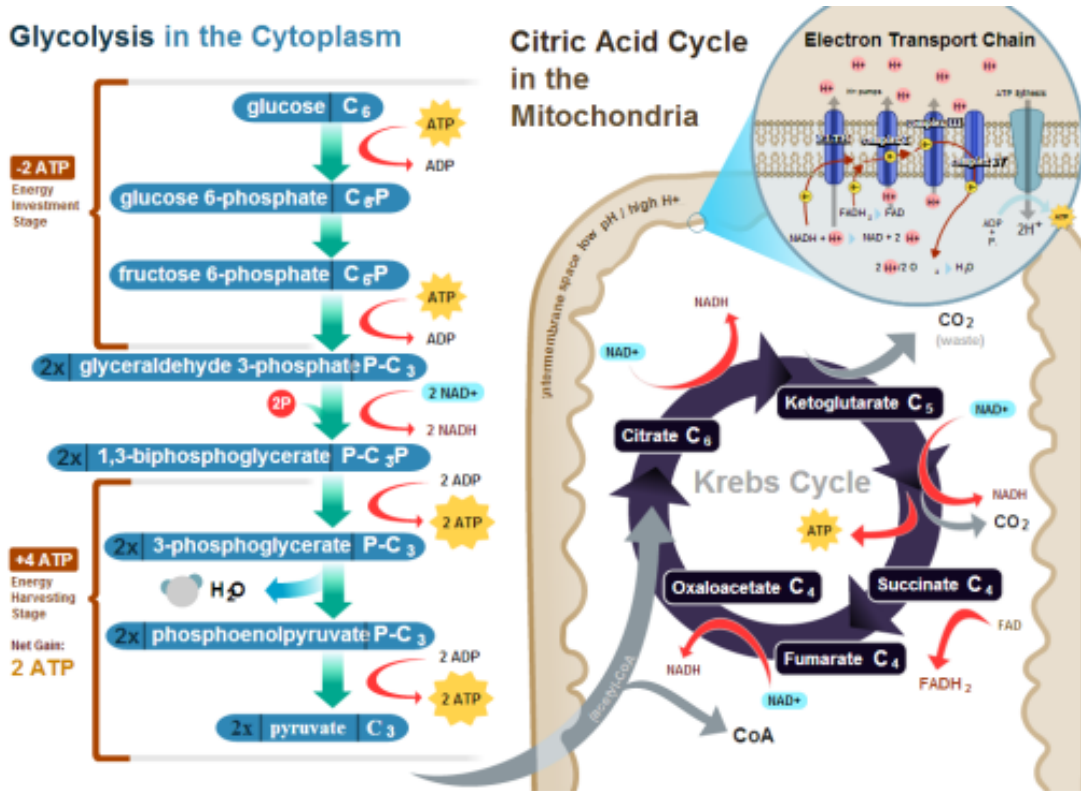


**Figure 1.3** Mitochondria TCA cycle.

Source: <https://biochemistry3rst.wordpress.com/category/tca-etc/> accessed on 12/8/19

### 1.2.2 Regulation of Cell Death Signaling

Apoptosis is programmed cell death that occurs in multicellular organisms. Mitochondria have been recognized as playing a central role in apoptotic cell death.<sup>26, 27</sup> The integrity of the OMM is strictly regulated through interactions of members of the B-cell lymphoma 2 (Bcl-2) protein family which is classified into two groups, pro-survival (Bcl-xL, Bcl-w, A1 and Mcl-1) and pro-apoptotic (Bax, Bak, Bok, Bid, Bim, Bad, Noxa and Puma). In the intrinsic (mitochondrial) pathway of apoptosis, pro-apoptotic stimuli such as DNA damage lead to the activation of two key Bcl-2 family proteins, Bax and Bak. Activation of Bax and Bak cause a reinforcement mitochondrial outer membrane permeability (MOMP), which releases cytochrome c from intermembrane space into

cytoplasm where it promotes activation of a caspase cascade.<sup>28-30</sup> Once cytochrome c is released into the cytoplasm, it binds with apoptotic protease activating factor – 1 (Apaf-1) and ATP, which then binds to pro-caspase-9 to create a protein complex known as an apoptosome. The apoptosome cleaves the pro-caspase-9 to its active form of caspase-9, which in turn activates caspase-3 and 7 to complete the apoptotic process.<sup>31, 32</sup>

### **1.2.3 ROS Generation**

Reactive oxygen species (ROS) are chemically reactive species containing oxygen, which include peroxides, superoxide, hydroxyl radical, and singlet oxygen. ROS is formed as a natural byproduct of the normal metabolism of oxygen, where mitochondrial ETC is one of the major sites that generate ROS during the TCA cycle. Leakage of electrons at complex I and complex III from ETC leads to partial reduction of oxygen to form superoxide. Subsequently, superoxide is quickly dismutated to hydrogen peroxide by two superoxide dismutases, then H<sub>2</sub>O<sub>2</sub> is released to cytoplasm. Mitochondria also contain antioxidant mechanisms to remove ROS. At low levels, ROS act as important signaling molecules and potent mitogens, whereas higher levels can lead to pathological oxidative damage to mitochondria and cells.<sup>33-35</sup>

## **1.3 Mitochondria and Cancer**

Mitochondria are bioenergetic, biosynthetic, and signaling organelles whose dysfunction of metabolism and/or morphology has been related to tumorigenesis, proliferation, invasion, migration, and metastasis.<sup>36</sup> Cancer cells often exhibit fragmented mitochondria, with high expression or enhanced activation of Drp1 and/or downregulation of Mfn2, leading to constant mitochondrial fission. The mitochondrial

fission asymmetrically generates one depolarized and one hyperpolarized mitochondrion, in which the hyperpolarized mitochondrion can be reintroduced into the healthy mitochondrial network with reduced MOMP and apoptosis.<sup>37, 38</sup> This mitochondrial fragmentation is caused by an unlimited proliferation, resulting in an hypoxic environment. Interestingly, hypoxia is considered a major driver of metabolic reprogramming, cancer progression, and metastasis.<sup>39</sup>

In cancer cells, mitochondria play an alternative metabolism due to the hypoxia, which cancer cells reprogram with the use of catabolic molecules, glucose and glutamine, via signaling pathways containing known oncogenes, including Myc and tumor suppressors. These signaling pathways regulate glucose toward aerobic glycolysis—the so-called Warburg effect, and glutamine toward glutaminolysis for the purpose of producing amino acids, nucleotides, and lipids that are essential for rapid proliferation.<sup>40</sup>

<sup>41</sup> The altered metabolism of cancer cells raises the production of ROS, which are formed as a signaling molecules to promote cell proliferation as mitogens.

## CHAPTER 2

### MITOCHONDRIA PENETRATING PEPTIDE FOR LIVE- CELL LONG-TERM TRACKING

Mitochondria are essential targets for treatment of diseases with mitochondrial disorders such as diabetes, cancer, cardiovascular, and neurodegenerative disease. Mitochondria penetrating peptides (MPPs) are composed of cationic and hydrophobic amino acids that can target and permeate the mitochondrial membrane. With the objective of developing new mitochondria penetrating peptides and long-term tracking of mitochondria, a novel D-arginine-phenylalanine-D-arginine-phenylalanine-D-arginine-phenylalanine-NH<sub>2</sub> (rFrFrF) peptide was conjugated with a rhodamine-based fluorescent chromophore, carboxy-tetramethylrhodamine (TAMRA). This new probe (TAMRA-rFrFrF) exhibited advantageous properties for long-term mitochondria tracking as demonstrated by fluorescence microscopy and analyzed by the Pearson's correlation coefficient. Cell viability assays and oxygen consumption rates indicated low cytotoxicity and high biocompatibility of the new contrast agent. Time dependent colocalization studies and isolated mitochondria uptake measurement were performed with a long-term period, which suggest that TAMRA-rFrFrF is a promising candidate for mitochondrial tracking for up to 3 days.

## 2.1 Introduction

Mitochondria are essential organelles as the site of respiration in eukaryotic cells and are involved in multiple functions in cell life, such as energy supply, cell cycle and growth, cell signaling pathways and apoptosis, cell proliferation, and metabolism.<sup>42, 43</sup> Meanwhile, these organelles are dynamic and continually undergo fusion, fission, transport, and degradation. These processes are critical for maintaining a healthy, functional mitochondrial network.<sup>44, 45</sup> Dysfunctions of mitochondrial metabolism and/or morphologies have been re-reported in human cancers as well as cardiovascular and neurodegenerative diseases. Thus, the capability of monitoring mitochondrial morphology is important in both scientific and clinical research.<sup>46-48</sup> However, due to their continuously moving and changing morphology, monitoring mitochondria morphological changes and dynamics over prolonged times is still difficult, and so far the longest reported time for live cell mitochondria imaging is 24 h.<sup>49, 50</sup> Therefore, a long-term tracking strategy would be helpful for studying mitochondria morphology and prospective drug delivery systems.

Over the last few decades, a variety of mitochondria targeting modules have been developed. Most of those reported are delocalized lipophilic cations, which exhibit relatively high toxicity to mitochondria.<sup>51, 52</sup> Mitochondria penetrating peptides (MPPs) represent a relatively new direction to develop mitochondria targeting vectors, which are short peptides with high mitochondrial uptake. The structure of MPPs is generally cationic and hydrophobic, which facilitates permeation through the hydrophobic mitochondrial membrane and accumulation in the mitochondria matrix.<sup>53-55</sup> Due to their primary peptide structures and bio-compatible properties, MPPs with short amino acid

sequences (fewer than 10 amino acids) are expected to exhibit low cytotoxicity, making them promising candidates for the development of new probes for investigation of mitochondria.<sup>56-58</sup>

Recently, MPPs were employed for targeting and delivering therapeutic cargos into mitochondria with high efficiency.<sup>51, 53, 55-59</sup> Peptides such as (FxrFxrFxr) (r is D-arginine and Fx is cyclohexylalanine) exhibited low cytotoxicity and high mitochondria targeting.<sup>57</sup> Although numerous MPPs have been developed to deliver fluorescent dyes, drugs and other cargos to mitochondria, there are no reports for long-term mitochondrial tracking thus far, possibly due to their low serum stability.<sup>60</sup>

Herein, we report a peptide containing six amino acid residues (Figure 2.1a), D-arginine-phenylalanine-D-arginine-phenylalanine-D-arginine-phenylalanine-NH<sub>2</sub> (rFrFrF), conjugated to a rhodamine-derived fluorescent probe (TAMRA)<sup>61</sup> (Figure 2.1b and Figure 2.2), and studies of the resulting probe, TAMRA-rFrFrF, in time-dependent mitochondria targeting and imaging. Unnatural D-arginine (r) in the first and third positions was selected to provide positive charges, minimize amino peptidase degradation, and increase serum-stability.<sup>62</sup> The natural amino acid phenylalanine (F) residue, which has a hydrophobic side group, was selected to tune the hydrophobicity and impart low cytotoxicity. This prospective MPP sequence possesses three positive charges with a balance of hydrophilicity and hydrophobicity designed to reduce potential disruptions to mitochondrial activity and maintain normal mitochondrial functions.<sup>63, 64</sup> Moreover, the amidated C-terminus was designed to increase structural stability and attenuate hydrolysis.<sup>65</sup>

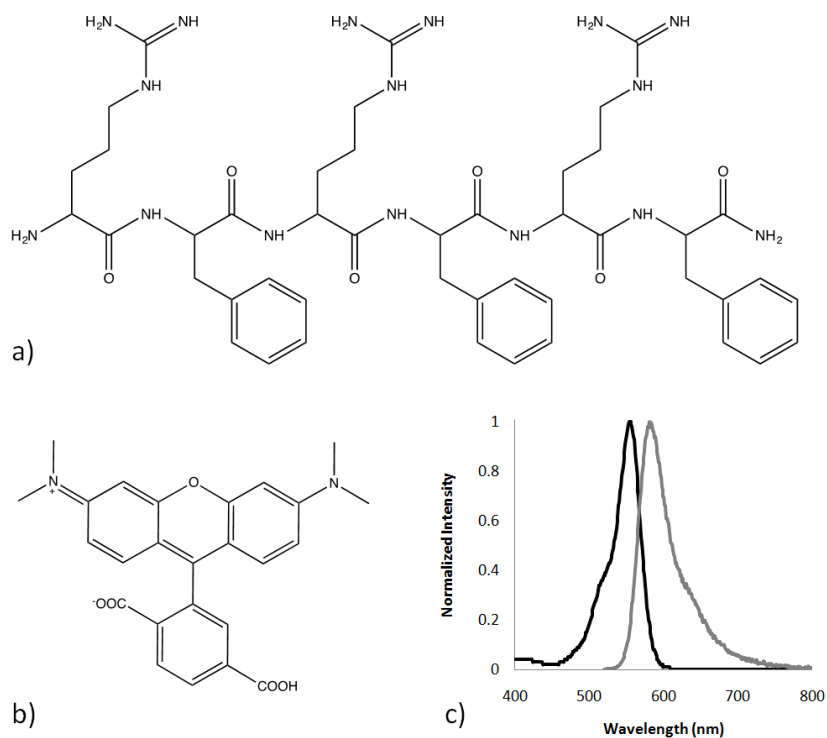


**Figure 2.1** Molecular structure and spectra. a) Molecular structure of unconjugated rFrFrF, b) molecular structure of TAMRA, c) normalized absorption and emission spectra of TAMRA-rFrFrF in PBS.

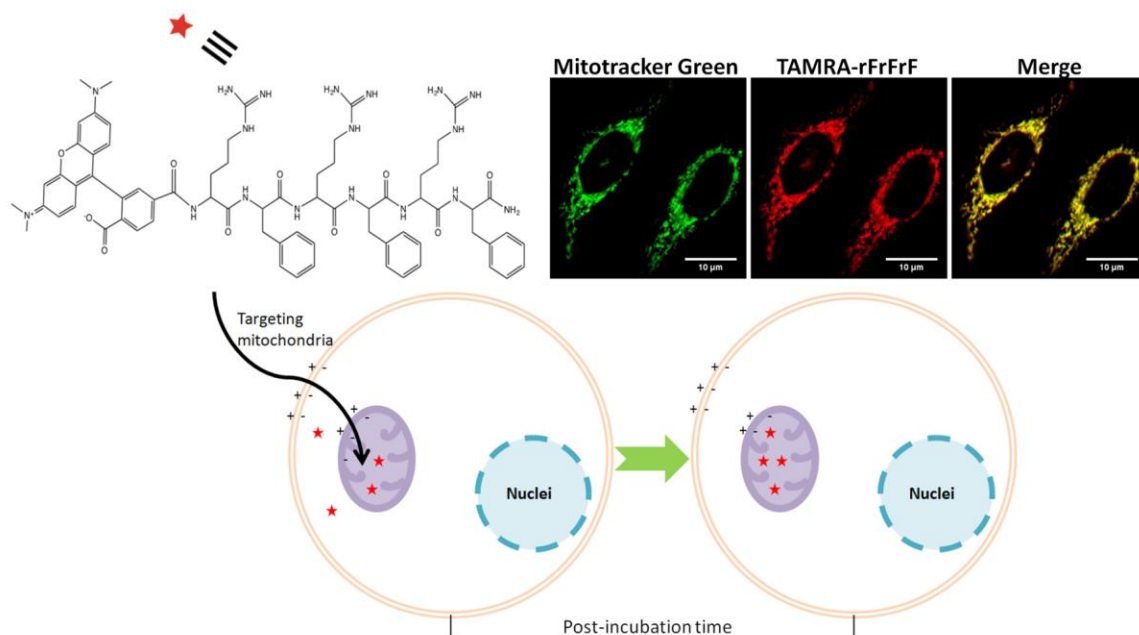


**Figure 2.2** Molecular structure of TAMRA-rFrFrF and mitochondria penetration.

## 2.2 Experimental Section

### 2.2.1 Material and Peptide Synthesis

All peptides and 6-(tetramethylrhodamine-5-(and-6)-carboxamido) hexanoic acid conjugates D-arginine-phenylalanine-D-arginine- phenylalanine- D-arginine-phenylalanine-NH<sub>2</sub> (rFrFrF) (TAMRA-rFrFrF), following design in our lab, were synthesized and purified by AnaSpec, EGT Corporation (Fremont, CA, USA). All other chemical reagents were purchased from Fisher Scientific, and used as received unless otherwise noted. Carbon dioxide (99.9% purity) was purchased from Airgas. All reagents and solvents were purchased from commercial suppliers and used without further purification.

### 2.2.2 Photophysical Properties Measurements

Linear absorption, fluorescence, and excitation spectra of TAMRA and TAMRA-rFrFrF were investigated in PBS at room temperature. The absorption spectra were measured with a Tecan Infinite M200 PRO plate reader spectrometer in 1 cm path length quartz cuvettes. The fluorescence and excitation spectra were obtained using an Edinburgh Instruments FLS980 fluorescence spectrometer.

### 2.2.3 Cell Culture

Human cervical cancer HeLa and pig normal kidney LLC-PK1 cell lines were cultured in Dulbecco's Modified Eagle Medium (DMEM) supplemented with 10% fetal bovine serum, 1% penicillin/streptomycin at 37 °C in a humidified 5% CO<sub>2</sub> incubator.

## 2.2.4 Cell Viability

To assess the cytotoxicity of unconjugated-rFrFrF and TAMRA-rFrFrF, HeLa and LLC-PK1 cells were cultured in DMEM cell medium supplemented with 10% fetal bovine serum, 1% penicillin, and streptomycin at 37 °C and 5% CO<sub>2</sub>. Cells were placed in 96 well plates and incubated until there were no fewer than  $5 \times 10^3$  cells per well for the experiments. Next, cells were incubated with different concentrations of rFrFrF (1, 2.5, 5, 10, 20, 40, and 80  $\mu$ M) and TAMRA-rFrFrF (1, 2.5, 5, 10, 20, 40, and 80  $\mu$ M) for an additional 22 h, where the values within parentheses refer to the nominal concentrations of the peptides. After that, 20  $\mu$ L of the CellTiter 96 Aqueous One solution reagent (for MTS assay) was added into each well, followed by further incubation for 2 h at 37 °C.

Cytotoxicities of Mitotracker Green and Red was performed same procedure as unconjugated-rFrFrF and TAMRA-rFrFrF in HeLa cells with a various concentration of (0.1, 0.25, 0.5, 1, 2, 4, 8, and 16  $\mu$ M).

The respective absorbance values were recorded with a Tecan Infinite M200 PRO plate reader spectrometer at 490 nm. Cell viabilities were calculated on the basis of the following equation,

$$Cell\ Viability(\%) = \frac{Abs^s_{490nm} - Abs^D_{490nm}}{Abs^c_{490nm} - Abs^{D2}_{490nm}} \times 100\% \quad (2.1)$$

where  $Abs^s_{490nm}$  is the absorbance of the cells incubated with different concentrations of experimental probe solutions,  $Abs^D_{490nm}$  is the absorbance of cell-free well containing only dye at the concentration that was studied,  $Abs^c_{490nm}$  is the absorbance of cells alone incubated in the medium, and  $Abs^{D2}_{490nm}$  is the absorbance of the cell-free well.

### **2.2.5 Oxygen Consumption Rate (OCR) Measurement**

Oxygen consumption rates were measured for HeLa cells by using Seahorse XFe96 Analyzer (Agilent, Santa Clara, CA, US). HeLa cells were placed in 96 well Seahorse XF96 cell culture plates at a density of  $2 \times 10^4$  cells/well, and incubated DMEM supplemented with 10% fetal bovine serum, 1% penicillin, and streptomycin at 37 °C and 5% CO<sub>2</sub> for 16 h. Next, to the cells were added 5 μM TAMRA-rFrFrF (in 1mM DMSO stock solution) for 6 h. A negative control was treated with DMSO only. After washing out TAMRA-rFrFrF, cells were incubated with XF Assay Medium for 1 h. Measurement of OCR was performed at baseline and following sequential injections of a) 1 μM oligomycin, (final conc. 0.8 μg/mL) (20 μL of 10 drops), an ATP synthase inhibitor, b) final conc. 2 μM FCCP (22 μL of 10 drops), a mitochondrial uncoupler, and c) 0.5 μM Rotenon + 0.5 μM antimycin A, (25 μL of 10 drops), a complex III and complex I inhibitor, respectively. This enabled the measurement of the OCR coupled to ATP production, as well as the maximal and the mitochondrial OCR, respectively.<sup>66</sup>

### **2.2.6 Colocalization Study**

To investigate the efficiency and specificity of TAMRA-rFrFrF, HeLa and LLC-PK1 cells were employed. All cells were seeded on confocal dish (MatTek) at the density of  $4 \times 10^4$  cells per dish and incubated for 24 h at 37 °C. Stock solutions of TAMRA, rFrFrF, and TAMRA-rFrFrF dissolved in DMSO were prepared at a nominal concentration of 10<sup>4</sup> μM. The stock solution was diluted to 5 μM with the DMEM respectively and freshly placed over cells for a 1.5 h incubation period. Cells were washed three times with PBS and then post-incubated with fresh medium at 37 °C for various time periods (0 h, 1 h, 2 h, 3 h, 4 h, 6 h, 8 h, 12 h, 18 h, 1 d, 2 d, and 3 d). After post-incubation, cells were further

incubated with MitoTracker Green (MT Green), Lysotracker Green (LT Green), or ER-tracker Green (ER Green) separately before cell imaging.<sup>67</sup> Cells were then washed with PBS three times, and then the live cell imaging solution (Molecular Probes) was added to confocal dishes. Fluorescence images were obtained using an inverted Olympus IX70 microscope coupled with a FITC filter cube (Ex: 482/40; DM: 506; Em: 534/40) for MT green, LT green, or ER Green, and a Texas Red filter cube (Ex: 562/40; DM: 593; Em: 624/40) for TAMRA or TAMRA-rFrFrF, respectively. Pearson's correlation coefficients for TAMRA and TAMRA-rFrFrF were calculated using Fiji, a freely available image processing software.

To further compare long-term tracking advantage of TAMRA-rFrFrF, incubation time-dependent cell imaging of MT green was performed in HeLa cells. Cells were incubated with 100 nM of MT green for 15 min at 37 °C. Cells were washed three times with PBS and then post-incubated with fresh medium at 37 °C for various time periods (0 h, 1 h, 2 h, 4 h, 6 h and 12 h). After post-incubation, cells were further incubated with 100 nM of Hoechst 33258 for 10 min and washed out with PBS before cell imaging.

### **2.2.7 Mitochondria Uptake Measurement**

To evaluate the uptake of TAMRA-rFrFrF by mitochondria,  $1 \times 10^6$  cells were incubated with 5  $\mu$ M TAMRA-rFrFrF for 1.5 h at 37 °C. After washing twice with PBS, post-incubation was performed at 37 °C for 2 h, 4 h, 6 h, 12 h, 1 d, 2 d, and 3 d. Subsequently, mitochondria were extracted according with a Mitochondria Isolation Kit for cultured cells (Thermo Fisher Scientific, Waltham, MA, US), and diluted to 2 mL using PBS. The fluorescence intensity was measured using an Edinburgh Instruments FLS980

fluorescence spectrometer. Isolated mitochondria with no TAMRA-rFrFrF treatment served as the blank.

## 2.3 Results and Discussion

### 2.3.1 Cell Viability

The cytotoxicity and bio-compatibility of rFrFrF and TAMRA-rFrFrF were evaluated in HeLa and pig kidney (LLC-PK1) cells via an MTS assay (Figure 2.3 and Figure 2.4).<sup>68</sup> The peptide rFrFrF itself did not show any acute toxic effects over a range of concentrations, even at the highest concentration employed of 80  $\mu$ M, cell viability remained at 100% after 24 h incubation. The TAMRA-rFrFrF probe also exhibited very good cell viability with a 90% survival rate at concentrations up to 80  $\mu$ M after 24 h. Meanwhile, commercial Mitotracker Green and Red were evaluated in HeLa cells to compare the cytotoxicity with rFrFrF and TAMRA-rFrFrF (Figure 2.5). Mitotracker Green appears to be more toxic at concentrations over 8  $\mu$ M, while MitoTracker Red exhibits high cytotoxicity at 4  $\mu$ M with only 30% of cells alive after 24 h incubation.

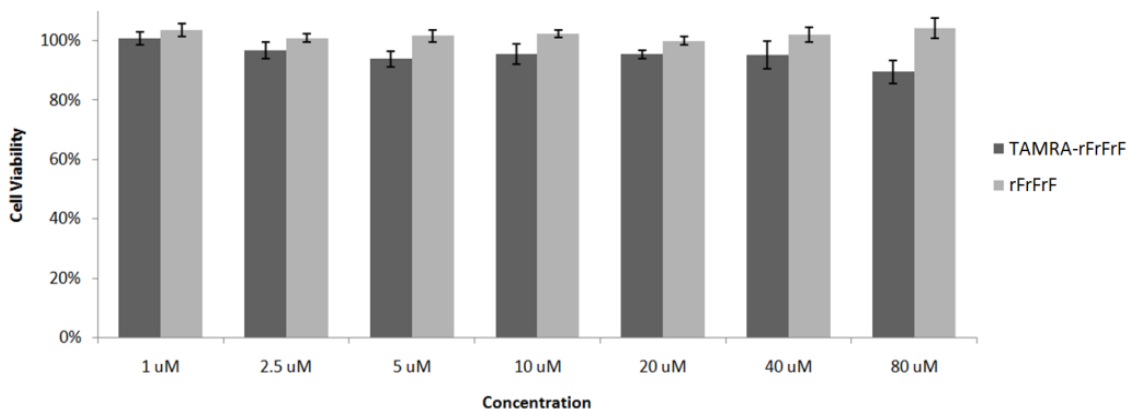


**Figure 2.3** Cell viability of HeLa cells after treatment with TAMRA-rFrFrF and unconjugated rFrFrF at different concentrations. HeLa cells with no treatment was classified as 100%.

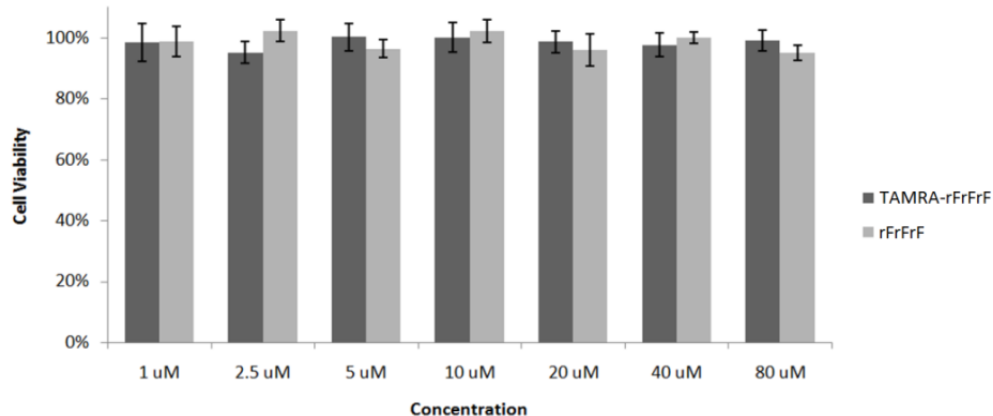


**Figure 2.4** Cell viability of LLC-PK1 cells after treatment with TAMRA-rFrFrF and unconjugated rFrFrF at different concentrations. LLC-PK1 cells with no treatment was classified as 100%.

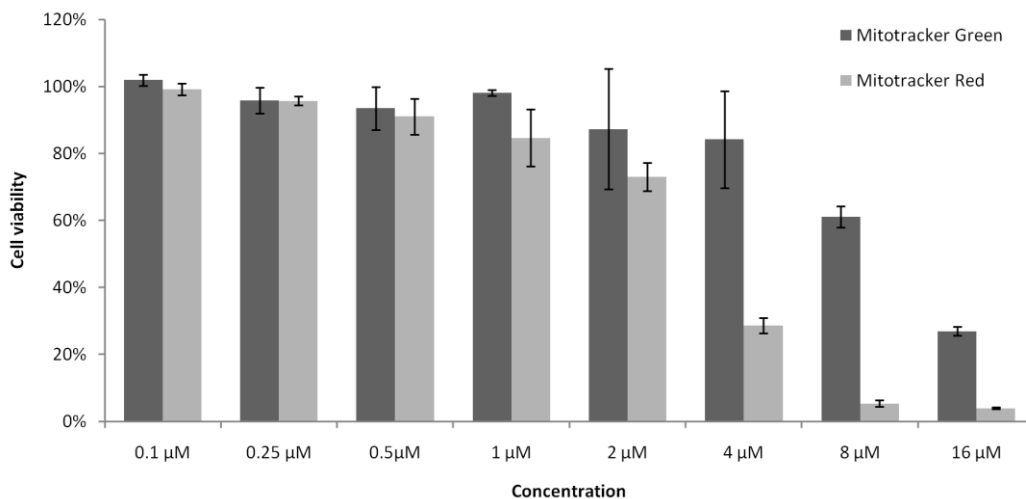


**Figure 2.5** Cell viability of HeLa cells after treatment with Mitotracker Green and Red at different concentrations. HeLa cells with no treatment were classified as 100%.

### 2.3.2 Cellular Uptake and Colocalization

The use of the new MPP probe, TAMRA-rFrFrF, was then investigated as a mitochondrial-targeting agent by fluorescence imaging and colocalization studies. Three experimental groups were conducted, including TAMRA-rFrFrF, TAMRA, and TAMRA physically mixed with unconjugated rFrFrF. After 1.5 h incubation with one of the aforementioned reagents with either HeLa or LLC-PK1 cells, the culture media was

changed to pure Dulbecco's Modified Eagle Medium (DMEM) and the HeLa cells were further incubated for 1 d.

As shown in Figure 2.6, bright fluorescence was observed for cells incubated with TAMRA-rFrFrF. By contrast, no fluorescence was detected for the other two groups (TAMRA and TAMRA mixed with unconjugated rFrFrF). Furthermore, TAMRA-rFrFrF displayed a high level of selectivity for mitochondria targeting, with a Pearson's correlation coefficient value of 0.88 relative to MitoTracker Green, a commercial mitochondrial staining agent while unconjugated TAMRA itself and the physical mixture of TAMRA with rFrFrF exhibited no mitochondria targeting ability nor capability of being uptaken by cells.<sup>69</sup>

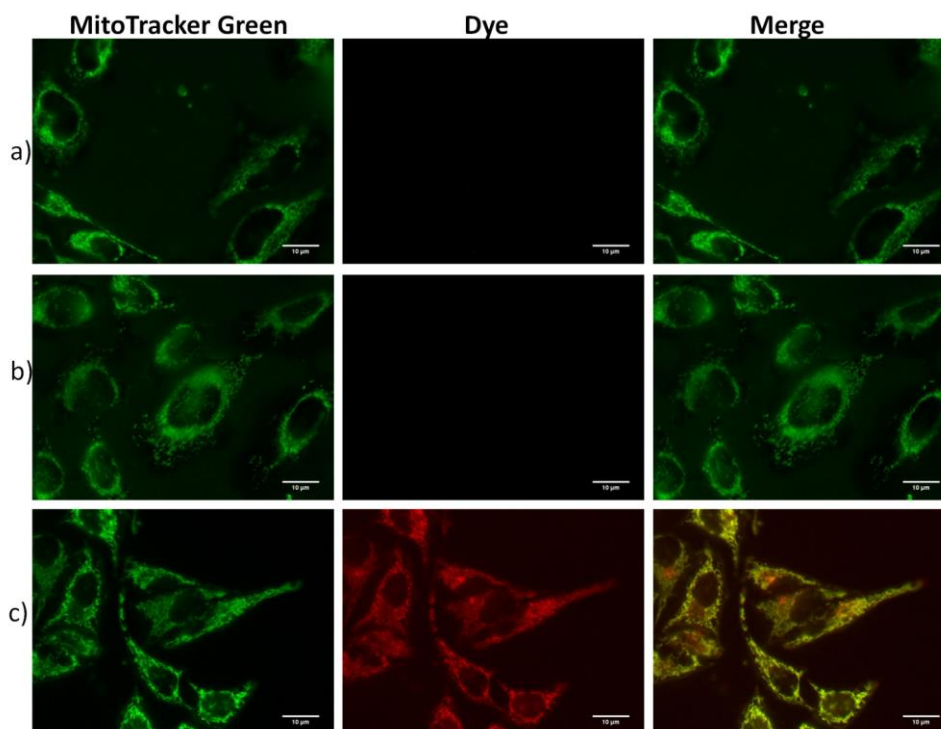


**Figure 2.6** Cellular uptake imaging. HeLa cells were incubated with 5  $\mu\text{M}$  of TAMRA, TAMRA mixed with unconjugated rFrFrF and TAMRA-rFrFrF separately for 1.5 h, and after washing, additional incubation of the cells at 37  $^{\circ}\text{C}$  for 1 d (post-incubation time). a) HeLa cells treated with TAMRA, b) HeLa cells treated with TAMRA mixed with unconjugated rFrFrF, c) HeLa cells treated with TAMRA-rFrFrF.

To further evaluate mitochondrial selectivity, TAMRA-rFrFrF colocalization studies with Lysotracker Green and endoplasmic reticulum (ER-tracker Green) were also performed with HeLa cells. Poor co-localization was observed between TAMRA-rFrFrF with Lysotracker Green or ER-tracker Green, in which Pearson's values are less than 0.4 (Figures 2.7 and 2.8). Thus, the designed rFrFrF sequence is attributed for successful cell uptake and high selectivity for mitochondrial targeting.

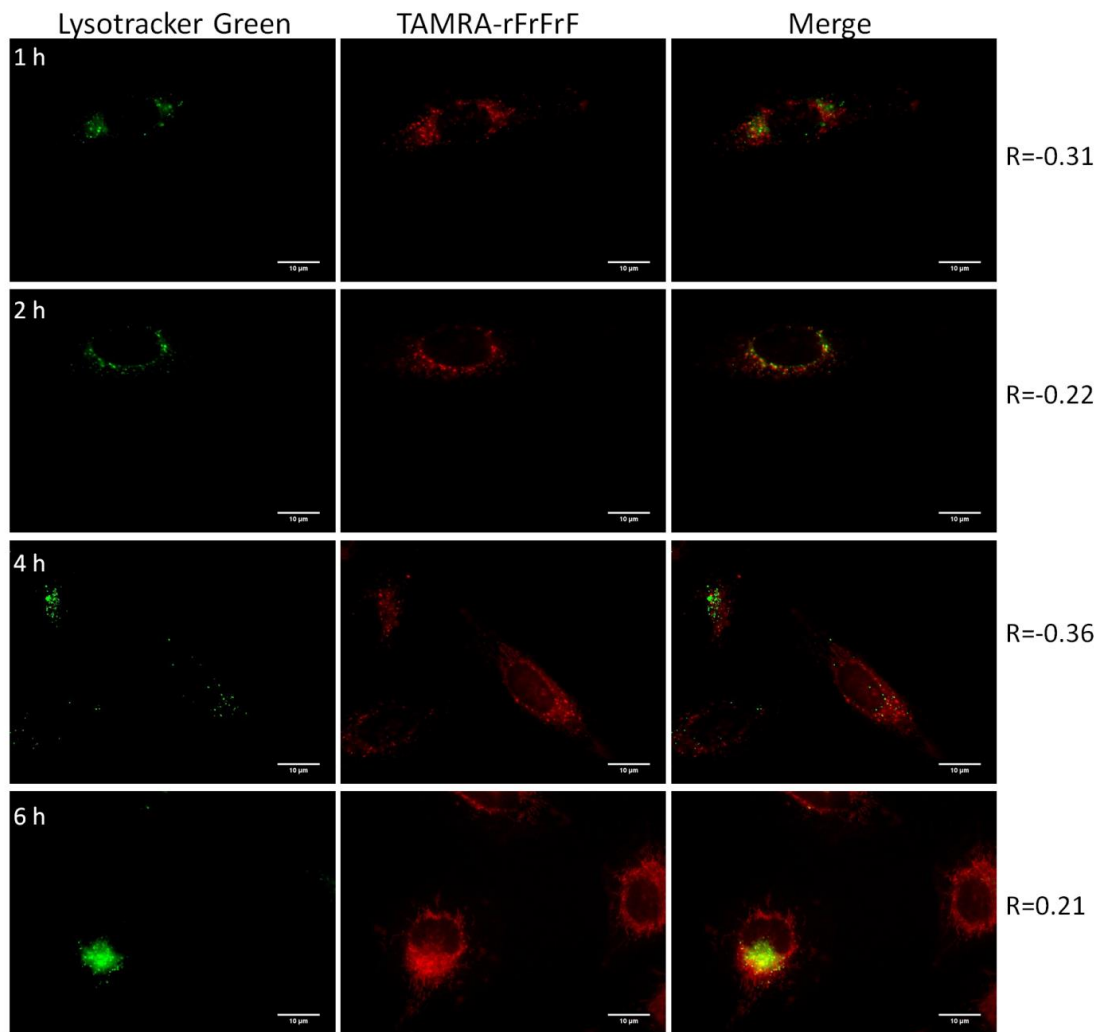


**Figure 2.7** Colocalization of LT Green. HeLa cells were incubated with 5 µM TAMRA-rFrFrF for 1.5 h, and, after washing out the TAMRA-rFrFrF, an extra incubation of the cells at 37 °C for various times (post-incubation time). Then, cells were incubated with 200 nM of Lysotracker Green for 1 h and washed out before cell imaging. Pearson's Value is labeled as R.

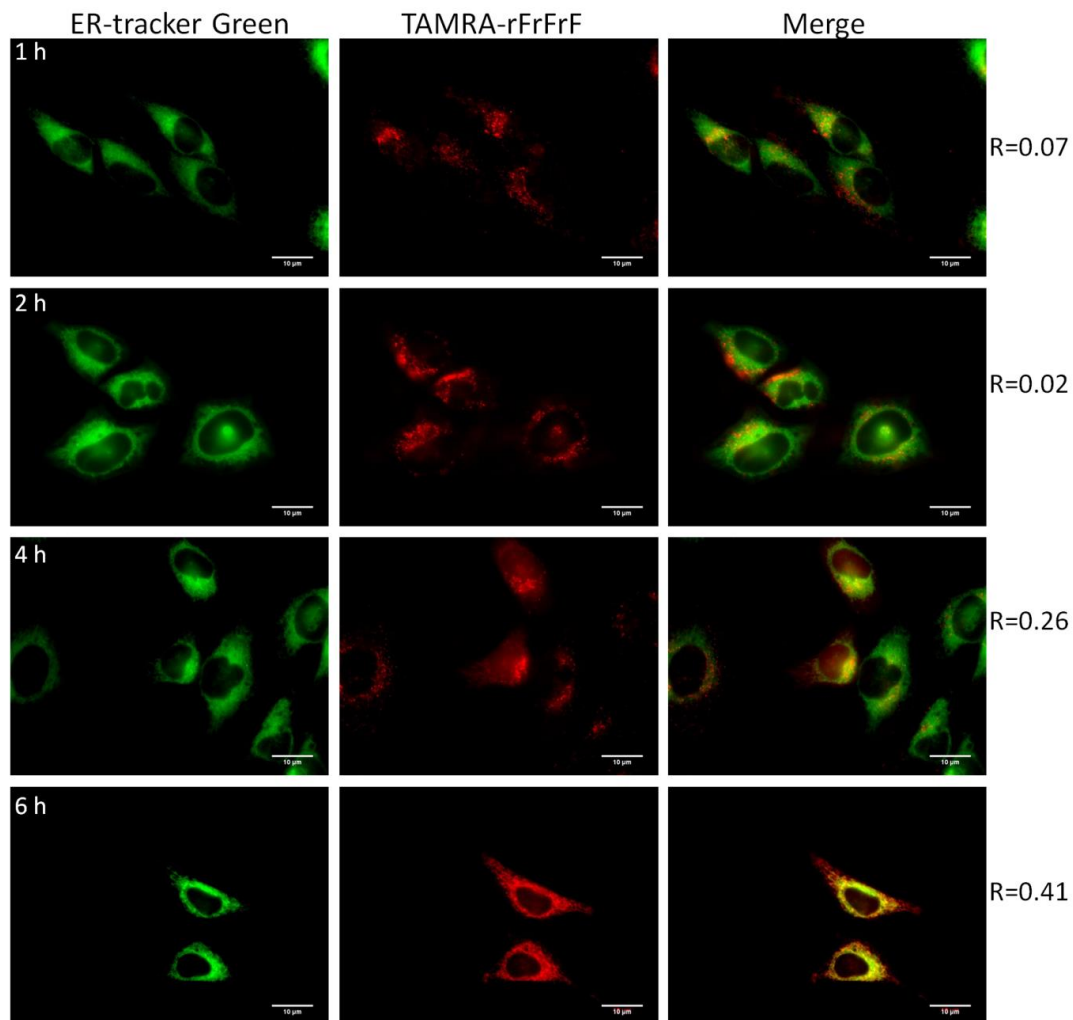


**Figure 2.8** Colocalization of ER Green. HeLa cells were incubated with 5  $\mu\text{M}$  TAMRA-rFrFrF for 1.5 h, and, after washing out the TAMRA-rFrFrF, an extra incubation of the cells at 37  $^{\circ}\text{C}$  for various times (post-incubation time). Then, cells were incubated with 1  $\mu\text{M}$  of ER-tracker Green for 30 min and washed out before cell imaging. Pearson's Value is labeled as R.

### 2.3.3 Time Dependent Colocalization

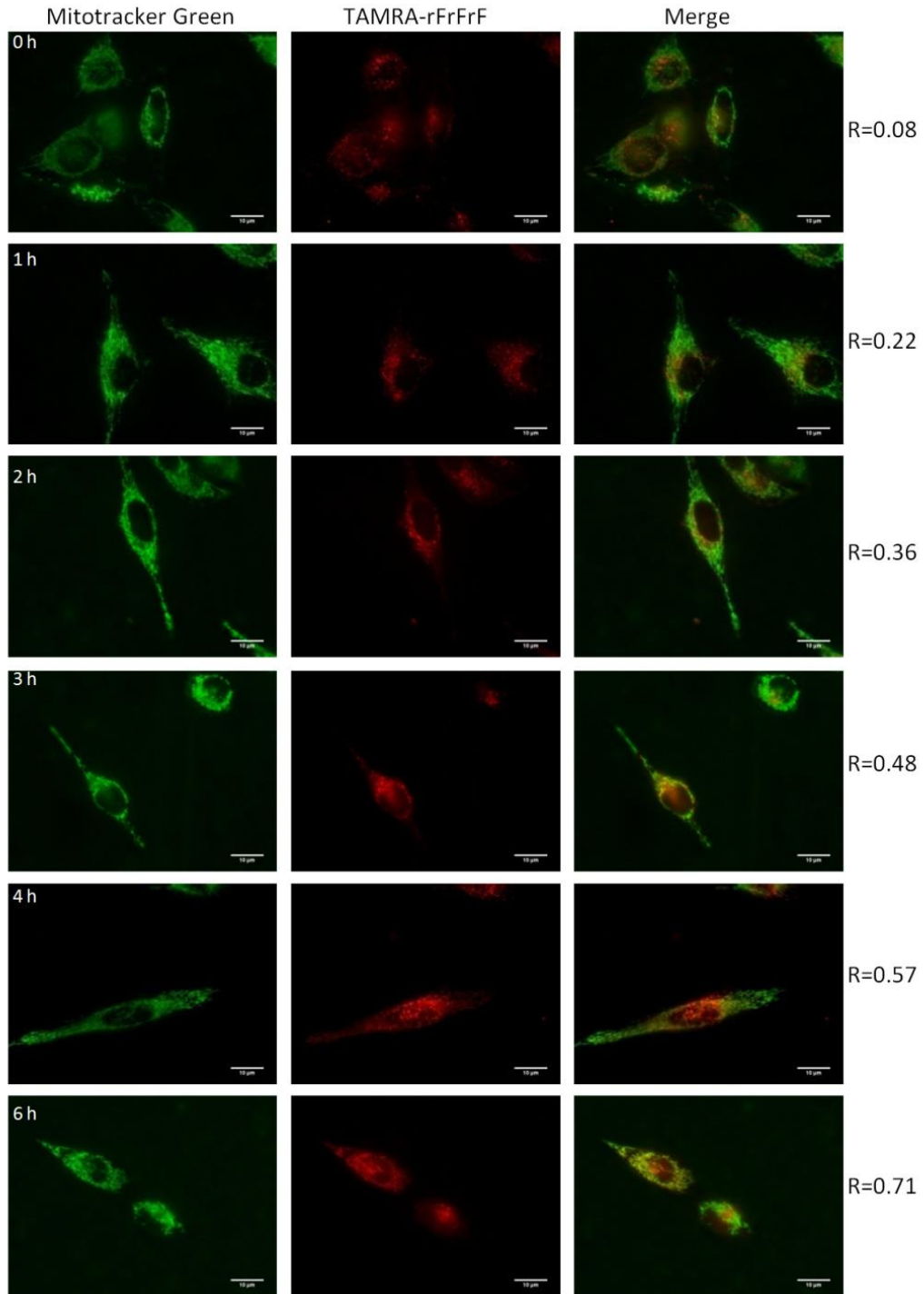
To better understand the time dependent mitochondrial uptake of TAMRA-rFrFrF, time-dependent cell imaging experiments were conducted. In general, after incubation with TAMRA-rFrFrF for 1.5 h, after washing, HeLa or LLC-PK1 cells were then incubated in cell medium alone for various times (post-incubation time) before cell imaging for long

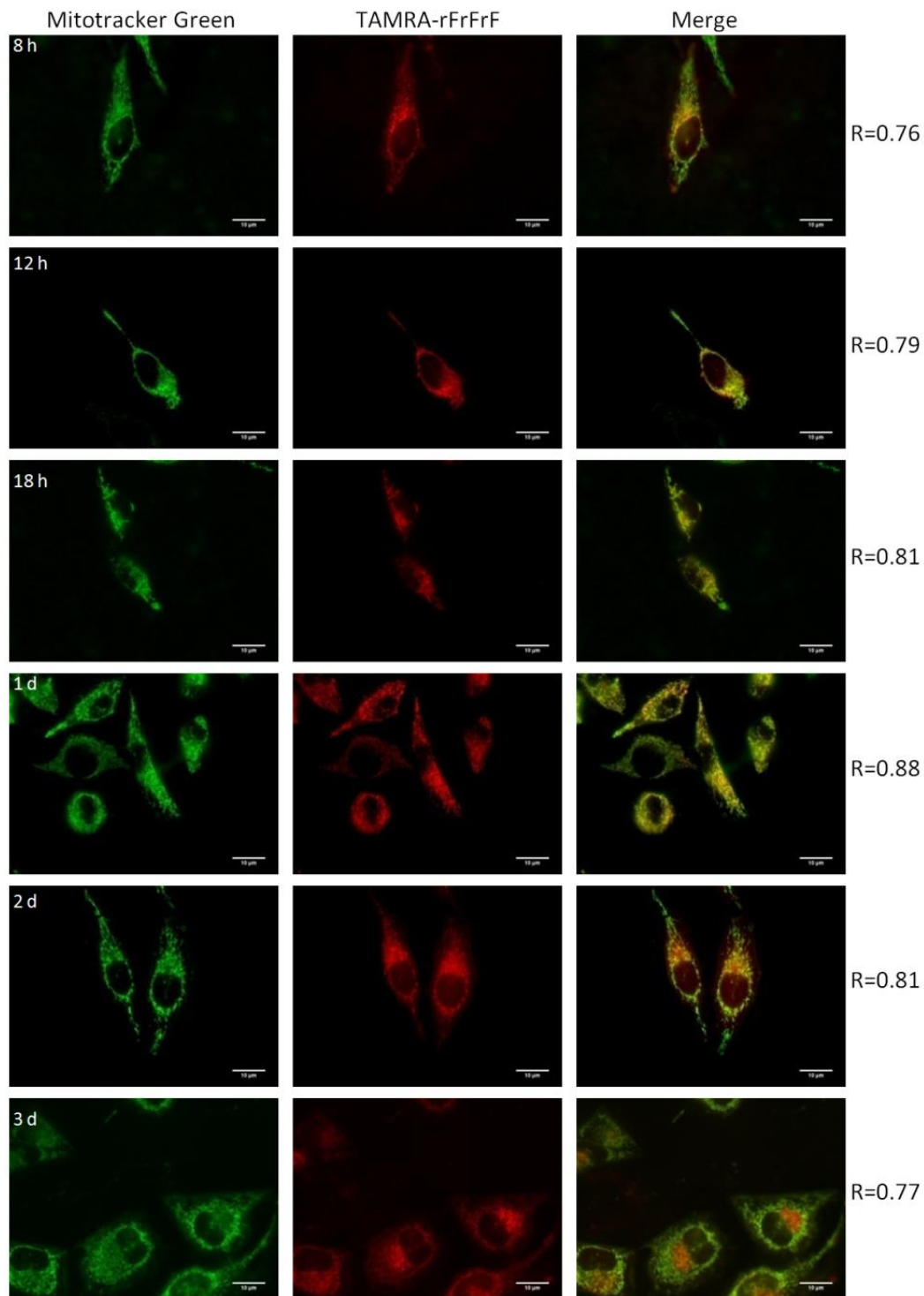
term mitochondria tracking was performed. Cells that underwent 0 to 4 h post-incubation (Figures 2.9 and 2.10) displayed strong fluorescence, however, mitochondria targeting was less efficient at these time points, which may be related to the charge and hydrophobicity of TAMRA-rFrFrF. The mitochondrial membrane exhibits hydrophobicity and a potential difference in which the inner mitochondrial membrane is negatively charged and outer membrane is positively charged.<sup>53, 54, 70</sup> MPPs that possess positive charges and hydrophobicity tend to target and penetrate the mitochondria membrane more easily.<sup>56</sup> However, increasing peptide charge or hydrophobicity may increase mitochondrial disruptive activity and lead to unwanted side effects and toxicity.<sup>63, 64</sup>

We discovered that our MPP could slowly but effectively target mitochondria. As shown in Figures 2.9, 2.10, 2.11 and 2.12, TAMRA-rFrFrF largely permeated mitochondria after 6 h of post-incubation time. Moreover, cells still exhibited significant fluorescence in mitochondria even at 3 d of post-incubation. By comparison Mitotracker Green was not capable of tracking mitochondria reliably much longer than 6 h (Figure 2.11). These results clearly demonstrating long-term mitochondria tracking ability of the new MPP probe.

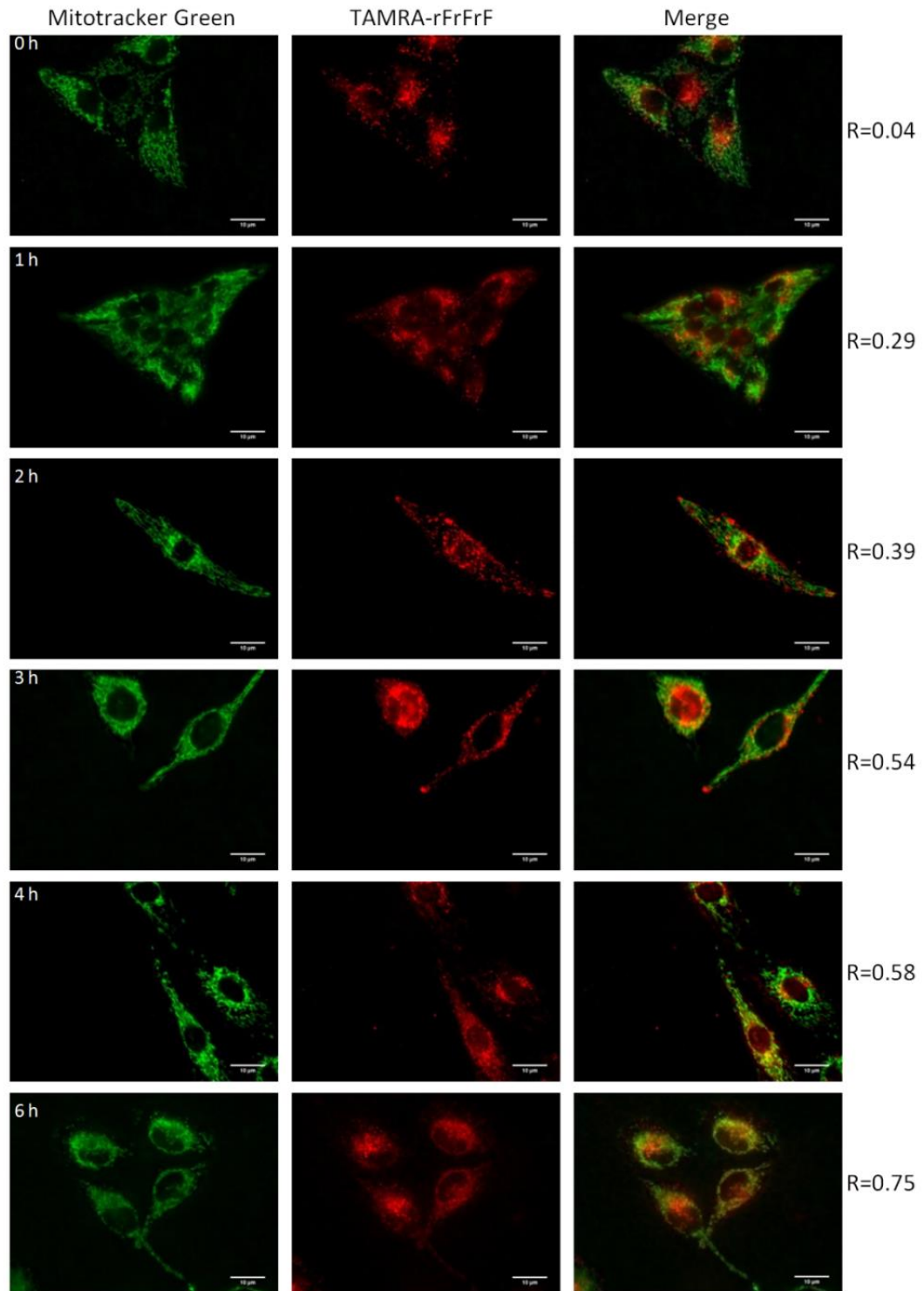
Mitochondria are highly dynamic organelles that constantly undergo fission, fusion and degradation,<sup>71</sup> e.g., HeLa cells undergo 1.44 events/min of fission.<sup>72</sup> These constant changes cause asymmetrical distribution of matrix proteins in the daughter mitochondria.<sup>73, 74</sup> In our study, TAMRA-rFrFrF exhibited persistent localized mitochondria staining ability without significant depletion or leakage over the 3 d post-incubation period, an assertion that was quantitatively confirmed by the Pearson's

correlation coefficient values (Figure 2.12b), indicating TAMRA-rFrFrF is capable of mitochondria targeting under frequent fission and fusion events.





**Figure 2.9** Time dependent HeLa cell colocalization. HeLa cells were incubated with 5  $\mu$ M TAMRA-rFrFrF for 1.5 h, and, after washing out the TAMRA-rFrFrF, an extra incubation of the cells at 37  $^{\circ}$ C for various times (post-incubation time). Then, cells were incubated with 100 nM of Mitotracker Green for 15 min and washed out before cell imaging. Pearson's Value is labeled as R.



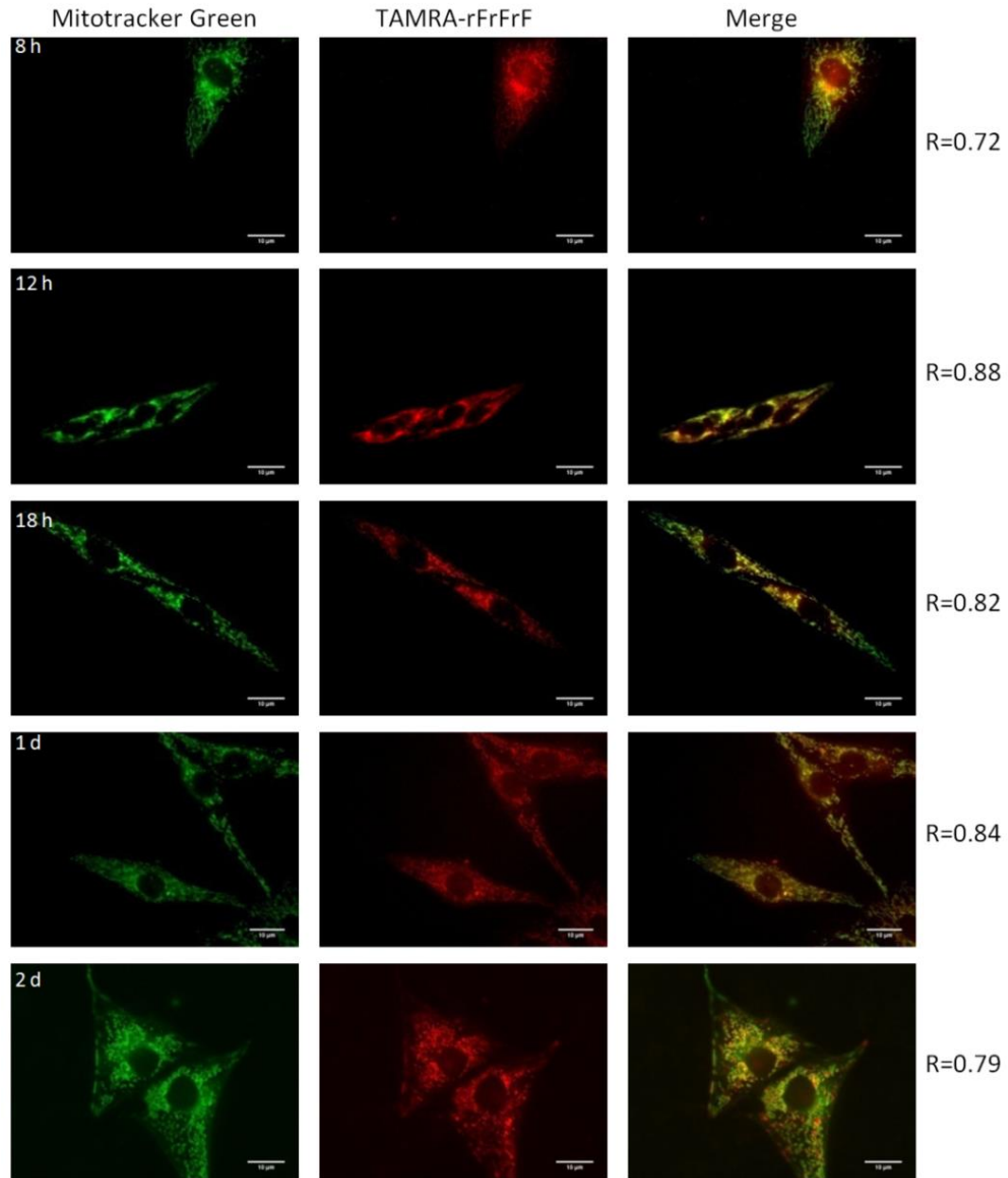


**Figure 2.10** Time dependent LLC-PK1 cell colocalization. LLC-PK1 cells were incubated with 5  $\mu$ M TAMRA-rFrFrF for 1.5 h, and, after washing out the TAMRA-rFrFrF, an extra incubation of the cells at 37  $^{\circ}$ C for various times (post-incubation time). Then, cells were incubated with 100 nM of Mitotracker Green for 15 min and washed out before cell imaging. Pearson's Value is labeled as R.

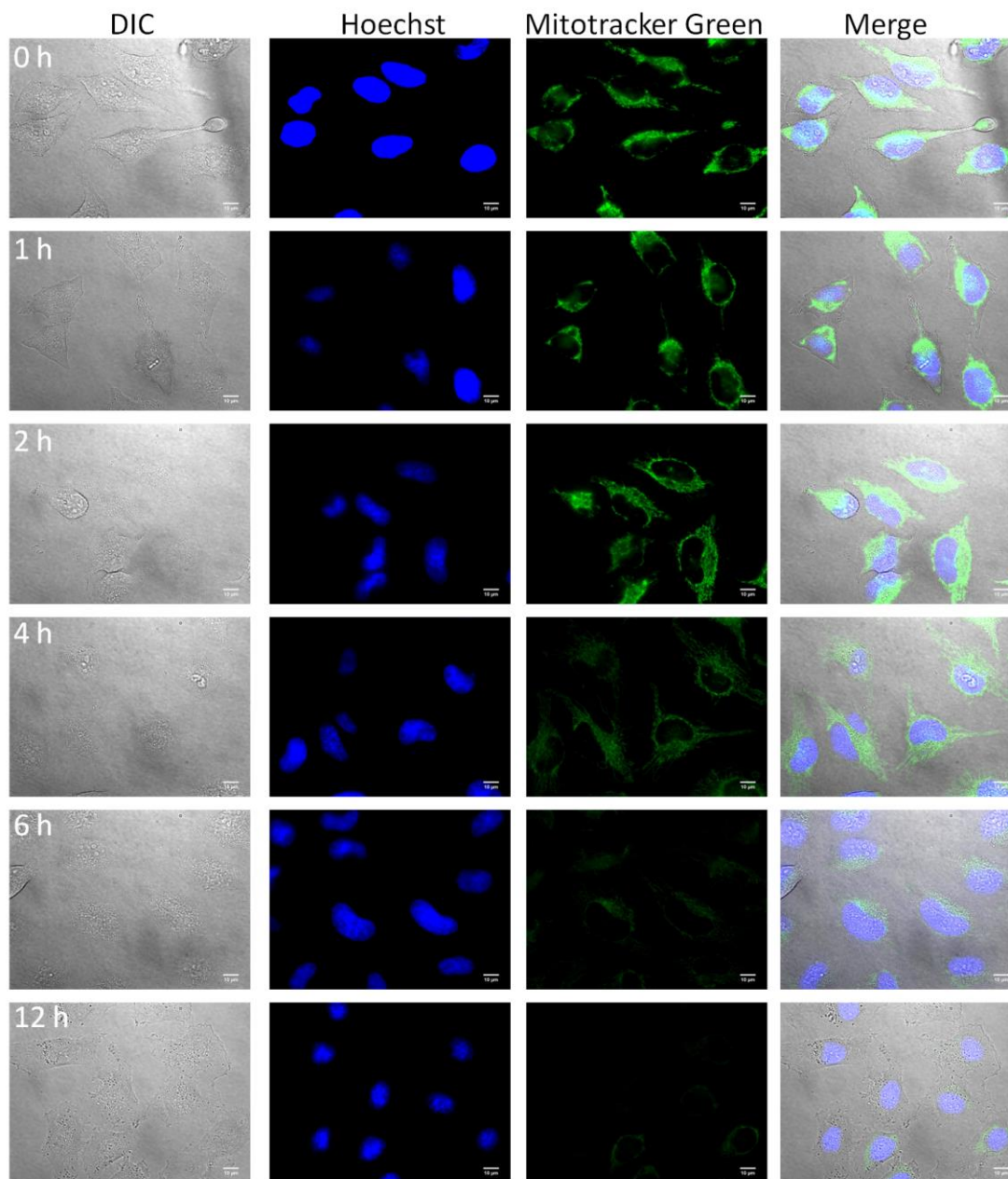


**Figure 2.11** Time dependent MT-Green cell imaging. HeLa cells were incubated with 100 nM Mitotracker Green for 15 min, and, after washing out Mitotracker Green, an extra incubation of the cells at 37 °C for various times (post-incubation time). Then, cells were incubated with 100 nM of Hoechst 33258 for 10 min and washed out before cell imaging. Pearson's Value is labeled as R.

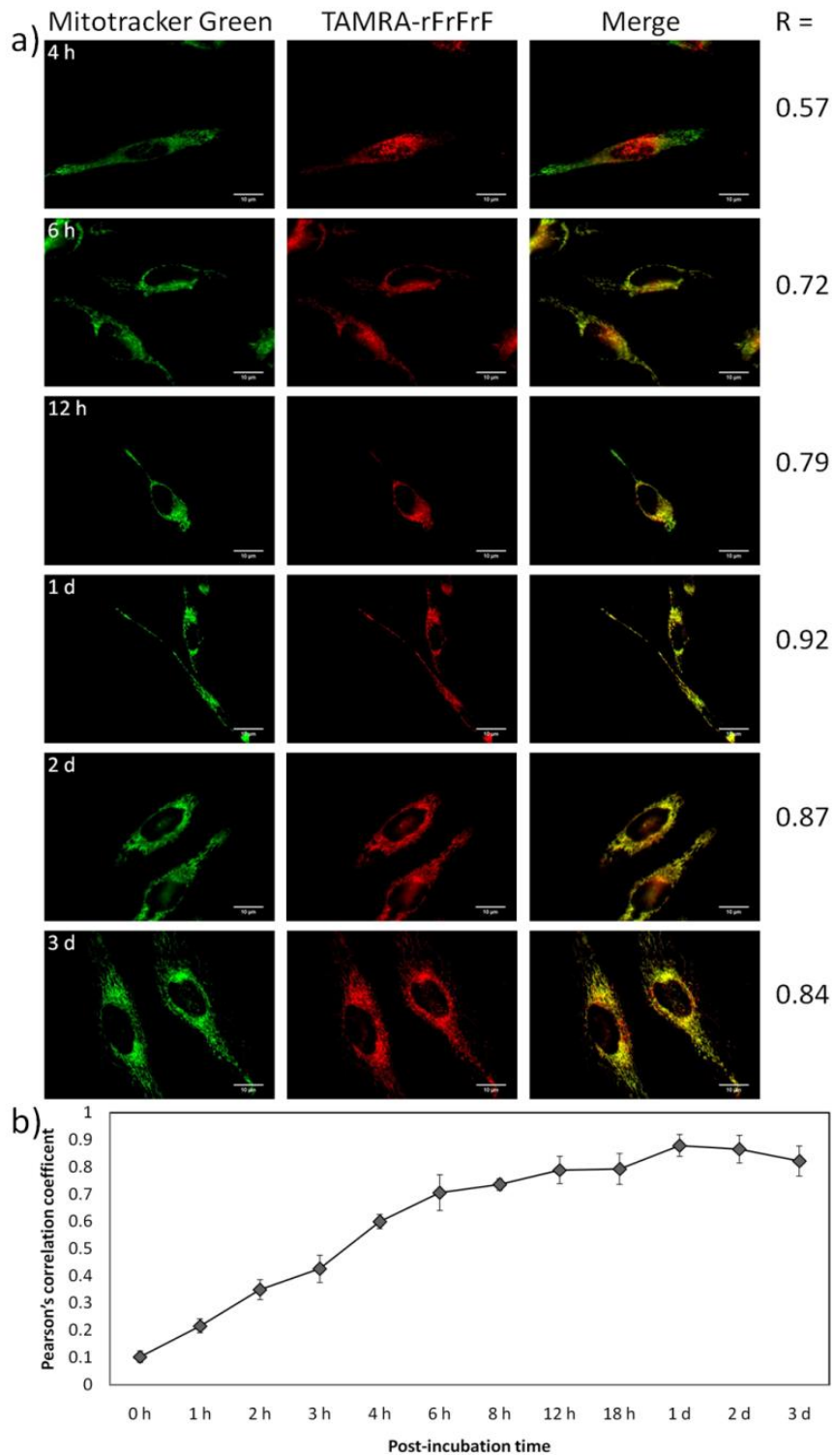


**Figure 2.12** Time dependent cell imaging. a) HeLa cells were incubated with 5  $\mu$ M of TAMRA-rFrFrF for 1.5 h, and after washed out the TAMRA-rFrFrF an extra incubation of the cells at 37  $^{\circ}$ C for various times (post-incubation time). Then, cells were incubated with Mitotracker Green for 15 min and washed before cell imaging. Pearson's value is labeled as R. b) Post-incubation time dependent Pearson's correlation coefficient of HeLa cells.

### 2.3.4 Isolated Mitochondria Uptake

To further confirm the mitochondria targeting ability of TAMRA-rFrFrF, mitochondria were isolated from TAMRA-rFrFrF treated cells and fluorescence intensities were recorded with a fluorescence spectrometer.<sup>75</sup> The fluorescence intensities of isolated mitochondria with 6 h, 12 h, 1 d, 2 d, and 3 d post-incubation were unquestionably much more intense than those of the blank - isolated untreated mitochondria (Figure 13 and Figure 14 ). These results clearly demonstrate that the uptake of TAMRA-rFrFrF is time-dependent and appears rather efficient. There was no intensity decrease of TAMRA-rFrFrF in mitochondria upon prolonged incubation. In fact, the post-incubation time was a key factor for TAMRA-rFrFrF to accumulate in the mitochondria in HeLa cells.

Further, the mitochondria present a whole set of complex proteolytic enzyme systems that regulate mitochondrial function and activities. Especially for mitochondrial degradation,<sup>76, 77</sup> endogenous proteases are responsible for the degradation of their internal proteins, which are eventually shuttled back to the cytoplasm by a specific peptide transporter.<sup>78, 79</sup> The fluorescence intensity of TAMRA-rFrFrF did not decrease from 12 h to 3 d, which indicated TAMRA-rFrFrF underwent no apparent release to the cytoplasm and was proteolytically stable. Overall TAMRA-rFrFrF is capable of long-term mitochondrial tracking up to 3 d, with high stability and selectivity.

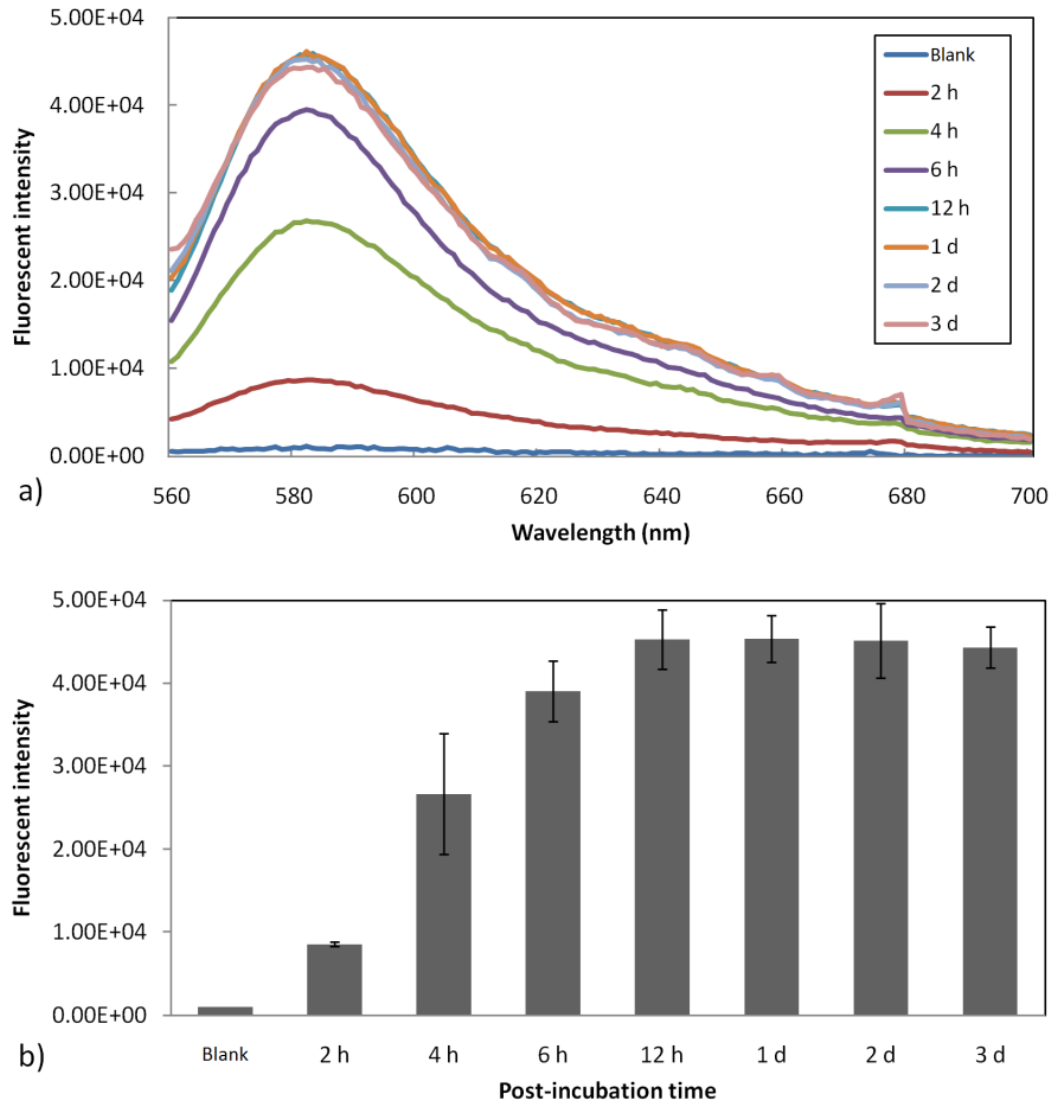


**Figure 2.13** HeLa cells mitochondria uptake TAMRA-rFrFrF measurement. 5  $\mu$ M of TAMRA-rFrFrF was pre-incubated with HeLa cells for 1.5 h, followed by washing out TAMRA-rFrFrF and post-incubation of the HeLa cells for 2 h, 4 h, 6 h, 12 h, 1 d, 2 d, and 3 d. Isolated mitochondria from untreated cells were the blank (N = 3).

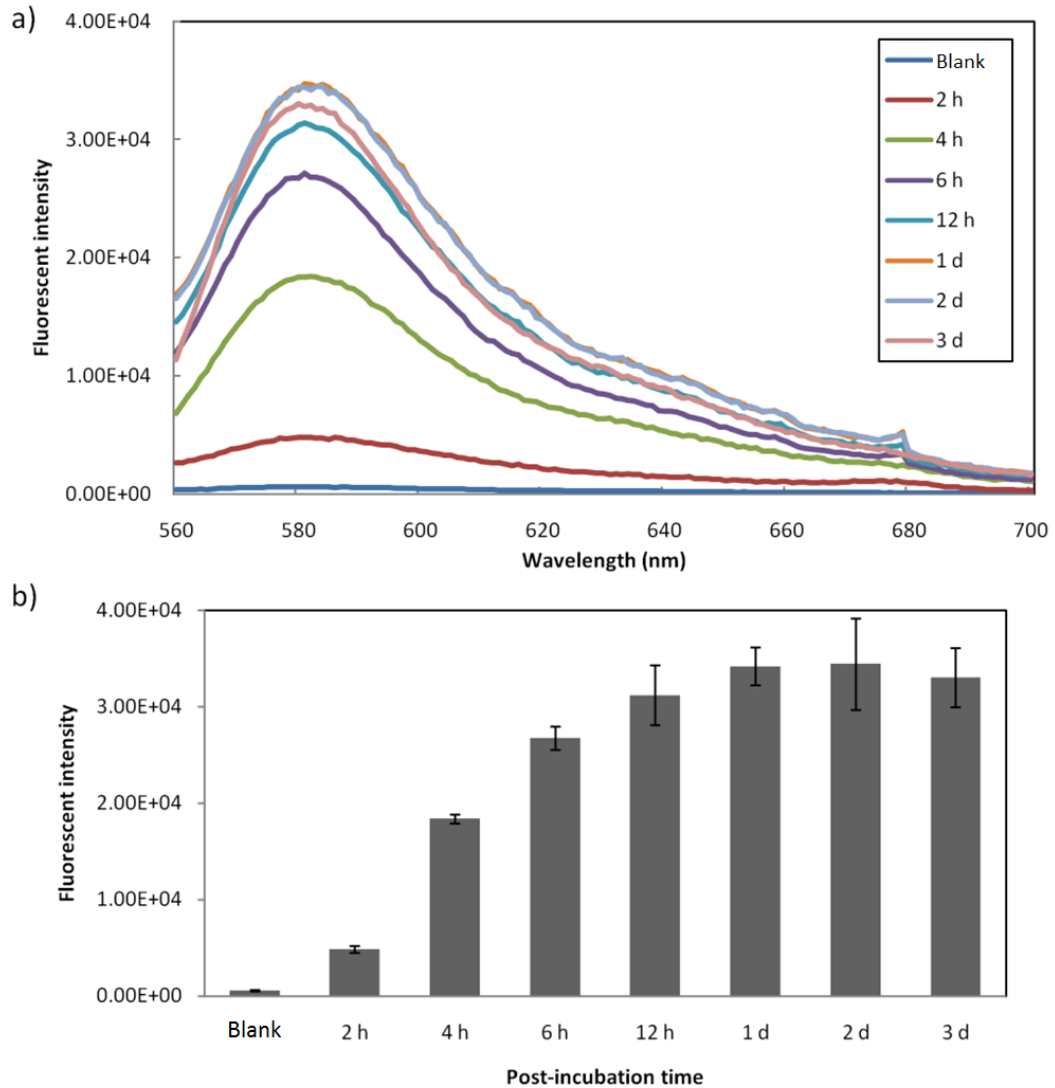


**Figure 2.14** LLC cells mitochondria uptake TAMRA-rFrFrF measurement. 5  $\mu$ M of TAMRA-rFrFrF was pre-incubated with LLC cells for 1.5 h, followed by washing out TAMRA-rFrFrF and post-incubation of the LLC cells for 2 h, 4 h, 6 h, 12 h, 1 d, 2 d, and 3 d. Isolated mitochondria from untreated mitochondria cells were the blank. (N=3).

### 2.3.5 Oxygen Consumption Rate (OCR)

To probe mitochondria function of cells incubated with TAMRA-rFrFrF, oxygen consumption rates were measured in HeLa cells using a Seahorse analyzer.<sup>80</sup> The results demonstrated that the basal respiratory rate and maximal respiratory capacity (Figure 2.15) decreased somewhat in the TAMRA-rFrFrF treated vs. untreated HeLa cells. Although decreases in maximum respiratory capacity and basal respiratory rate are strong indicators of potential mitochondrial dysfunction,<sup>81</sup> in this situation, the decreases are most likely a result of a change in the potential difference of outer and inner mitochondrial membranes caused by the cationic rFrFrF rather than mitochondrial dysfunction.<sup>81, 82</sup> The drop of mitochondrial membrane potential difference will inhibit the activity of electron transport chain, which would decrease maximum respiratory capacity and basal respiratory rate.<sup>83, 84</sup> Furthermore, spare respiratory capacity exhibited only a slight decrease while ATP production underwent no significant reduction when compared with a control, indicating the TAMRA-rFrFrF probe has minimal influence on mitochondrial respiration.<sup>85</sup> In fact, the results indicated that mitochondrial functions were mostly unchanged.

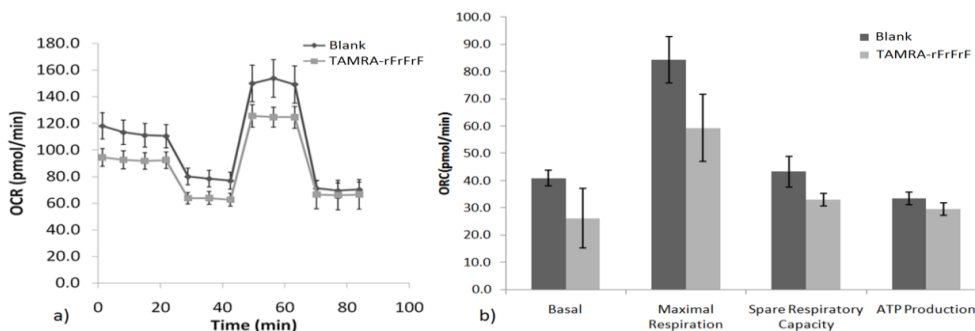


**Figure 2.15** Oxygen consumption rates. a) Oxygen consumption rates (OCR) in TAMRA-rFrFrF treated vs. untreated HeLa cells (blank, n = 5). OCR was measured approximately every 8 min using an XF-96 analyzer as described in the Supporting Information Methods section. b) The rates of basal respiration, maximal respiratory capacity, spare respiratory capacity, and ATP-linked respiration (ATP production).

## 2.4 Conclusion

In conclusion, a novel MPP probe, TAMRA-rFrFrF, was designed that contained 6 amino acid residues. Our investigations demonstrated the new MPP probe's utility in long-term *in vivo* mitochondrial tracking for up to 3 d, which is far superior to commercial Mitotracker Green and Red. Importantly, the TAMRA-rFrFrF probe can undergo mitochondria distribution, activities, and fission or fusion events with no degradation or transportation by mitochondria proteolysis, which fulfills major criteria for long-term mitochondria tracking. In addition, we have shown that the TAMRA-rFrFrF was essentially benign and biocompatible from cell viability and oxygen consumption rate experiments. There is an important link between mitochondrial morphology change and mitochondrial dysfunction,<sup>47, 86-88</sup> in which mitochondrial morphology serves as a marker to study and treat mitochondria dysfunction related disease. Therefore, this TAMRA-rFrFrF MPP probe is a potential candidate for live cell mitochondrial morphological and mitochondrial dysfunction studies.

## CHAPTER 3

### MITOCHONDRIAL PH REGULATING AND THE ROLE IN REDUCING DRUG RESISTANCE

Mitochondrial membrane polarization (mitochondrial membrane potential difference) is formed by the membrane proton gradient, which plays a key role in chemoresistance due to the hyperpolarization of mitochondrial membrane in cancer cells. Herein, we hypothesize that regulating mitochondrial pH to depolarize the mitochondrial membrane in cancer cells may offer a potential therapeutic strategy to counter certain chemotherapeutic drug resistance.

A BODIPY chromophore based triarylsulfonium photoacid generator (BD-PAG) was designed and synthesized to target mitochondria with the aim to regulate mitochondrial pH. Cell viability assays demonstrate the relatively low toxic and biocompatibility of BD-PAG. To determine the BD-PAG capabilities, examination of cellular distribution was evaluated in HeLa and MCF-7 cell lines, demonstrating the selective localization of BD-PAG in mitochondria as evidenced by high Pearson's colocalization coefficients when co-incubated with commercial mitotracker probes. Investigation of mitochondrial pH and assay of membrane potential indicated BD-PAG is capable of regulating mitochondrial pH, which reduces the membrane potential. Time lapse, Z-stack images and caspase assays further demonstrated the membrane potential change via pH regulation. Further experiments demonstrated their use in against anti-cancer drug resistance, all described below.

### 3.1 Introduction

Mitochondria are essential organelles as they are the site of respiration and are composed of a double-membrane in eukaryotic cells, and involved in many essential cellular functions, including energy supply, cell cycle and growth, cell signaling pathways, apoptosis, and metabolism.<sup>89</sup> The mitochondrial outer membrane (OMM) and inner membrane (IMM) are composed of phospholipid bilayers, which harbor electron transport chain complexes (ETC).<sup>90</sup> ETC use electron flow to pump protons ( $H^+$ ) into the intermembrane space to generate a proton gradient that drives the synthesis of adenosine triphosphate (ATP), and, furthermore, create a potential force (mitochondrial membrane polarization) represented by the mitochondrial membrane potential ( $\Delta\Psi \sim -150$  to  $-180$  mV).<sup>91-94</sup> More important, the disturbed  $\Delta\Psi$  in dysfunctional mitochondria may be related to multiple diseases, especially cancer.<sup>95-97</sup>

It was found that mitochondrial membrane hyperpolarization contributes to greater migration and invasion of cancer cells while the  $\Delta\Psi$  is as low as  $-220$  mV, due to the ETC functional status.<sup>98</sup> Moreover, the change of membrane polarization has direct impact on mitochondrial outer membrane permeabilization (MOMP).<sup>99, 100</sup> MOMP constitutes a decisive step in apoptosis (a form of programmed cell death), regulating cytochrome C release and activating caspase cascade.<sup>101</sup> Most cancer treatments, including chemotherapy, radiation therapy and immunotherapy, aim to trigger apoptosis.<sup>102, 103</sup> However, MOMP is significantly reduced in cancer cells due to the low  $\Delta\Psi$ , and this a major source of drug resistance in cancer treatment.<sup>104, 105</sup> Hence, regulating  $\Delta\Psi$  in cancer cells may offer a potential therapeutic strategy to overcome drug resistance.

Drug resistance remains a persistent problem in treating cancer with inhibition of apoptosis pathway becoming more prevalent.<sup>106, 107</sup> However, most of studies focus on the upper stream of the apoptosis pathway, such as the Bcl-2 protein family expressing regulation.<sup>108-110</sup> So far, there has been no literature reports of regulating the mitochondrial pH to overcome drug resistance, by virtue of the lack of strategies to target mitochondrial and introduce acid effectively.

Triarylsulfonium based photoacid generators (PAGs) are light-sensitive organic compounds that can produce proton ( $H^+$ ) upon exposure to certain wavelengths of light.<sup>111</sup> Lipophilic cationic properties of triarylsulfonium salts are similar to triphenyl phosphonium (TPP) salts, a frequently used mitochondria targeting moiety, and make it a promising candidate to target mitochondria.<sup>112, 113</sup> Herein, we designed a visible light absorbing BODIPY chromophore-based triarylsulfonium (BD-PAG) (Figure 3.1) to target mitochondria. IN the electronically excited state, energy transfers to triarylsulfonium moiety to facilitate homolytic cleavage of a C-S bond, forming a cation-radical on the sulfur-containing fragment, and, after hydrogen atom abstraction, form  $H^+$  to regulate mitochondrial pH.<sup>114</sup> This is the first report of a PAG to regulate mitochondrial pH to depolarize the mitochondrial membrane and attenuate cancer drug resistance.

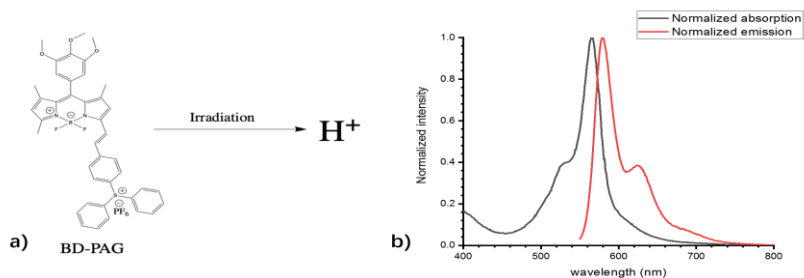


**Figure 3.1** Molecular structure and spectra. a) Molecular structure of BD-PAG, b) normalized absorption and emission spectra of BD-PAG.

## 3.2 Results and Discussion

### 3.2.1 Cell Viability

The cytotoxicity and bio-compatibility of BD-PAG in dark were evaluated in HeLa and MCF-7 cells via an MTS assay.<sup>115</sup> BD-PAG did not present any acute toxic effects over a range of concentrations, even at the highest concentration employed (80  $\mu\text{M}$ ), cell viability remained over 90% in the dark (Figure 3.2). Irradiation time-dependent cell viability was performed after incubation with BD-PAG for 4 h (to ensure cellular uptake), then BD-PAG was removed (washed away), and normal cell medium was introduced followed by LED light (Thorslab, 80  $\text{mW}/\text{cm}^2$ ) illumination of various times in both cell lines (Figure 3.3 and Figure 3.4). Only a slight toxicity of BD-PAG was observed after 20 min light irradiation in at a concentration of 20  $\mu\text{M}$ , where the cell viability was around 80%. Control group without BD-PAG but LED light showed no toxicity to the cell.

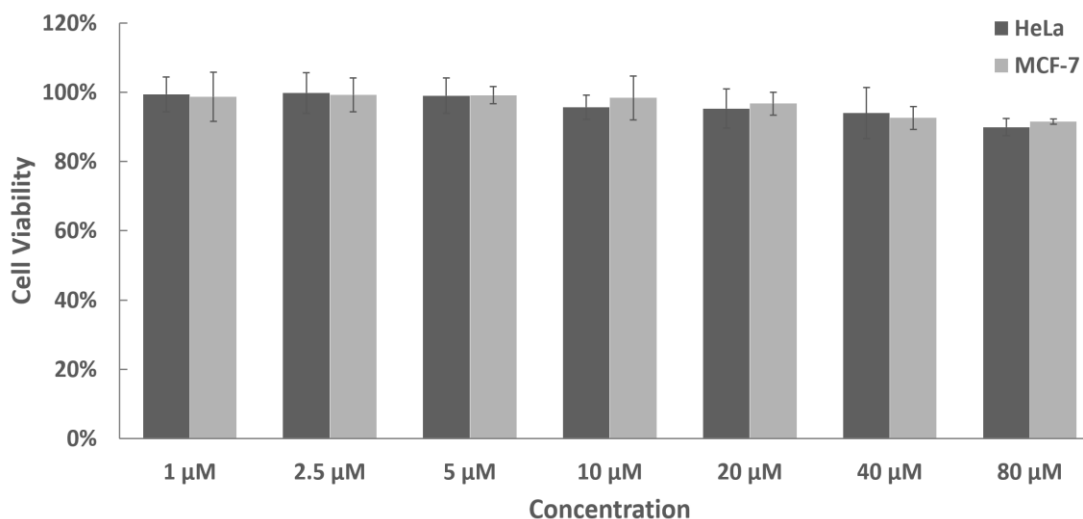


**Figure 3.2** Dark cell viability. Cell viability of HeLa and MCF-7 cells treated with 1  $\mu\text{M}$  to 80  $\mu\text{M}$  of BD-PAG at 37  $^{\circ}\text{C}$  for 24 h separately. Untreated cells were classified as 100% cell viability. (N=6)

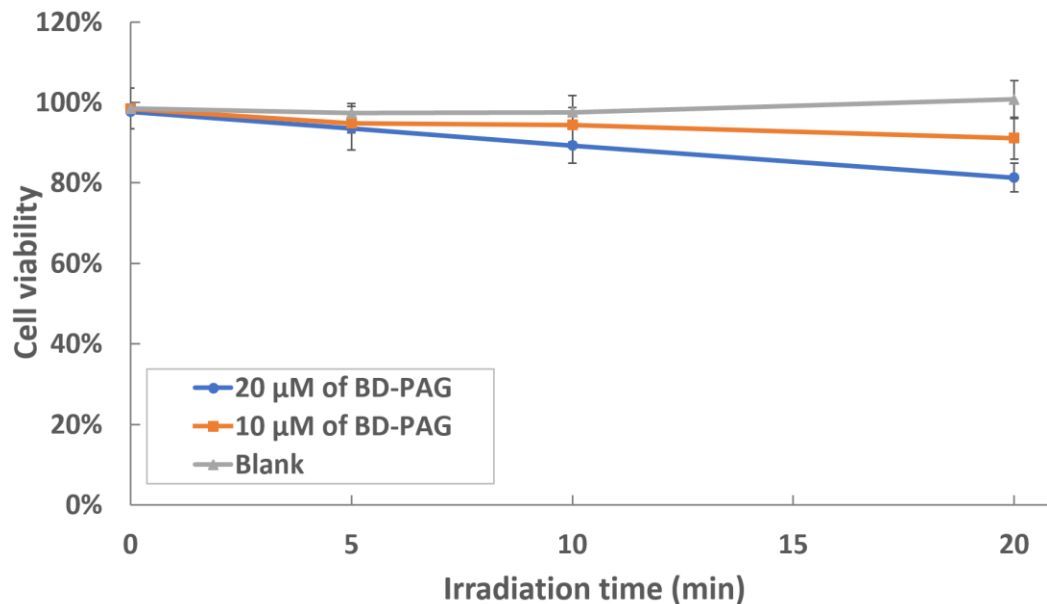


**Figure 3.3** Irradiation time dependent cell viability of HeLa cells after treatment with 10 and 20  $\mu$ M of BD-PAG for 4 h. Blank is HeLa cells with no treatment. HeLa cells with no irradiation and treatment classified as 100%. (N=6)

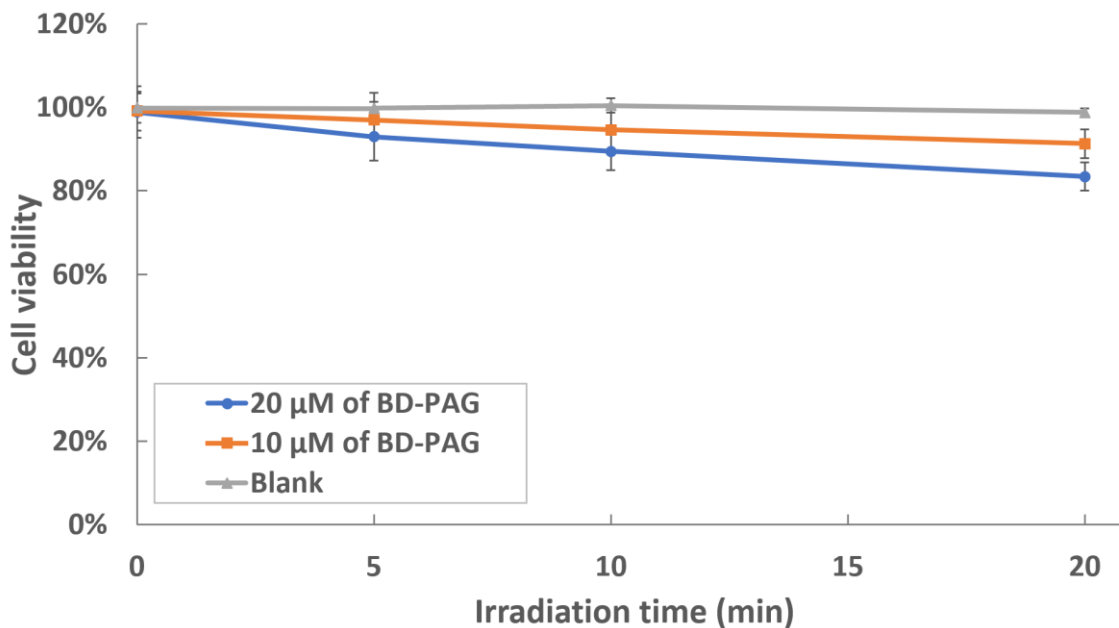


**Figure 3.4** Irradiation time dependent cell viability of MCF-7 cells after treatment with 10 and 20  $\mu$ M of BD-PAG for 4 h. Blank is MCF-7 cells with no treatment. MCF-7 cells with no irradiation and treatment classified as 100%. (N=6)

### 3.2.2 Cellular Uptake and Colocalization

For demonstration purposes, fluorescence imaging was performed in the human cervical cancer cell line, HeLa, with BD-PAG. From the basic cell viability test results, 2  $\mu\text{M}$  of BD-PAG was employed for cell incubation and fluorescence imaging. Cells treated with BD-PAG for 30 min displayed strong fluorescence upon excitation, manifesting the good biological compatibility of BD-PAG and the capability of cell uptake by (Figure 3.5).

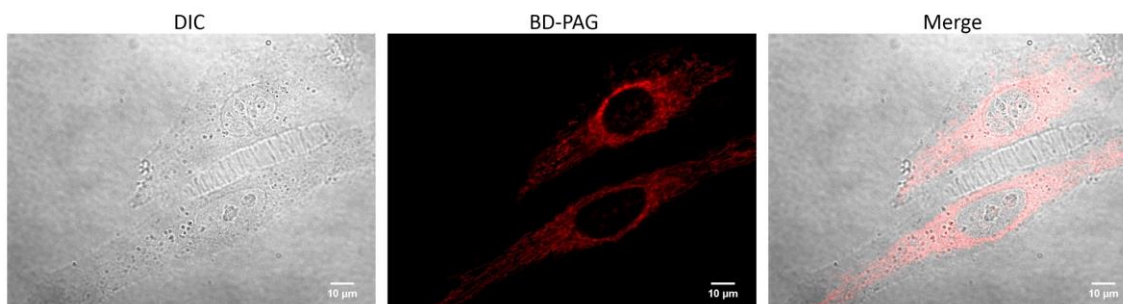


**Figure 3.5** Cellular uptake image. HeLa cells were incubated with 2  $\mu\text{M}$  of BD-PAG at 37  $^{\circ}\text{C}$  for 1 h, cell imaging was performed after washed with PBS. Texas Red filter cube (Ex: 562/40; DM: 593; Em: 624/40) for BD-PAG

To confirm the assumption that the triarylsulfonium salt should have mitochondria targeting ability due to the similar lipophilic cationic property as TPP, the localization of BD-PAG in cells was monitored by confocal microscopy. In the experiment, colocalization studies were performed with MitoTracker Green, LysoTracker Green, and ER-Tracker Green and fluorescent images were captured (Figures 3.6 and 3.7). Fluorescence from BD-PAG was observed, and the distribution colocalized very well with MitoTracker Green in both HeLa and MCF-7 cell lines. In addition, Pearson's correlation coefficient values suggest that BD-PAG exhibits a strong selectivity for mitochondria in various concentration of BD-PAG (Pearson's value  $\sim 0.9$ ), while no selective localization to lysosomes or endoplasmic reticulum (ER) was observed, as evidenced by Pearson's values less than 0.3.

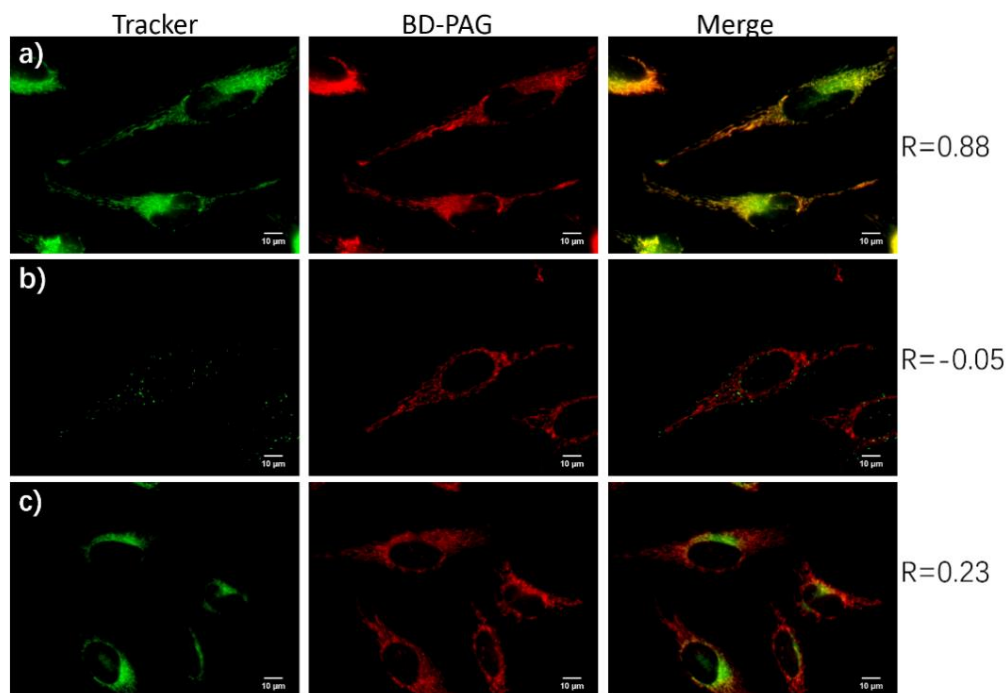


**Figure 3.6** Colocalization of BD-PAG in HeLa cells. HeLa cells were incubated with 2  $\mu\text{M}$  of BD-PAG at 37  $^{\circ}\text{C}$  for 30 min followed by colocalization stains, a) 100 nM of MitoTracker Green was incubated with cells for 15 min. b) 400 nM of LysoTracker Green was incubated with cells for 1 h. c) 1  $\mu\text{M}$  of ER-Tracker Green was incubated with cells for 30 min. Pearson's values are labeled as R.

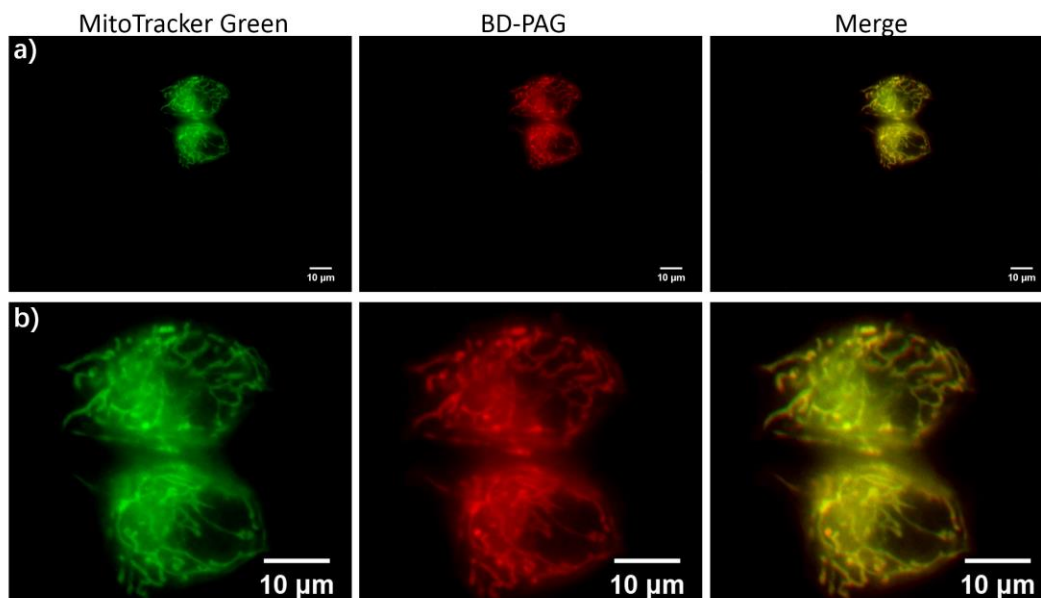


**Figure 3.7** Colocalization of BD-PAG in MCF-7 cells. MCF-7 cells were incubated with 2  $\mu\text{M}$  of BD-PAG at 37  $^{\circ}\text{C}$  for 30 min, 100 nM of MitoTracker Green was incubated with cells for 15 min before the cell imaging. Pearson's value  $R = 0.97$

### 3.2.3 Mitochondrial pH

To ascertain the mitochondrial pH regulating efficiency of BD-PAG, mitochondrial pH was measured by a pH-sensitive ratiometric fluorescent indicator, carboxy SNARF-1 AM, at various irradiation times of cells incubated with BD-PAG, using a fluorescence plate reader.<sup>116, 117</sup> The fluorescence intensities of carboxy SNARF-1 AM were measured at 590 nm and 650 nm. The data was plotted as a ratio of the emission intensities at 650 nm/590 nm (Figure 3.8), where the emission at 650 nm decreased with decreasing pH.<sup>118</sup>

The results exhibited a significant decrease of 650 nm/590 nm emission intensity ratio after the LED light irradiation, implying a mitochondrial pH decrease. This indicates that BD-PAG, under irradiation, is capable of generating H<sup>+</sup> that consequently lowers the mitochondrial pH. Meanwhile, the decrease of mitochondrial pH is dependent on both BD-PAG concentration and irradiation time. The decreasing ratio of 20 min irradiation of 20  $\mu$ M of BD-PAG indicates a 0.8 to 1.0 pH drop compared to the control group (Figure 3.8).<sup>119, 120</sup>

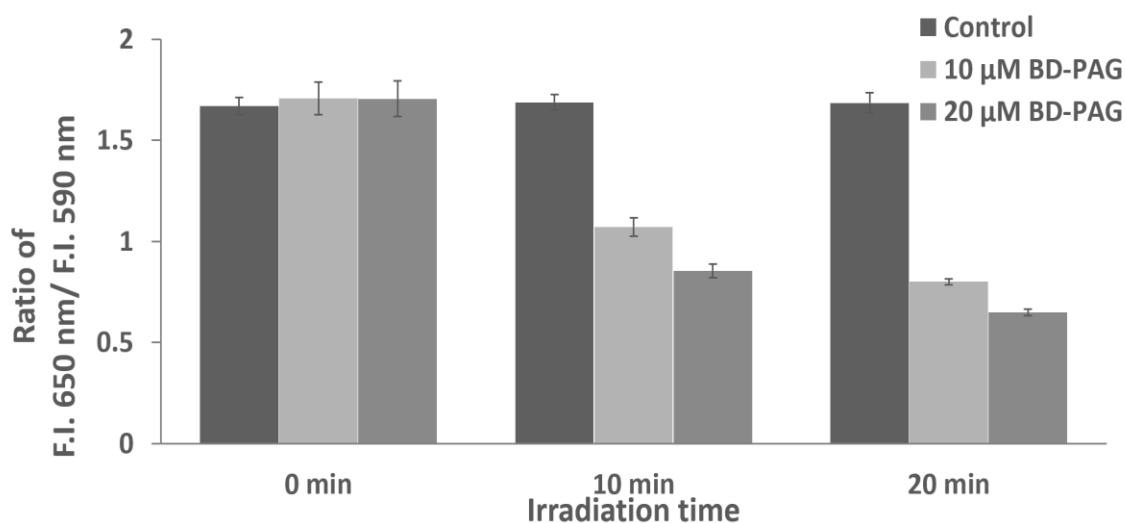


**Figure 3.8** Mitochondrial pH in HeLa cell. HeLa cells were incubated with with 10 and 20  $\mu$ M of BD-PAG for 4 h. The fluorescent of 590 nm and 650 nm were measured by plate reader at 488 nm excitation. Control group is HeLa cells with no BD-PAG treatment (N=5).

### 3.2.4 Mitochondrial Membrane Potential

To analyze the relevance of BD-PAG regulated mitochondrial pH with mitochondrial membrane potential change, the JC-1 mitochondrial membrane potential assay was performed. The fluorescence intensities of JC-1 at 530 nm and 590 nm were recorded as a ratio of 590 nm/530 nm emissions (Figure 3.9). JC-1 aggregates (emits at 590 nm) imply hyperpolarization of mitochondrial membrane, which increases  $\Delta\psi$ , while the depolarization of mitochondrial membrane (decrease of  $\Delta\psi$ ) is due to the JC-1 monomer (emits at 530 nm).<sup>121</sup> The JC-1 measurement results were consistent with mitochondrial pH changes. Moreover, the lipophilic cationic BD-PAG itself shows no impact to the membrane potential in the dark. This result indicates the mitochondrial membrane depolarization was caused by  $H^+$  release from BD-PAG upon irradiation, acidifying the mitochondria is was capable of regulating the proton gradient that drives mitochondrial membrane depolarization.<sup>122</sup>

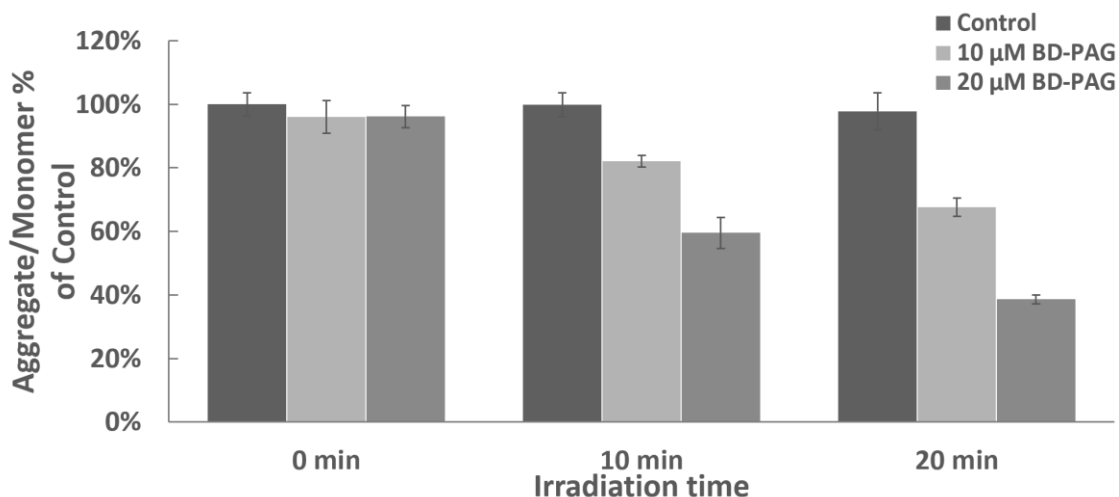


**Figure 3.9** Mitochondrial membrane potential in HeLa cell. HeLa cells was incubated with 10 and 20  $\mu$ M of BD-PAG for 4 h. The fluorescent of 530 nm and 590 nm were measured by plate reader at 475 nm excitation. Control group is HeLa cells with no BD-PAG treatment. HeLa cells with no irradiation and treatment was classified as 100%. (N=6)

### 3.2.5 Irradiation Time-Dependent Time-Lapse Cell Imaging

Irradiation time-dependent time-lapse cell imaging was performed in HeLa cells to observe the mitochondrial morphology change under the photo-triggered  $H^+$  release. Cells incubated with BD-PAG were irradiated with laser light directly by the fluorescent microscope (prox. Power density  $\sim 4.9 \text{ W/cm}^2$ ) from 0 to 50 s with a PAG concentration of 10 and 20  $\mu\text{M}$ , separately (Figures 3.10 and 3.11, respectively). Interestingly, the time-lapse images exhibit a filamentous to punctate mitochondrial dynamic transition during the light irradiation.

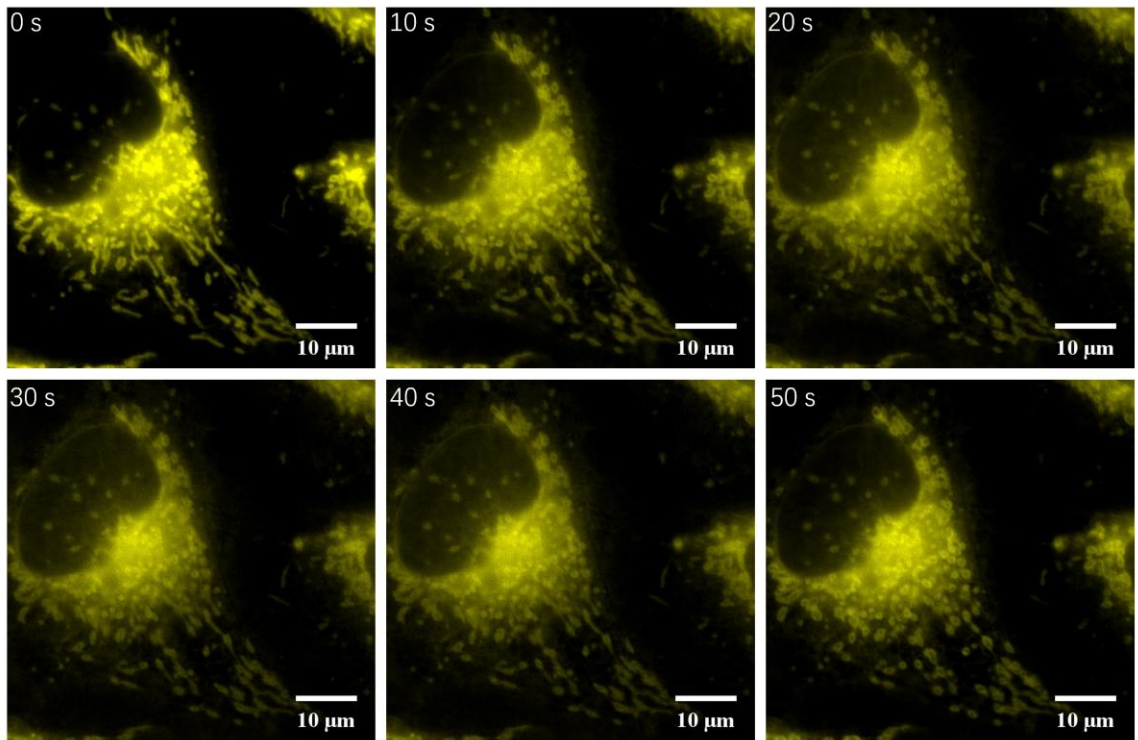


**Figure 3.10** 20  $\mu\text{M}$  of BD-PAG treated time lapse cell imaging. HeLa cells were treated with 20  $\mu\text{M}$  of BD-PAG for 30 min. After washed out BD-PAG, time lapse cell imaging was captured every 10 s.

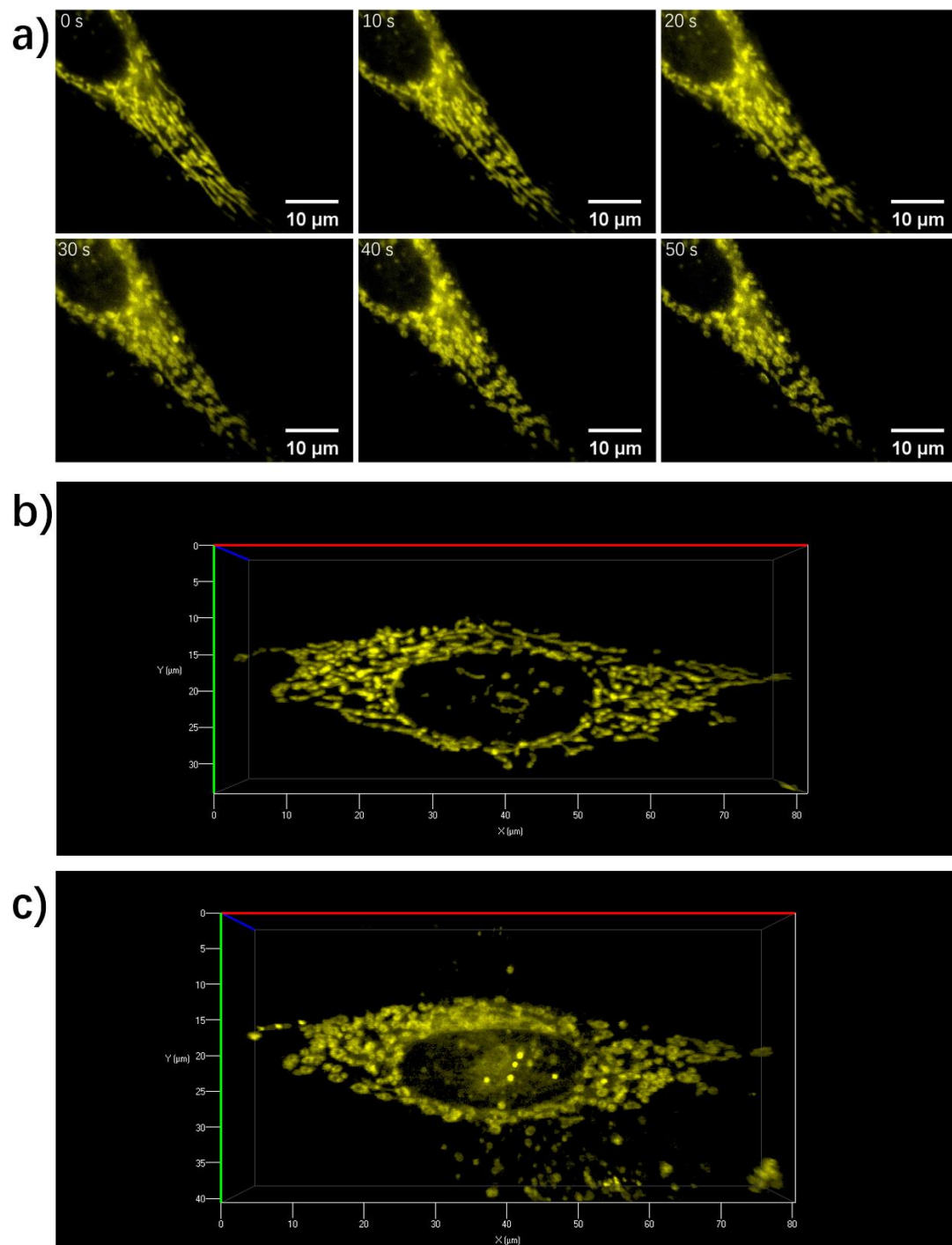


**Figure 3.11** Time lapse and Z-stack cell imaging. a) Time lapse cell imaging of HeLa cells treated with 10  $\mu\text{M}$  of BD-PAG. After washed out BD-PAG, time lapsed cell images were captured every 10 s while the cells were under irradiation in the whole course. 3D image captured by confocal microscope before b) and after c) 50 s of light irradiation.

Furthermore, the Z-stack of the starting time point and irradiation ending time point cell images (Figure 3.11b and c) present a significant mitochondrial morphology difference, displaying that most of the mitochondria transformed from the filamentous-like to punctate-like morphology after 50 s. Although the mitochondrial morphology appears to be diverse, especially in cancer cells,<sup>123</sup> this phenotypic change from filamentous to punctate has been shown to be intimately involved in apoptosis under stressful conditions.<sup>124-126</sup> This transition may be caused by the MOMP increase and apoptosis initiation, which is induced by mitochondrial membrane depolarization. This set of data further supports the potential of photo-triggered BD-PAG to regulate mitochondrial pH and depolarize the mitochondrial membrane.

### **3.2.6 Caspase 3/9 Assay**

To further evaluate BD-PAG-regulated depolarization and the MOMP reinforcement, caspase 3/9 assays were performed in HeLa cells. Cytochrome c is the key protein to initiate the intrinsic apoptosis pathway that is localized in the compartment between the inner and outer mitochondrial membranes.<sup>127, 128</sup> The reinforced MOMP leads cytochrome c to be released from the mitochondrial membrane, resulting in a caspase cascade that activates caspase 9, then, in turn, caspase 9 activates caspase 3 and 7 to induce cell apoptosis.<sup>129</sup> Both caspase 3 and 9 exhibited a strong increase after light irradiation (Figure 3.12), while the group of BD-PAG with no irradiation (kept in the dark) showed no significant difference relative to the blank. This downstream apoptosis pathway activation provides confirmation of cytochrome c release from mitochondria, and support of the occurrence for mitochondrial membrane depolarization and MOMP reinforcement.

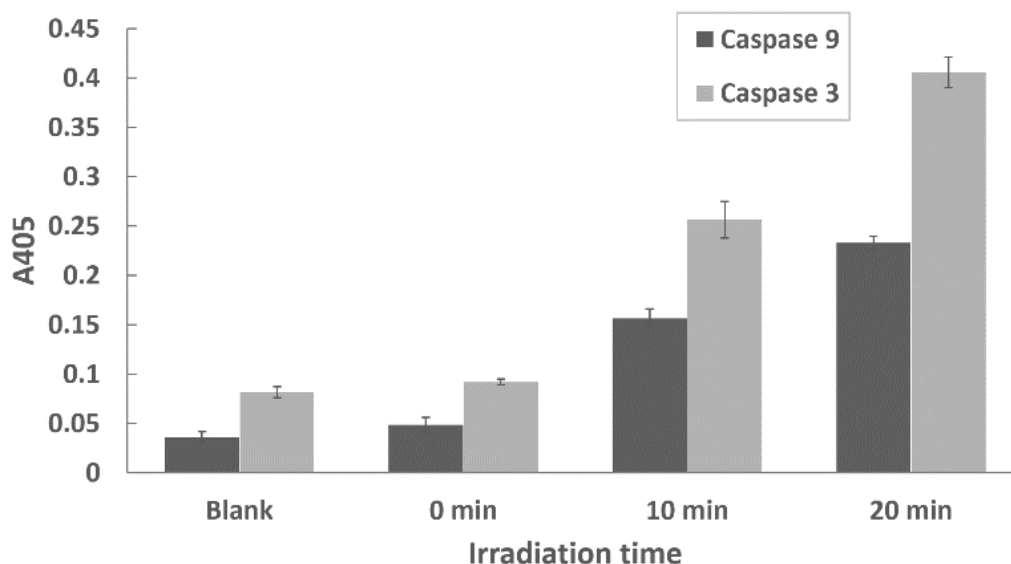


**Figure 3.12** Irradiation time dependent caspase 3/9 assay of HeLa cells treated with 10  $\mu$ M of BD-PAG for 4 h. Blank group is HeLa cells with no BD-PAG. (N=3).

### 3.2.7 Combined Drug Therapy

The capability of photo-triggered  $H^+$  release from BD-PAG to overcome anti-cancer drug resistance was examined by irradiation time-dependent combined drug therapy with chlorambucil (Cbl). Anti-cancer drug Cbl is a potent alkylating agent that is primarily used to treat chronic lymphocytic leukemia. Its drug resistant mechanism is due to the tumor suppressor gene P53 mutation or under-expression, which inhibits the apoptosis pathway and results in mitochondrial membrane hyperpolarization and MOMP reduction.<sup>130-132</sup> The cell viability of chlorambucil and/or BD-PAG were measured with both HeLa and MCF-7 cell lines (Figures 3.13 and 3.14). In the BD-PAG and Cbl combination therapy study, we found out the therapeutic efficiency of Cbl was remarkably increased with PB-PAG upon light activation, and the IC<sub>50</sub> of Cbl was reduced to 5  $\mu$ M when compared with the reported IC<sub>50</sub> in HeLa and MCF-7 at 100  $\mu$ M.<sup>133, 134</sup> We reason that the photo-triggered BD-PAG caused mitochondrial membrane depolarization and MOMP reinforcement attenuated drug resistance and significantly enhanced the therapeutic efficiency of Cbl.

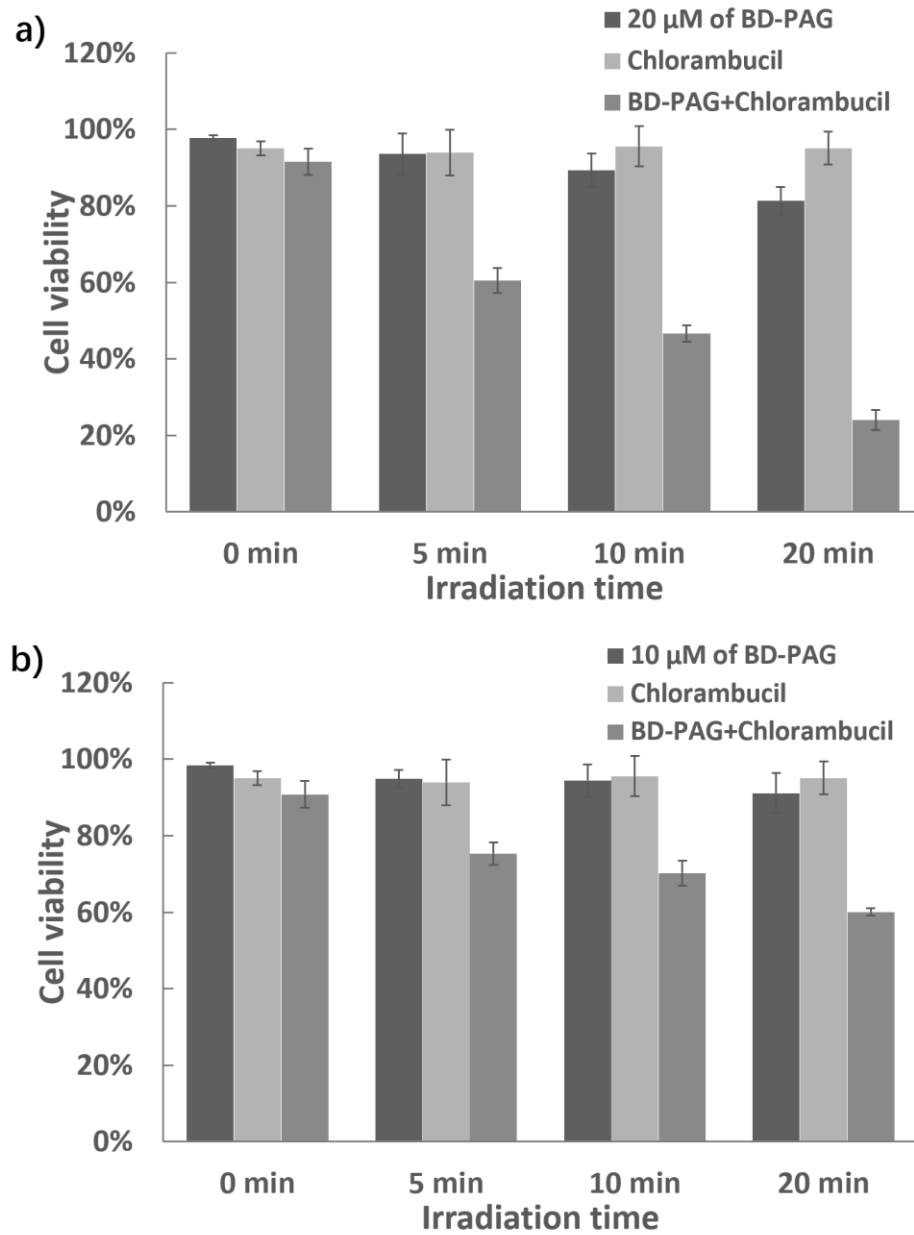


**Figure 3.13** Irradiation time dependent combined drug therapy on HeLa cells after treatment with 5  $\mu$ M of Cbl and BD-PAG in varied concentration. a) HeLa cells with 20  $\mu$ M of BD-PAG upon LED light irradiation. b) HeLa cells with 10  $\mu$ M of BD-PAG upon LED light irradiation. HeLa cells with no irradiation and treatment classified as 100%. (N=6).

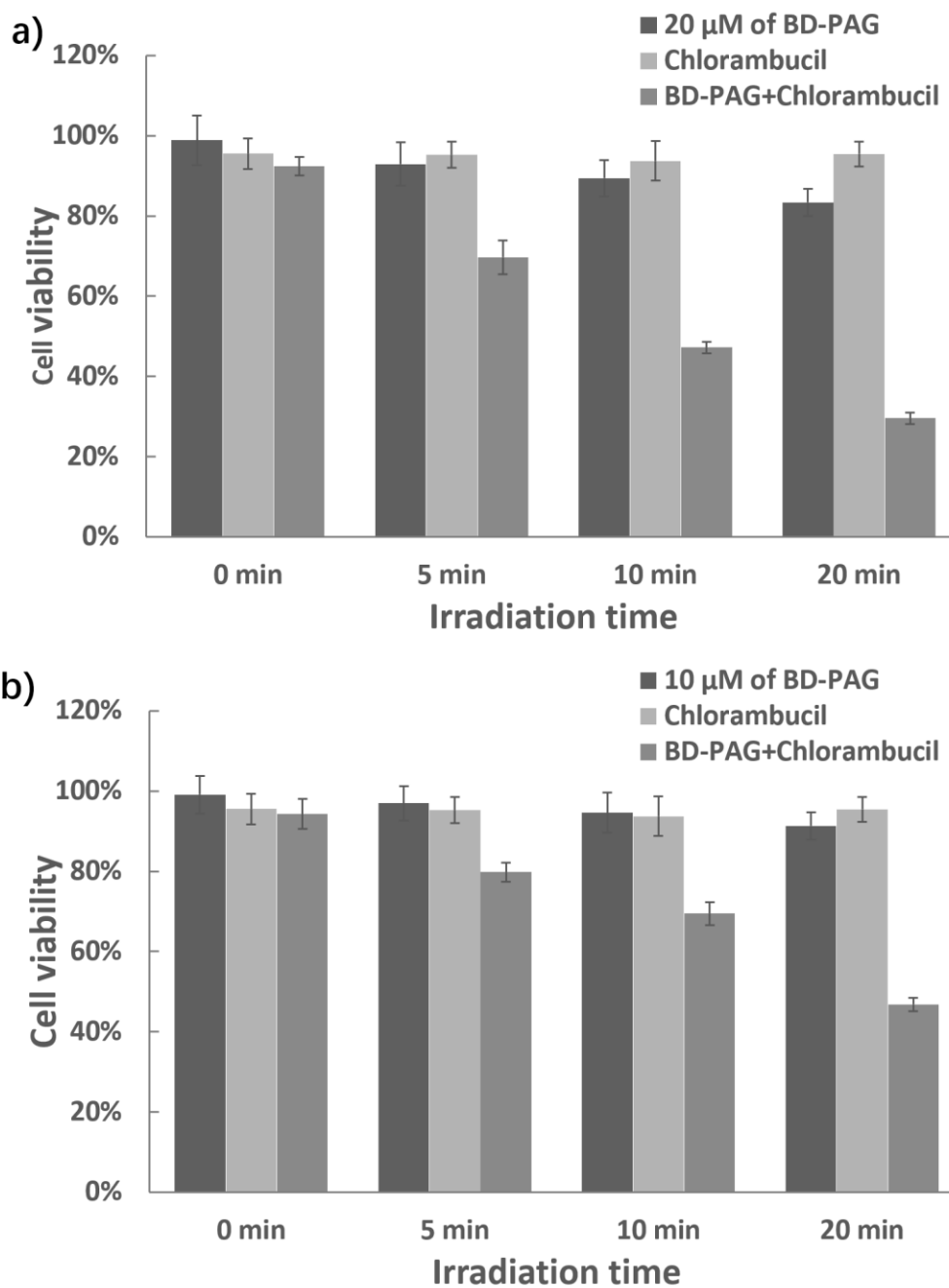


**Figure 3.14** Irradiation time dependent combined drug therapy on MCF-7 cells after treatment with 5  $\mu$ M of Cbl and BD-PAG in varied concentration. a) MCF-7 cells with 20  $\mu$ M of BD-PAG upon LED light irradiation. b) MCF-7 cells with 10  $\mu$ M of BD-PAG upon LED light irradiation. MCF-7 cells with no irradiation and treatment classified as 100%. (N=6).

### **3.3 Materials and Methods**

#### **3.3.1 Materials and General Equipments**

BD-PAG was synthesized according to our previous reported procedures. All other reagents and solvents were purchased from commercial suppliers and used without further purification. UV-vis absorption spectra, mitochondrial pH and potential were recorded on a Tecan Infinite M200 PRO plate reader spectrometer. Fluorescence emission spectra were measured using an FLS980 fluorescence spectrometer. Cell images were recorded on an Olympus IX-81 DSU microscope equipped with a Hamamatsu EMCCD C9100 digital camera. Z-stack cell images were captured by a Zeiss confocal microscope. All the cell images were issued by Fiji, a freely available image processing software.

#### **3.3.2 Cell Culture**

Human cervical cancer cell HeLa and human breast cancer cell MCF-7 cell lines were cultured in Dulbecco's Modified Eagle Medium (DMEM) supplemented with 10% fetal bovine serum, 1% penicillin/streptomycin at 37 °C in a humidified 5% CO<sub>2</sub> incubator.

#### **3.3.3 Dark Cell Viability**

To assess the cytotoxicity of BD-PAG, HeLa cells and MCF-7 cells were cultured in the Dulbecco's modified Eagle's medium (DMEM) cell medium supplemented with 10% fetal bovine serum, 1% penicillin, and streptomycin at 37 °C and 5% CO<sub>2</sub>. Cells were placed in 96 well plates and incubated until there were no fewer than  $5 \times 10^3$  cells per well for the experiments. Next, cells were incubated with different concentrations of BD-PAG (1, 2.5, 5, 10, 20, 40 and 80  $\mu$ M) 24 h, where the values within parentheses refer to

the nominal concentrations of the surfactants. After 22 h incubation, 20  $\mu\text{L}$  of the Cell Titer 96 Aqueous One solution reagent (for MTS assay) was added into each well, followed by further incubation for 2 h at 37  $^{\circ}\text{C}$ .

The respective absorbance values were read on a Tecan Infinite M200 PRO plate reader spectrometer at 490 nm. Cell viabilities were calculated based on of the following equation

$$\text{Cell Viability}(\%) = \frac{\text{Abs}_{490\text{nm}}^{\text{S}} - \text{Abs}_{490\text{nm}}^{\text{D}}}{\text{Abs}_{490\text{nm}}^{\text{C}} - \text{Abs}_{490\text{nm}}^{\text{D}2}} \times 100\% \quad (3.1)$$

where  $\text{Abs}_{490\text{nm}}^{\text{S}}$  is the absorbance of the cells incubated with different concentrations of experimental probe solutions,  $\text{Abs}_{490\text{nm}}^{\text{D}}$  is the absorbance of cell-free well containing only BD-PAG at the concentration that was studied,  $\text{Abs}_{490\text{nm}}^{\text{C}}$  is the absorbance of cells alone incubated in the medium,  $\text{Abs}_{490\text{nm}}^{\text{D}2}$  is the absorbance of the cell-free well.

### 3.3.4 Time Dependent Cell Viability and Combined drug therapy

To assess the photolysis cytotoxicity of BD-PAG, cells were placed in 96 well plates and incubated until there were no fewer than  $5 \times 10^3$  cells per well for the experiments. Next, cells were incubated with 10  $\mu\text{M}$  and 20  $\mu\text{M}$  of BD-PAG separately for 4 h. Then, BD-PAG was removed and regular DMEM was added for further incubation. After that, cells were placed under the 595 nm LED lamp (power density  $\sim 80 \text{ mW}/\text{cm}^2$ ) with 1 cm distance for various irradiation time (0, 5, 10, 20 min). Then chlorambucil was added in chlorambucil + BD-PAG group and an additional 22 h incubation was performed after the irradiation, except control group which had no BD-PAG or chlorambucil treatment. And chlorambucil group had not incubate with BD-PAG. 20  $\mu\text{L}$  of the Cell Titer 96

Aqueous One solution reagent (for MTS assay) was added into each well, followed by further incubation for 2 h at 37 °C.

The respective absorbance values were read on a Tecan Infinite M200 PRO plate reader spectrometer at 490 nm. Cell viabilities were calculated based above equation.

### **3.3.5 Cellular Uptake and Colocalization**

To investigate the efficiency and specificity of BD-PAG, HeLa and MCF-7 cells were employed. All cells were seeded on confocal dish (MatTek) at the density of  $4 \times 10^4$  cells per dish and incubated for 24 h at 37 °C. Stock solutions of BD-PAG dissolved in DMSO were prepared at a nominal concentration of  $10^4 \mu\text{M}$ . The stock solution was diluted to 2  $\mu\text{M}$  with the DMEM cell medium and freshly placed over cells for 30 min incubation period. Cells were washed three times with PBS and further incubated with MitoTracker Green (MT Green), LysoTracker Green (LT Green), or ER-tracker Green (ER Green) separately before cell imaging. Cells were then washed with PBS three times, and then the live cell imaging solution (Molecular Probes) was added to confocal dishes. Fluorescence images were obtained using an inverted Olympus IX70 microscope coupled with a FITC filter cube (Ex: 482/40; DM: 506; Em: 534/40) for MT green, LT green, or ER Green, and a TRITC filter cube (Ex: 532/40; Em: 585/40) for BD-PAG. Bright field, commercial tracker field and BD-PAG field were obtained, and Pearson's correlation coefficients were issued by Fiji, freely available image processing software.

### **3.3.6 Mitochondrial pH Measurement**

For measuring the mitochondrial pH, HeLa cells were employed and seeded on petri-dish at the density of  $1 \times 10^6$  cells per dish and incubated for 24 h at 37 °C. Then, HeLa cells were incubated with 10  $\mu\text{M}$  of carboxy SNARF-1 AM for 30 min. Cells were washed

three times with PBS and incubated with 10 and 20  $\mu\text{M}$  of BD-PAG for 4 h respectively. After washing out the BD-PAG, cells were irradiated various time (0, 10, and 20 min) by 595 nm LED lamp separately. HeLa cells were removed to 96 well plate for measuring fluorescent intensity at 590 and 650 nm with 488 nm excitation using a Tecan Infinite M200 PRO plate reader spectrometer.

### **3.3.7 Mitochondrial Membrane Potential Measurement**

For measuring the mitochondrial pH, HeLa cells were employed and seeded on petri-dish at the density of  $1 \times 10^6$  cells per dish and incubated for 24 h at 37 °C. Then, HeLa cells were incubated with 10 and 20  $\mu\text{M}$  of BD-PAG at 37 °C for 4 h respectively. Control groups were HeLa cells without BD-PAG treatment. Cells were washed three times with PBS and irradiated various time (0, 10, and 20 min) by 595nm LED lamp separately. Cells were incubated with 5  $\mu\text{M}$  of JC-1 at 37 °C for 10 min, then JC-1 was washed out. HeLa cells were transferred to a 96 well plate for measuring fluorescence intensity at 530 and 590 nm with 475 nm excitation using a Tecan Infinite M200 PRO plate reader spectrometer.

### **3.3.8 Time Lapse and Z-stack Cell Imaging**

To observe mitochondrial morphological changes during the BD-PAG photolysis, HeLa cells were employed. All cells were seeded on confocal dish (MatTek) at a density of  $4 \times 10^4$  cells per dish and incubated for 24 h at 37 °C. HeLa cells were incubated with 10 and 20  $\mu\text{M}$  of BD-PAG for 30 min, respectively. Control groups were HeLa cells without BD-PAG treatment. Cells were washed three times with PBS and the live cell imaging solution (Molecular Probes) was added to confocal dishes. BD-PAG was irradiated directly by the lamp source of the microscope (power density  $\sim 4.9 \text{ W/cm}^2$ ), and time-

lapse cell imaging was recorded every 10 s. Z-stack cell imaging was captured by Zeiss confocal microscope before and after the irradiation.

### **3.3.9 Caspase 3 and Caspase 9 measurements**

To further assess cytochrome c release and caspase 3/9 activation, caspase 3 and caspase 9 assays were performed in HeLa cells. HeLa cells were mounted on petri-dishes at a density of  $1 \times 10^6$  cells per dish, and incubated for 24 h at 37 °C. Then, cells were incubated with 10  $\mu$ M of BD-PAG at 37 °C for 4 h. The blank group was HeLa cells without BD-PAG treatment. Cells were washed three times with PBS and irradiated various time (0, 10, and 20 min) by 595 nm LED lamp separately, followed by further incubation for 18 h. Caspase 3/9 assays using the corresponding kits were performed and transferred to a 96 well plate for further incubation. Then, 405 nm absorption was measured Tecan Infinite M200 PRO plate reader spectrometer.

## **3.4 Conclusion**

In conclusion, the mitochondria targetable pH interference was demonstrated using BD-PAG under red LED light. We demonstrate the capability of photo-triggered BD-PAG release proton ( $H^+$ ) to regulate mitochondrial pH. The acidified mitochondria triggered mitochondrial membrane depolarization. The mitochondrial morphology transition and caspase cascade activation further demonstrated that mitochondrial pH decrease leads the MOMP increase in which the depolarization of mitochondrial membrane caused reinforced MOMP release of cytochrome C to activate apoptosis pathways. Overcoming cancer chemotherapeutic drug resistance was observed by a combination drug therapy, in which the drug efficiency of Cbl was significantly enhanced by lowering the

mitochondrial pH. This study represents a promising strategy to regulate mitochondrial pH by using a mitochondria-targeted photoacid generator to overcome cancer drug resistance.

## CHAPTER 4

### PHOTO-UNCAGING OF BODIPY OXIME ESTER FOR HISTONE DEACETYLASES INDUCED APOPTOSIS IN TUMOR CELLS

Photo-removable protecting groups, or caging groups, enable one to regulate the activities of bioactive molecules in living cells upon light irradiation. The basic idea behind the caging technique is that molecules of interest can be inactive when protected with photo-caging functional groups, then, after light irradiation, the molecules of interest can be freed and act in an intact form. Herein, a new class of BODIPY-based oxime ester photo-uncaging group was constructed to release aliphatic/aromatic carboxylic acids. Upon green light (~ 500 nm) irradiation, oxime esters resulted in N–O bond scission to generate cyano-photoproducts and release cargo molecules. Photophysical properties of BODIPY-based oxime esters were investigated via ultraviolet–visible absorption and fluorescence spectroscopy. Further, we constructed a photo-uncaging drug delivery system to release valproic acid (VPA), a drug that can inhibit histone deacetylases and induced apoptosis in tumor cells. *In vitro* study reveals that our photo-uncaging system exhibited better cellular uptake, biocompatibility, and photo-regulated drug release for enhanced toxicity in tumor cells.

#### 4.1 Introduction

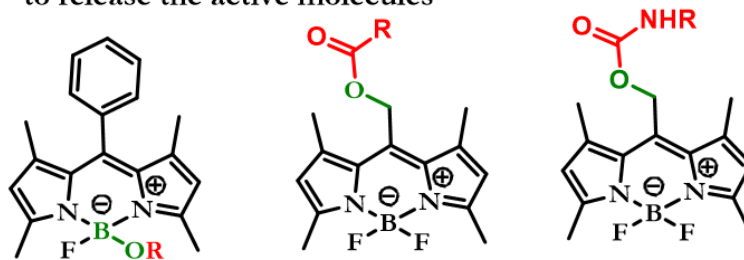
Photo-removable protecting groups, or caging groups, enable scientists to regulate the activities of bioactive molecules in living cells upon light irradiation. The basic idea behind the caging technique is that molecules of interest can be inactive with photo-caging groups, after light irradiation the molecules of interest can be freed

and act in an intact form. This approach has been used for drug delivery and exhibits pinpoint accuracy with light guidance as well as low off-target toxicity.<sup>135-137</sup> However, most of the uncaging groups show absorbability in UV-to-blue region (300–450 nm), which leads to shallow tissue penetration depth and increased photo toxicity caused by high energy radiance. Thus, there is a strong need for uncaging groups that operate in longer wavelength windows.<sup>138</sup>

Boron-dipyrromethene (BODIPY) derivatives were identified as one of the potential chromophore for photo-uncaging, which absorbs in the visible region with high molar extinction coefficient and resistance to photo bleaching.<sup>139, 140</sup> Most of the reported BODIPY uncaging groups undergo heterolytic C–O or B–O bond cleavage to release the active molecules (carboxylic acid, amine, and phenol) (Figure 4.1a). For example, Prof. Urano's group developed a novel BODIPY uncaging group where B–O bond cleave (photo elimination reaction) releases the active molecule from the chromophore.<sup>141, 142</sup> In addition, Smith and winter et al. reported meso-substituted BODIPY dyes that release acetic acid under green light at wavelength ~500 nm via the dissociation of C–O bond.<sup>143</sup> Further, extended conjugation meso-BODIPY was reported for uncaging of active molecule through C–O bond cleavage with moderate photochemical quantum yield.<sup>144, 145</sup> Meanwhile, in order to improve the photo-uncaging efficiency, halogen (I/Br) substituted BODIPY has been used, in which the heavy atoms promote intersystem crossing (ISC) to a triplet surface, and consequently allows more time for uncaging.<sup>146-149</sup> However, the halogen substitution can encourage reactive oxygen species (ROS), and consequently interfere with biological samples. Thus, there is a great need to develop photo-uncaging systems with high uncaging efficiencies.

a. Previous works:

Green light activated B-O, C-O bond cleavage  
to release the active molecules



b. Present work:

Green light activated N-O bond cleavage  
to release the active molecules

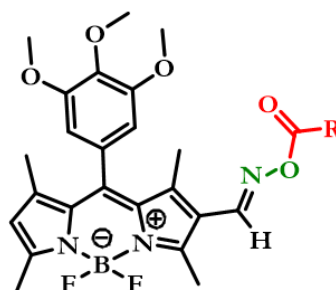


**Figure 4.1** Schematic representation of (a) reported green light activated C-O and B-O cleavage photo-uncaging groups, and (b) our new green light activated N-O cleavage photo-uncaging approach.

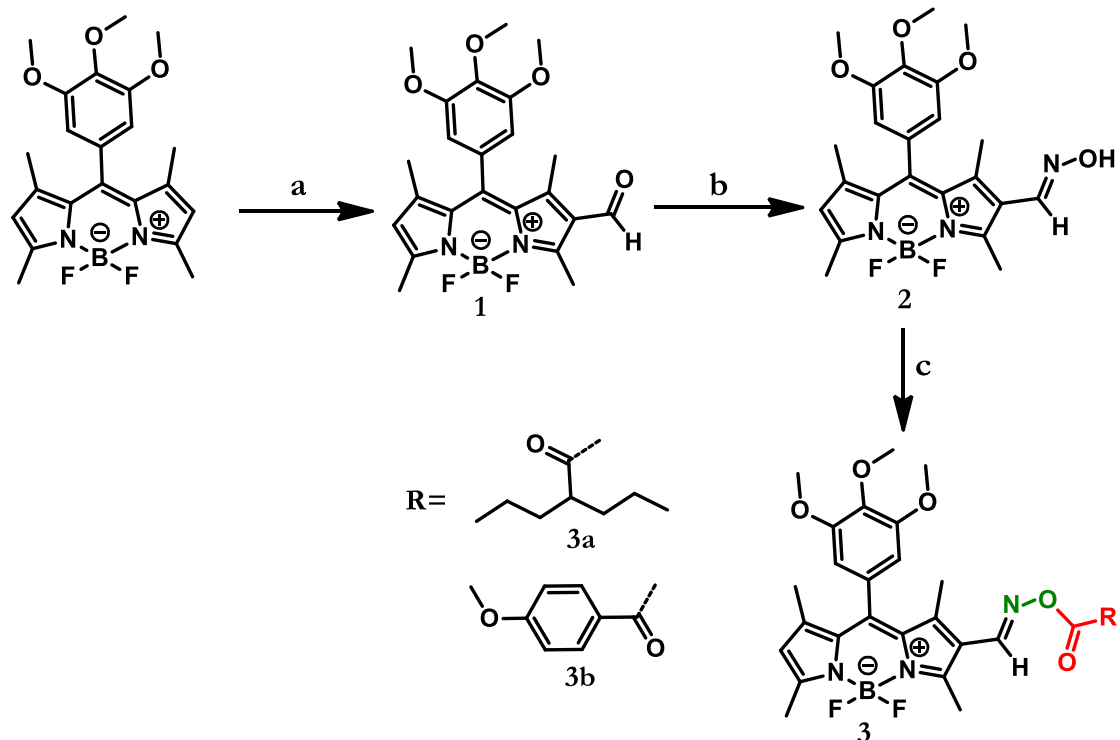
The photochemistry of oxime esters was well studied in the literature for a decade. Direct irradiation of oxime ester resulted in N–O bond scission to generate iminyl and caged radical pair.<sup>150, 151</sup> The generated radical pair in aqueous polar protic solvent, subsequently abstracts hydrogen from the solvent to release the caged molecule.<sup>152, 153</sup> In this work, we take advantage of the weak N-O bond of oxime ester to promote the photo-uncaging via coupling with BODIPY chromophore. With this intension, we designed a BODIPY oxime ester as a new photon-uncaging platform that can photo-uncage both aromatic and aliphatic carboxylic acids (Figure 4.1b).

For the caged cargo molecule, we chose p-methoxy benzoic acid to represent aromatic acid and valproic acid (VPA) as an example of aliphatic acid. In addition, VPA is a small fatty acid, primarily used to treat epilepsy and bipolar disorder and to prevent migraine headaches.<sup>154</sup> Recently, VPA was identified as an inhibitor of histone deacetylase (HDAC), emerging as a potential anticancer agent to induce cell apoptosis.<sup>155, 156</sup> However, preclinical and clinical research indicates that using VPA directly (without specific targeting) has multiple side effects and even fatal risks.<sup>157, 158</sup> Herein, we demonstrated that our BODIPY oxime ester caged valproic acid (**3a**) could be used as a new platform for light guided cancer treatment. We found compound **3a** can be uptaken by cells and accumulate in the areas close to the nucleus. Upon irradiation, **3a** can effectively release VPA (from N-O cleavage) inside tumor cells, and, consequently, induce apoptosis and lead to tumor cell death.

## 4.2 Results and Discussion

### 4.2.1 Synthetic Strategy

First, a BODIPY core was synthesized using a literature method by reacting 3,4,5-trimethoxybenzaldehyde with 2,4-dimethylpyrrole.<sup>159</sup> Next, a Vilsmeier–Haack formylation reaction of the BODIPY core gave compound **1** with the aldehyde functional group, which was then treated with NH<sub>2</sub>OH.HCl in EtOH at reflux temperature to yield BODIPY-oxime parent compound **2**. Reaction of **2** with acid chloride derivatives afforded the corresponding BODIPY oxime esters, **3a** and **3b**, with caged VPA and p-methoxy benzoyl, respectively. (Figure 4.2)



**Reagents:** a) DMF/ $\text{POCl}_3$ /-5 C; b)  $\text{NH}_2\text{OH}\cdot\text{HCl}$ /ethanol; c) 3a: Triethylamine/ DCM/ 2-propylpentanoyl chloride, 3b: p-methoxy benzoyl chloride/Triethylamine/ DCM.

**Figure 4.2** Synthesis route of BODIPY oxime ester **3a** and **3b**.

#### 4.2.2 Photophysical Properties

UV-vis absorption and emission spectra were then measured using BODIPY oxime esters (**3a**, **3b**) in methanol. The absorption spectra of **3a** and **3b** show intense peak centered at 507 ( $\epsilon = 52800 \text{ M}^{-1}\text{cm}^{-1}$ ) and 516 nm ( $\epsilon = 57600 \text{ M}^{-1}\text{cm}^{-1}$ ) (Figure 4.3). With the emission maximum centered at 521 and 562 nm, respectively. Fluorescence quantum yields ( $\Phi_f$ ) were calculated using fluorescein as standard.  $\Phi_f$  of **3a** and **3b** were determined to be 0.09 and 0.12, respectively. The low  $\Phi_f$  values are attributed to the presence of  $^3n-\pi^*$  in the vicinity of lowest  $^1\pi-\pi^*$  excited state. Hence, inter-system crossing occurs in competition with fluorescence.<sup>159</sup>

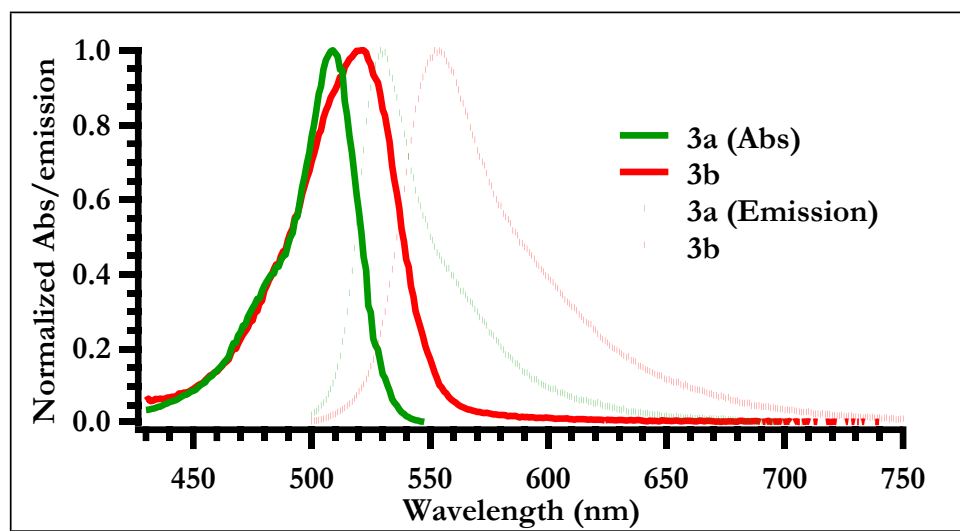


**Figure 4.3** Normalized absorption and emission spectra of compound **3a** and **3b** in methanol.

**Table 4.1** Photophysical Properties for Compound **3a** and **3b**

Sample	$\lambda_{\text{abs}}^a$ [nm]	$\lambda_{\text{em}}^a$ [nm]	$\epsilon^b$ [ $\text{M}^{-1}\text{cm}^{-1}$ ]	$\Phi_{\text{flu}}^c$	$\tau^d$ [ns]	$\Phi_{\text{un}}^e$ [ $\times 10^4$ ]	$\epsilon\Phi_{\text{un}}$
<b>3a</b>	507	521	52800	0.09	0.6	7.2	38
<b>3b</b>	516	562	57600	0.12	0.7	5.2	30

<sup>a</sup> Absorption and emission maxima; <sup>b</sup> molar absorption coefficients; <sup>c</sup> fluorescent quantum yield; <sup>d</sup> fluorescence lifetimes; <sup>e</sup> photo-uncaging quantum yield.

Next, the photo-uncaging abilities of BODIPY oxime esters were studied with UV-vis spectroscopy. We irradiated the BODIPY oxime esters ( $1.0 \times 10^{-5}$  M of **3a** and **3b**) in MeOH/H<sub>2</sub>O (7/3, v/v) solution with LED light ( $503 \pm 30$  nm, power density of  $\sim 80$  mW/cm<sup>2</sup>), and UV-vis spectra were recorded at different time intervals. Decreases of the absorbance intensities were observed after irradiation, which were attributed to the photolysis of the compound (Figures 4.4). We measured the photo-uncaging quantum yields ( $\Phi_{\text{un}}$ ) for **3a** and **3b** using a reported procedure,<sup>145, 160</sup> and compared with previously reported BODIPY based photo-uncaging platforms ( $\Phi_{\text{un}} = 1.5 - 6.3 \times 10^{-4}$  for C-O bond and  $\Phi_{\text{un}} = 3.0 \times 10^{-4}$  for B-O bond), the newly synthesized oxime ester photo-uncaging

quantum yields are  $7.2 \times 10^{-4}$ , and  $5.2 \times 10^{-4}$  for compound **3a** and **3b**, respectively.<sup>143, 144,</sup>  
<sup>149</sup> Further, the rate of photo-uncaging was expressed in the function of quantum efficiency parameter ( $\epsilon\Phi_{un}$ ), and  $\epsilon\Phi_{un}$  values are 38 and 30 for compound **3a** and **3b**, respectively. The higher photo-uncaging quantum yield compared with reported ones is attributed to the weak N-O bond in the oxime ester. The photophysical properties of **3a** and **3b** are summarized in Table 4.1.

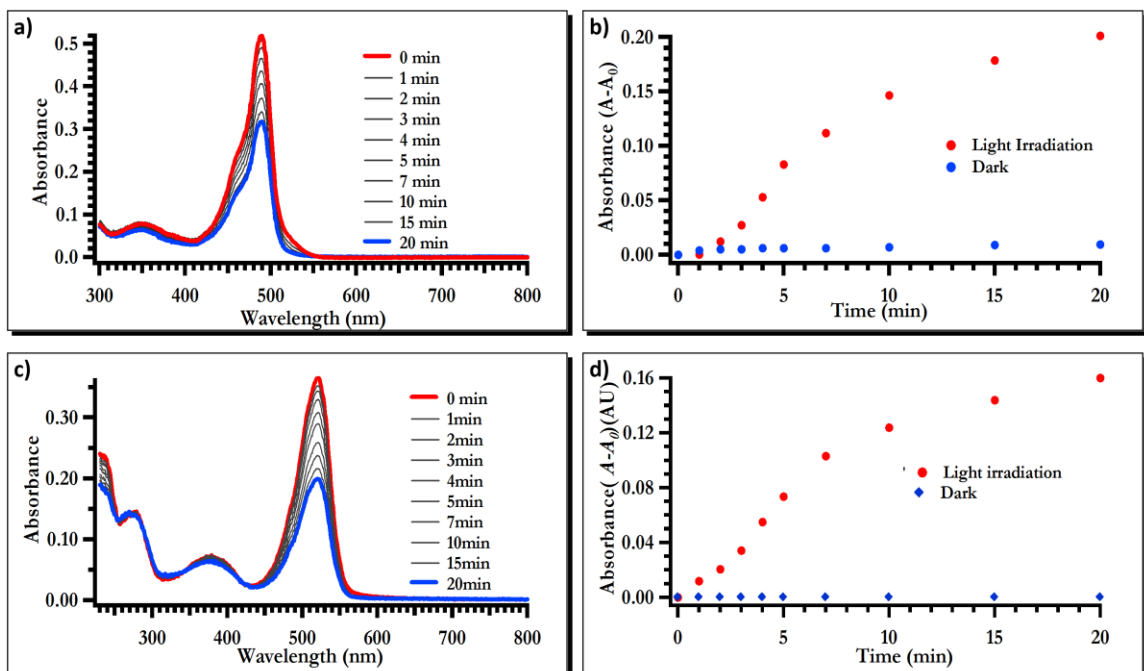


**Figure 4.4** a) UV-Vis spectra of photorelease from compound **3a** in MeOH/Water. (7/3 v/v) b) Absorbance at 505 nm Vs time is plotted, for compound **3a**. c) UV-Vis spectra of photorelease from compound **3b** in MeOH/Water. (7/3 v/v) d) Absorbance at 505 nm Vs time is plotted, for compound **3b**.

To verify the photo-uncaging reaction process, we then used compound **3a** as an example, and studied the mechanism and kinetics by following the uncaging procedure with HPLC and  $^1\text{H}$  NMR. **3a** solution in methanol/ $\text{H}_2\text{O}$  (7:3 v/v,  $1.0 \times 10^{-5}$  M) was irradiated with LED light ( $\lambda = 503 \pm 30$  nm,  $\sim 80$  mW/cm<sup>2</sup>), and the photolyase was taken

at regular intervals of time to HPLC analysis. Before light irradiation (0 min), BODIPY oxime ester showed a retention time of 5.6 min in HPLC. After 10 min under green LED light, the major peak shifted to 6.6 min (Figure 4.5). To further confirm the structure of the photoproduct, we followed the course of the photo-uncaging using  $^1\text{H}$  NMR. Aqueous suspension of the photolyase was taken after 10 min of irradiation ( $\lambda = 503 \pm 30$  nm,  $\sim 80$  mW/cm $^2$ ) and was extracted to perform  $^1\text{H}$  NMR. By comparing the  $^1\text{H}$  NMR of **3a**, and the photolyase mixture (Figure 4.6), it was observed that the oxime proton of **3a** decreased in intensity at 8.33 ppm. Further, the BODIPY- $\beta$ -proton of **3a** at 6.12 ppm was decreased in intensity and new signal emerged at 6.18 ppm, which belongs to the photoproduct of 2-cyano-BODIPY (Figure 4.7). The peaks intensity ratio of the  $\beta$ -protons ( $c'$  and  $c$ , integration ratio 1.5:1) (Figure 4.6) shows that 60% of **3a** has been photolysis to become 2-cyano-BODIPY upon light irradiation of 10 min. In addition, we also noticed the appearance of a new multiplet at 2.41 ppm, corresponding to the tertiary proton of the released VPA.

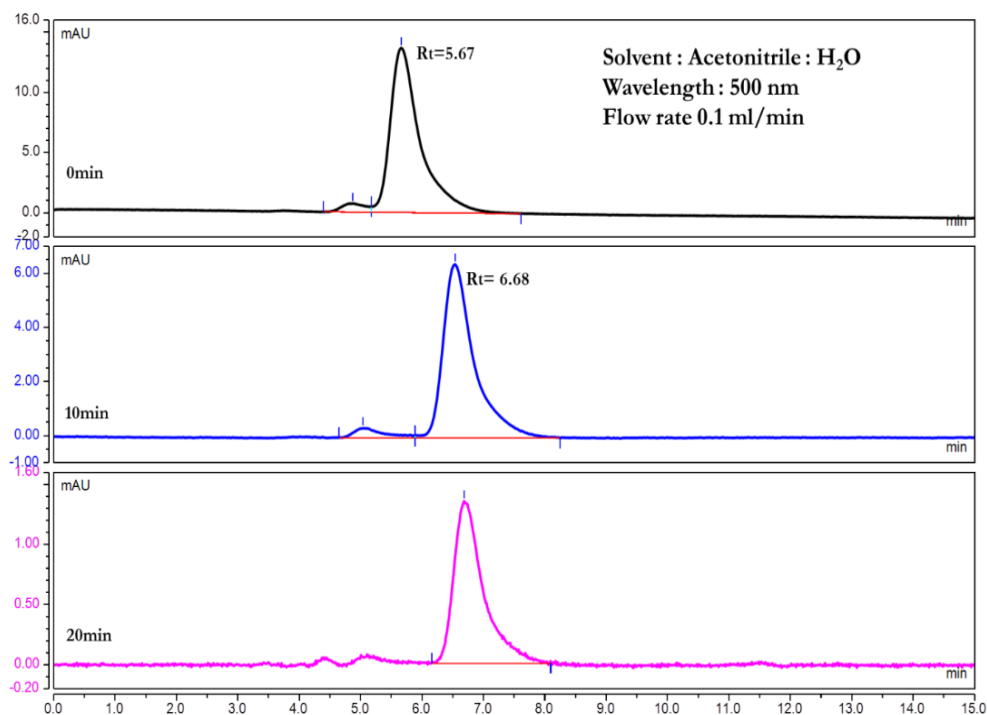


**Figure 4.5** The LC-MS profile of time-dependent photo-uncaging **3a** using green LED (505 nm) irradiation, time point of 0, 10 and 20 min

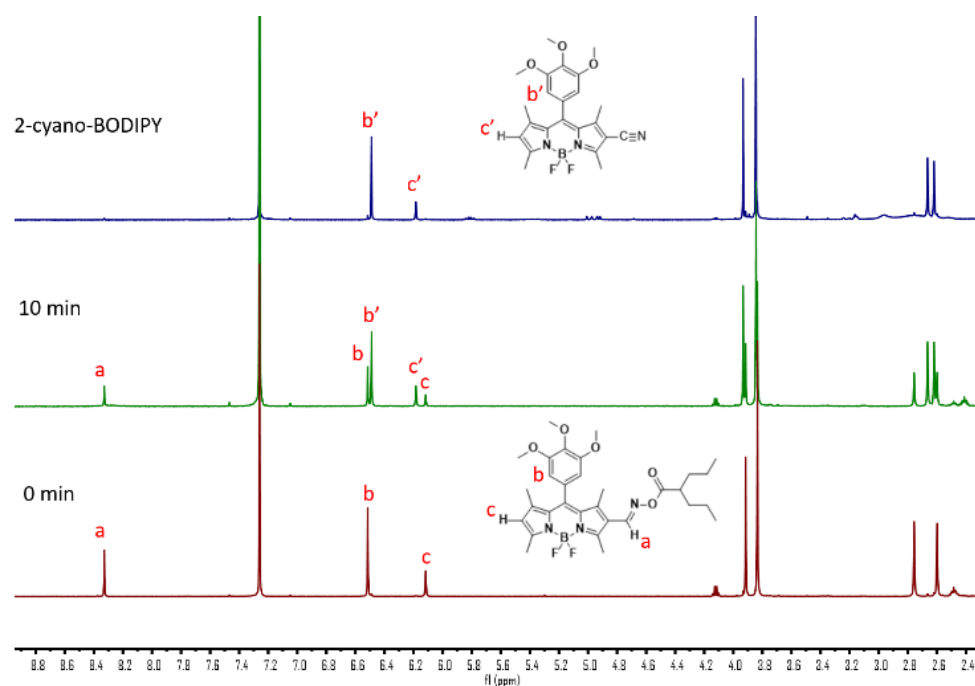


**Figure 4.6**  $^1\text{H}$  NMR spectra of **3a**, 2-cyano-BODIPY photo-byproduct and the photolysate mixture after 10 min irradiation with green LED ( $\lambda = 503 \pm 30$  nm,  $\sim 80$  mW/cm $^2$ ).

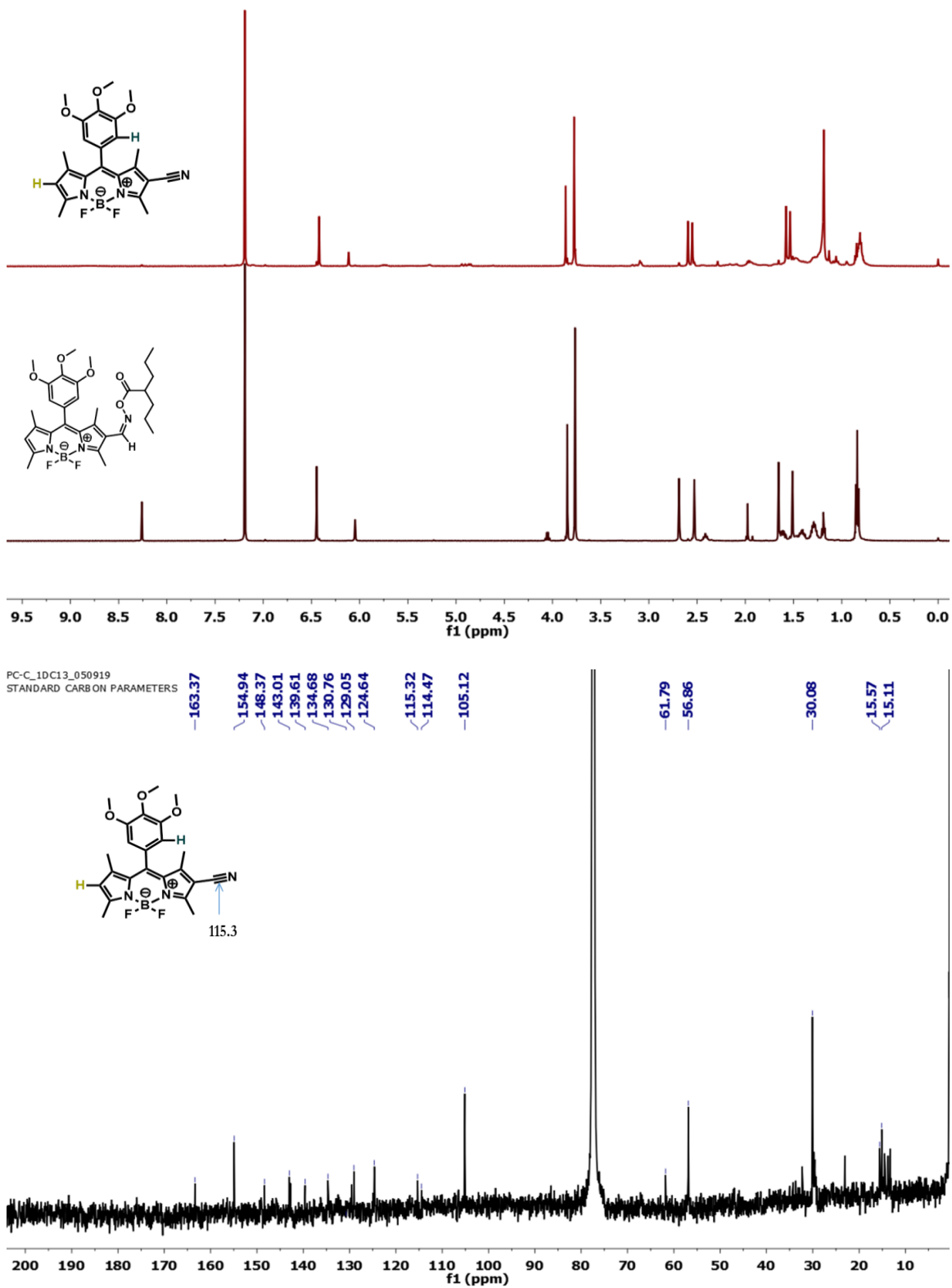
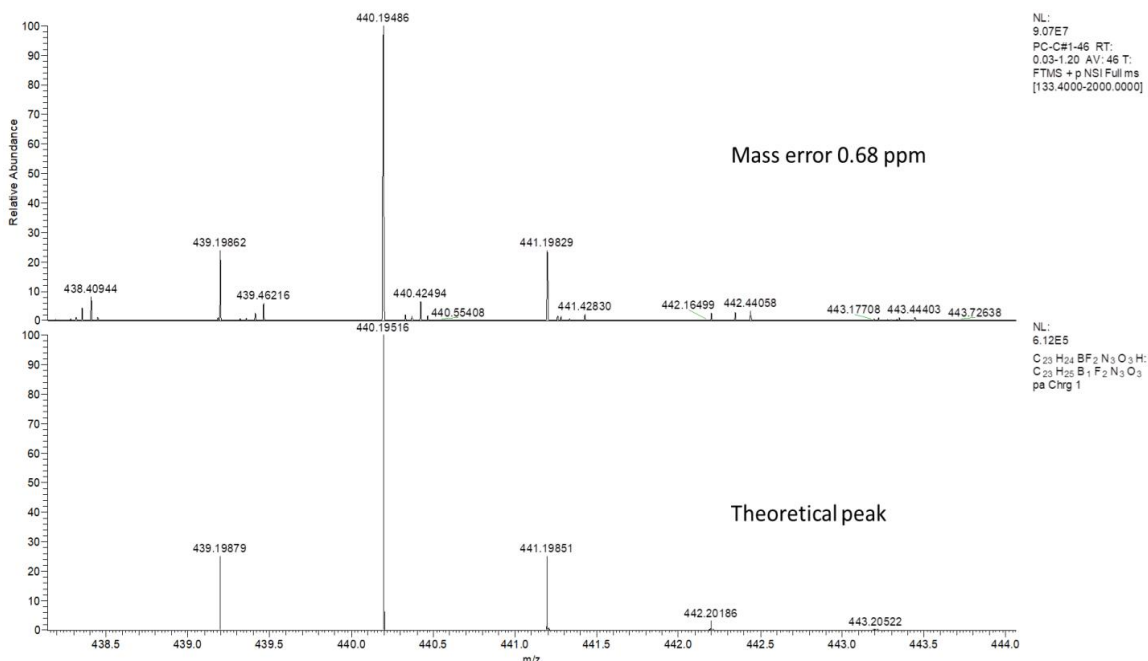


Figure 4.7  $^1\text{H}$ ,  $^{13}\text{C}$  NMR and Mass spectra of 2-cyano-BODIPY photo-byproduct.



**Figure 4.7(Continued)**  $^1\text{H}$ ,  $^{13}\text{C}$  NMR and Mass spectra of 2-cyano-BODIPY photoproduct.

### 4.2.3 Photolysis Analysis

To understand whether the photo-uncaging proceeds through a triplet or singlet excited state, the Stern–Volmer quenching experiment on the BODIPY oxime ester **3a** was performed by using triplet quencher (TQ) potassium sorbate. Photolysis of  $1 \times 10^{-5}$  M solution of **3a** was irradiated without or with addition of different concentration of a triplet quencher (1 and 5 mM). The course of photolysis was monitored by UV-Vis absorbance spectroscopy and the change in absorbance was plotted against irradiation time (Figure 4.8). The result showed the rate of photo-uncaging decreased on increasing amount of TQ, indicating photo-uncaging of oxime ester proceeds partially via the triplet excited state. Based on the photo-uncaging byproduct and Stern–Volmer quenching experiment, we suggested a possible mechanism for the photolysis of BODIPY oxime ester platform by using the structure of **3a** as an example. As shown in Figure 4.9,

irradiation of **3a** leads to an excited state (both singlet and triplet), which then undergoes cleavage of the N–O linkage in BODIPY oxime ester and consequently release the caged molecule VPA and form the photoproduct of 2-cyano-BODIPY derivative.

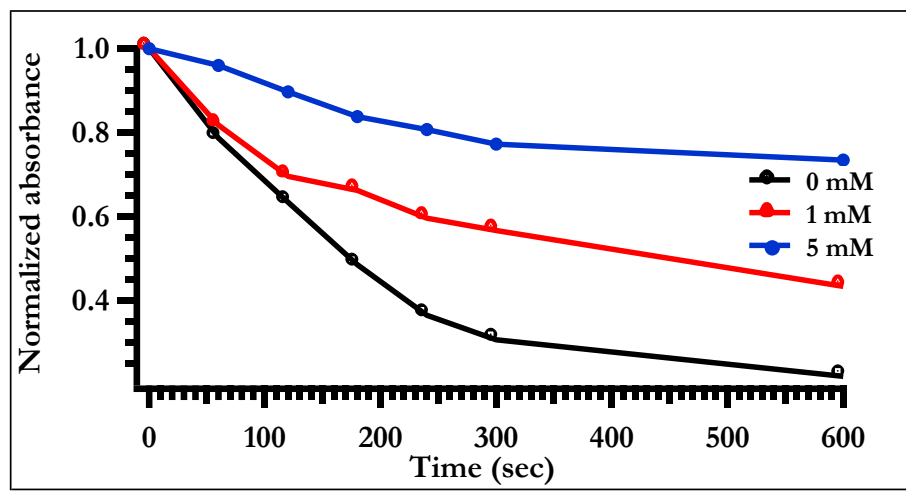


**Figure 4.8** Time course of photolysis for the oxime ester **3a** in presence of different amount of triplet quencher potassium sorbate (PS).

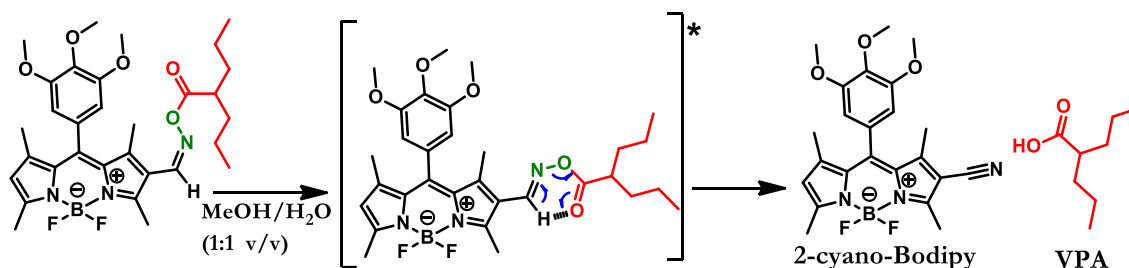


**Figure 4.9** Possible photo-uncaging mechanism of N-O bond cleavage of **3a** and the formation of 2-cyano-BODIPY as a photo-byproduct.

#### 4.2.4 Cellular Uptake and Cell Imaging

After investigating the mechanism and kinetics of this photo-uncaging platform, we went on to assess the biological application of light-regulated drug release. Starting from the cellular uptake, 10  $\mu\text{M}$  of **3a** was incubated with HeLa cells for 4 h, as shown in Figure 4.10a, fluorescence signals (Ex: 482/40; DM: 506; Em: 534/40) of **3a** were observed in the cytoplasm, which accumulated close to the nucleus. Furthermore, we tested the cell

uptake of **3a** at a lower concentration (1  $\mu\text{M}$ ) and shorter incubation time (1 h) (Figure 4.10b). The cell images showed similar uptake and location, indicating a high cellular uptake efficiency of **3a**, even at low concentration and short incubation duration.

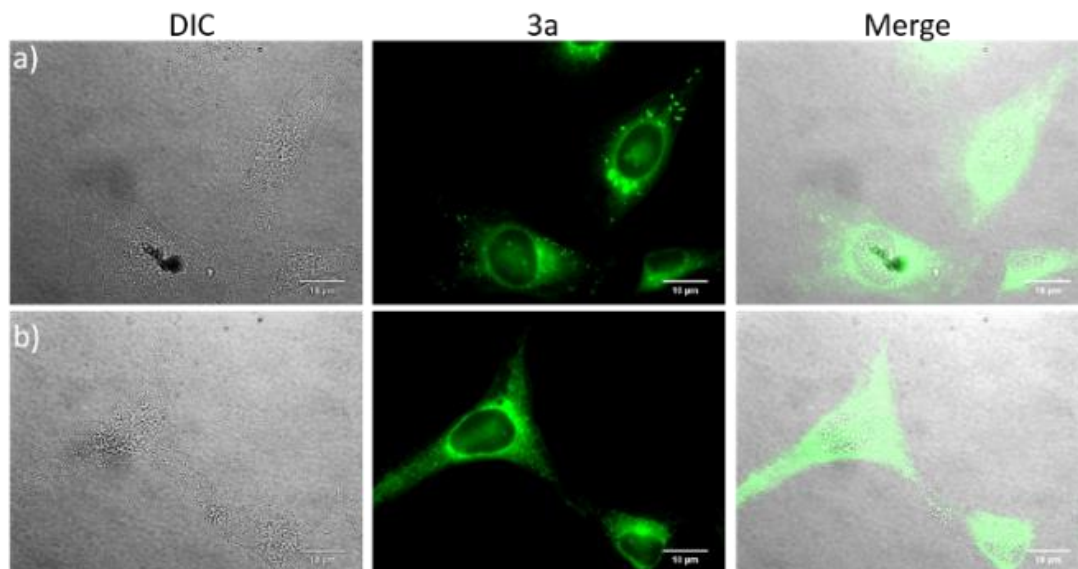


**Figure 4.10** a) HeLa cells were incubated with 10  $\mu\text{M}$  of **3a** for 4 h, b) HeLa cells were incubated with 1  $\mu\text{M}$  of **3a** for 1 h. DIC is the bright field.

#### 4.2.5 Dark Cell Viability and Photo-toxicity

The dark cytotoxicity of **3a** was evaluated in HeLa cells via MTS assay, shown in figure 4.11a. Two groups were performed in HeLa cells in the dark that incubated with **3a** with or without removing extracellular **3a** (washing) at the time point of 4 h. Both of conditions did not show any acute toxic effects over a range of concentrations, even at the highest concentration employed of 40  $\mu\text{M}$ , cell viability remained over 90%.

The phototherapeutic efficiency was then measured by testing the irradiation time dependent cell viability. HeLa cells were incubated with 20  $\mu\text{M}$  of **3a** in two groups, with or without washing at the time point of 4 h. After further incubation of 24 h, LED light was given with varied irradiation time. As show in Figure 4.11b, cell viabilities of both

groups were decreased with increased irradiation time, where they showed cell viability less than 40% after 5 min irradiation, and less than 20% after 10 min. Meanwhile, untreated control group (with LED light in absence of **3a**) exhibits no cytotoxicity even over 20 min irradiation, the cell viability was remained 100%, which indicates the LED light exposure itself has negligible damage to the cells. Furthermore, the photo-byproduct 2-cyano-BODIPY of **3a** exhibits relatively non-toxic to the cell (Figure 4.12), which indicates that the therapeutic and toxic effects came from the released VPA. In literature, VPA inhibits HDAC in vitro in a dose-dependent manner with an IC<sub>50</sub> between 0.93 to 2.43 mM when used along for the treatment ovarian cancer.<sup>161, 162</sup> And the IC<sub>50</sub> of VPA for HeLa cells are reported to be around 2 mM.<sup>163</sup> Clearly, our strategy of photo-uncaging exhibits more therapeutic efficiency with lower concentration (20 μM), that is 100 times lower than IC<sub>50</sub> of VPA in HeLa cells. The high therapeutic efficiency of **3a** can be explained by the good cellular uptake ability and the intracellular location around the nucleus, where HDAC presents the most. Furthermore, the two groups under irradiation (Figure 4.11b) with or without washing at the time point of 4 h showed no significantly difference of the cytotoxicity, indicates the major toxic (therapeutic effect) came from the VPA released inside cytoplasm. Upon irradiation the extracellularly released VPA exhibited none significant toxicity to cells.

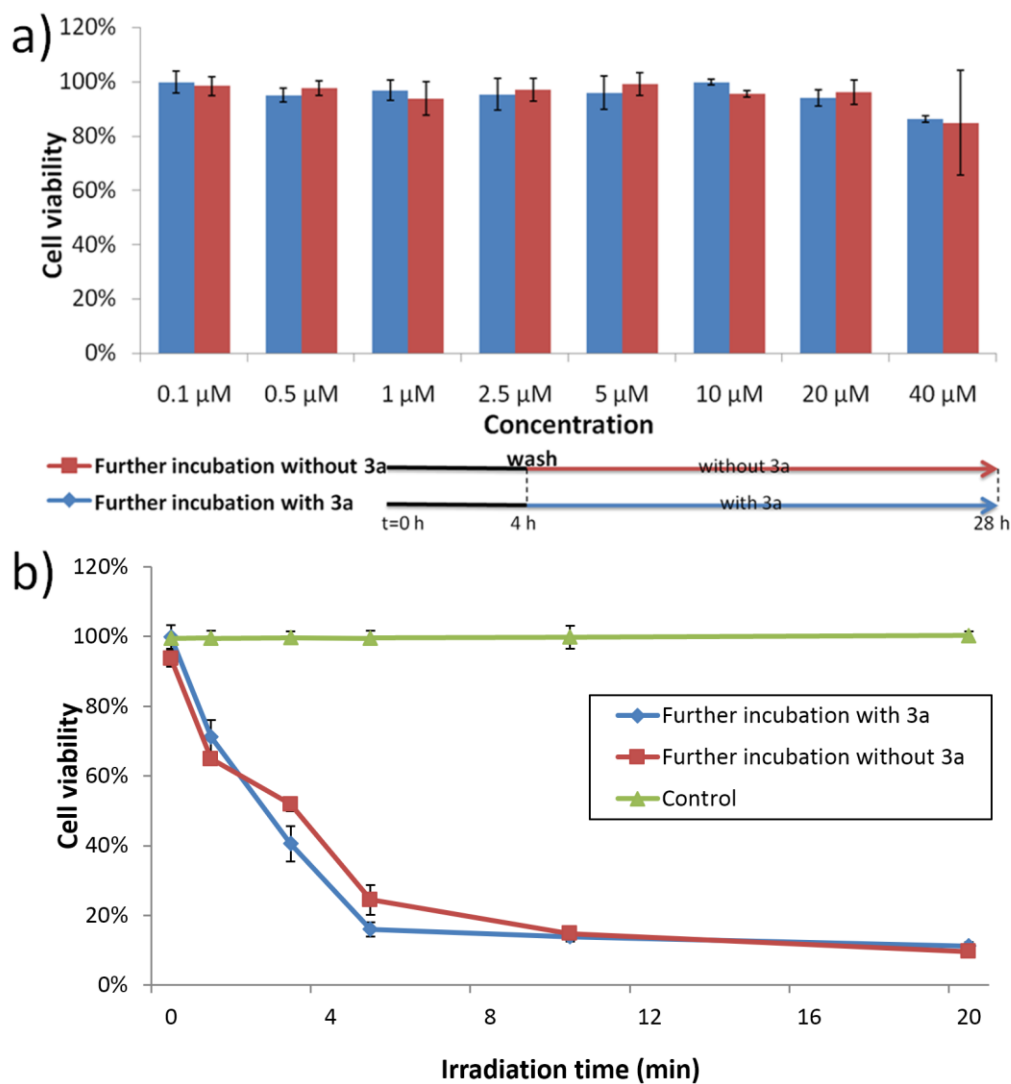


**Figure 4.11** Dark and photo-toxicity of **3a**. a) dark cell viability of HeLa after treatment with **3a** in different concentrations, with (red bar) or without (blue bar) removal of extracellular **3a** at 4 h. b) LED (503±30 nm, ~80 mW/cm<sup>2</sup>) light irradiation time dependent cell viability of HeLa cells after treatment with 20 μM of **3a** with (red line) and without (blue line) removal of extracellular **3a** at 4 h. Control group (green line) is HeLa cells treated with LED light in the absence of **3a**. (HeLa cells without light and **3a** classified as 100%)

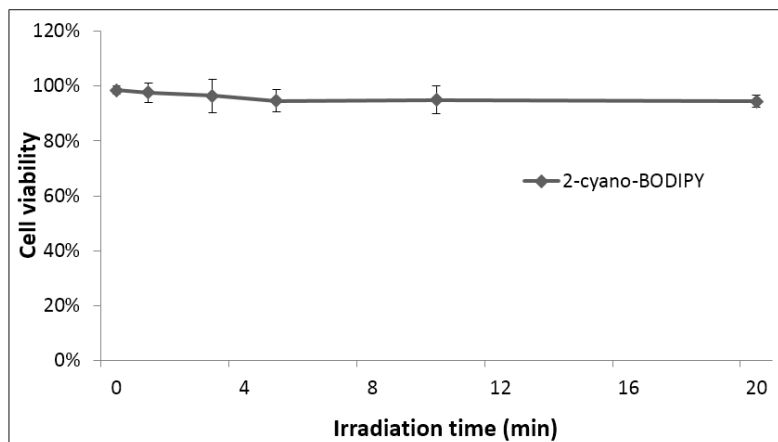


**Figure 4.12** Photo-toxicity of 2-cyano-BODIPY. LED (503±30 nm, ~80 mW/cm<sup>2</sup>) light irradiation time dependent cell viability of HeLa cells after treatment with 20 μM of 2-cyano-BODIPY. HeLa cells with no treatment was classified as 100%. (N=6)

## 4.3 Methods

### 4.3.1 Materials

All reagents and solvents were purchased from commercial suppliers and used as received without further purification. Compound **2** was synthesized according to their previous reported procedures. <sup>1</sup>H and <sup>13</sup>C NMR spectra were carried out in CDCl<sub>3</sub> solution on a Bruker AVANCE spectrometer (500 MHz). orbitrap mass spectrometry analyses were performed in Prof. Hao Chen's lab, Department of Chemistry and Environmental Science, New Jersey Institute of Technology (NJIT). Flash column chromatography was performed on a CombiFlash® Rf+ automated flash chromatography using RediSep Rf Gold® normal-phase HP silica columns. UV-vis absorption spectra were recorded on an Tecan Infinite M200 PRO plate reader spectrometer in 1 cm path length cuvettes. Fluorescence emission spectra were measured using an Edinburgh FLS980 fluorescence spectrometer. One-photon fluorescence microscopy images were

recorded on an Olympus IX-81 DSU microscope equipped with a Hamamatsu EMCCD C9100 digital camera.

#### 4.3.2 Synthesis of BODIPY Core

3,4,5-Trimethoxybenzaldehyde (1.65 g) and 2,4-dimethylpyrrole (1.6 g) were dissolved in dry  $\text{CH}_2\text{Cl}_2$  (800 mL) under a nitrogen atmosphere. Nine drops of trifluoroacetic acid (TFA) (about 0.5 mL) were added, and the mixture was stirred at room temperature overnight. After TLC monitoring showed complete disappearance of the aldehyde, a solution of 2, 3-dichloro-5, 6-dicyano-1, 4-benzoquinone (DDQ) (1.9 g) in anhydrous  $\text{CH}_2\text{Cl}_2$  (200 mL) was added. This mixture was further stirred for 4 h, and N, N-diisopropylethylamine (DIPEA) (16 mL) were added under a nitrogen atmosphere. The solution was stirred at room temperature for 30 min, and  $\text{BF}_3\text{-OEt}_2$  (20 mL) was subsequently added. This mixture was stirred for overnight, where upon the complexation was found to be completed by TLC monitoring. The mixture was washed thoroughly with water and brine, dried over anhydrous  $\text{Na}_2\text{SO}_4$ , filtered, and evaporated under vacuum. The crude compound was purified by silica gel column chromatography (eluent: petroleum ether/ethyl acetate: first 10:1 to final 5:1, increasing the polarity of the solvent) to give a shiny green powder as the pure BODIPY dye (600 mg).  $^1\text{H}$  NMR (500 MHz,  $\text{CDCl}_3$ ):  $\delta$  : 6.53 (s, 2H); 6.00(s, 2H), 3.92 (s, 3H,  $\text{OCH}_3$ -4), 3.83 (s, 6H,  $2 \times \text{OCH}_3$ -3, 5), 2.56 (s, 6H), 1.53 (s, 6H) ppm.  $^{13}\text{C}$  NMR (126 MHz,  $\text{CDCl}_3$ )  $\delta$ : 155.6, 154.2, 143.0, 141.3, 138.6, 131.3, 130.1, 121.2, 105.1, 61.3, 56.3, 30.9, 14.2 ppm.

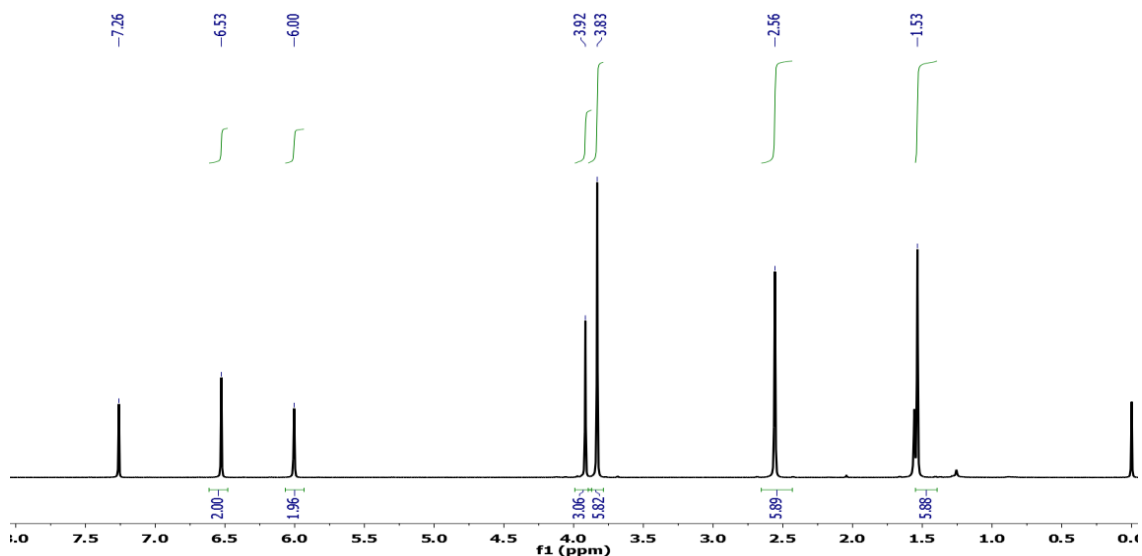


**Figure 4.13**  $^1\text{H}$  NMR of BODIPY core compound.

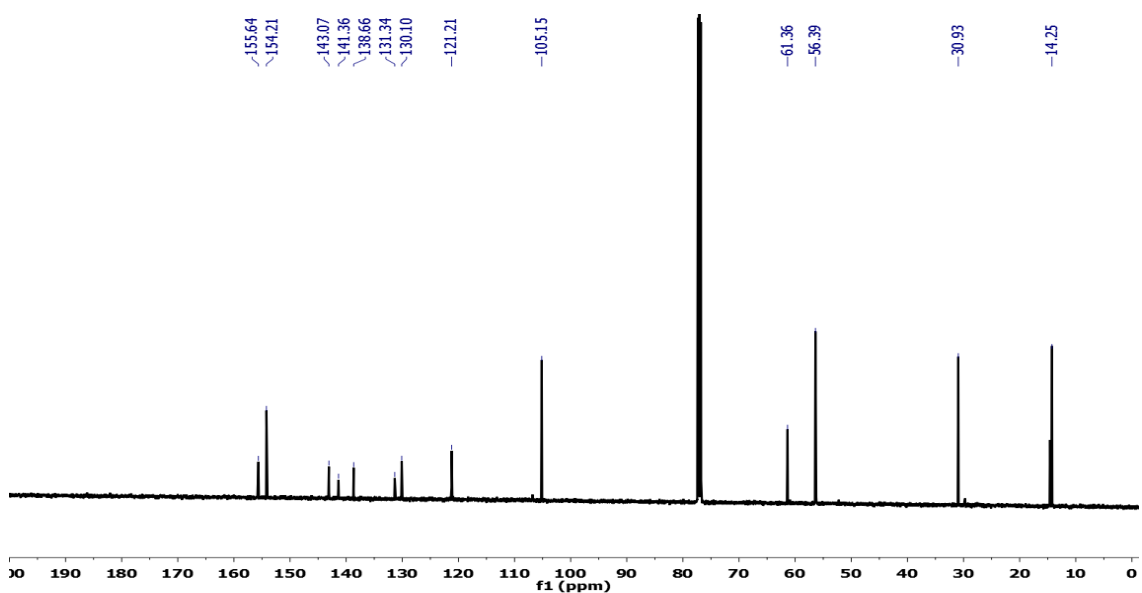


**Figure 4.14**  $^{13}\text{C}$  NMR of BODIPY core compound.

### 4.3.3 Synthesis of BODIPY Aldehyde (1)

A mixture of DMF (6 mL) and  $\text{POCl}_3$  (6 mL) was stirred at  $-5\text{ }^\circ\text{C}$  for 30 min, to this reaction mixture BODIPY core (150 mg) was dissolved in dichloromethane (5 mL), and the mixture was stirred for 2 h. The crude product was purified using column chromatography (silica gel, hexane/EtOAc 6/4 v/v) to give BODIPY aldehyde (1) (142

mg, 89%) as red crystal solid.  $^1\text{H}$  NMR (500 MHz,  $\text{CDCl}_3$ ):  $\delta$ : 10.0 (s, 1H), 6.51 (s, 2H), 6.18 (s, 1H), 3.93 (s, 3H,  $\text{OCH}_3$ -4), 3.84 (s, 6H,  $2 \times \text{OCH}_3$ -3, 5), 2.82 (s, 3H), 2.62 (s, 3H), 1.81 (s, 3H), 1.60 (s, 3H).  $^{13}\text{C}$  NMR (126 MHz,  $\text{CDCl}_3$ )  $\delta$ : 206.9, 185.8, 161.7, 156.6, 154.5, 147.2, 143.2, 142.8, 139.1, 134.0, 129.1, 123.9, 104.9, 61.4, 56.4, 30.9, 14.7, 11.5 ppm. HRMS-ESI:  $\text{C}_{23}\text{H}_{25}\text{BF}_2\text{N}_2\text{O}_4$ , Calculated :443.19482, Found:  $[\text{M}+\text{H}]^+$ :443.19475.

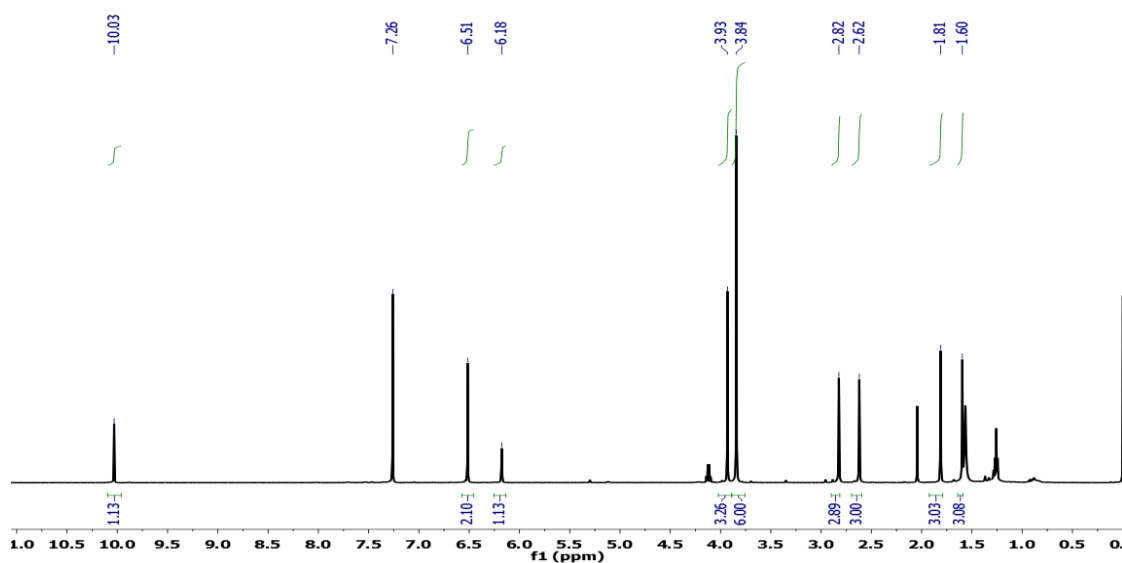


**Figure 4.15**  $^1\text{H}$  NMR of aldehyde BODIPY compound **1**.

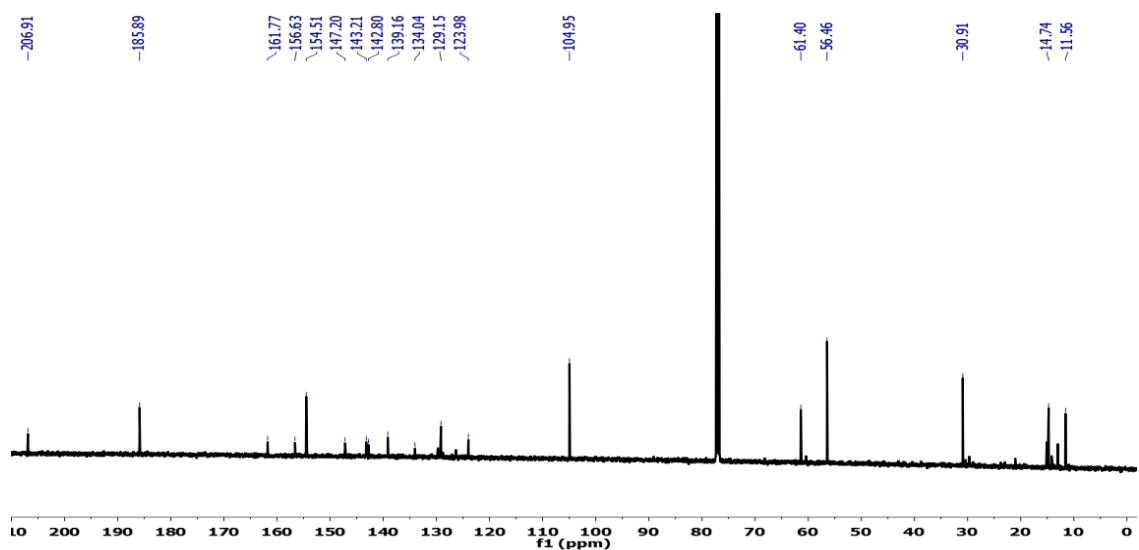


**Figure 4.16**  $^{13}\text{C}$  NMR of aldehyde BODIPY compound **1**.

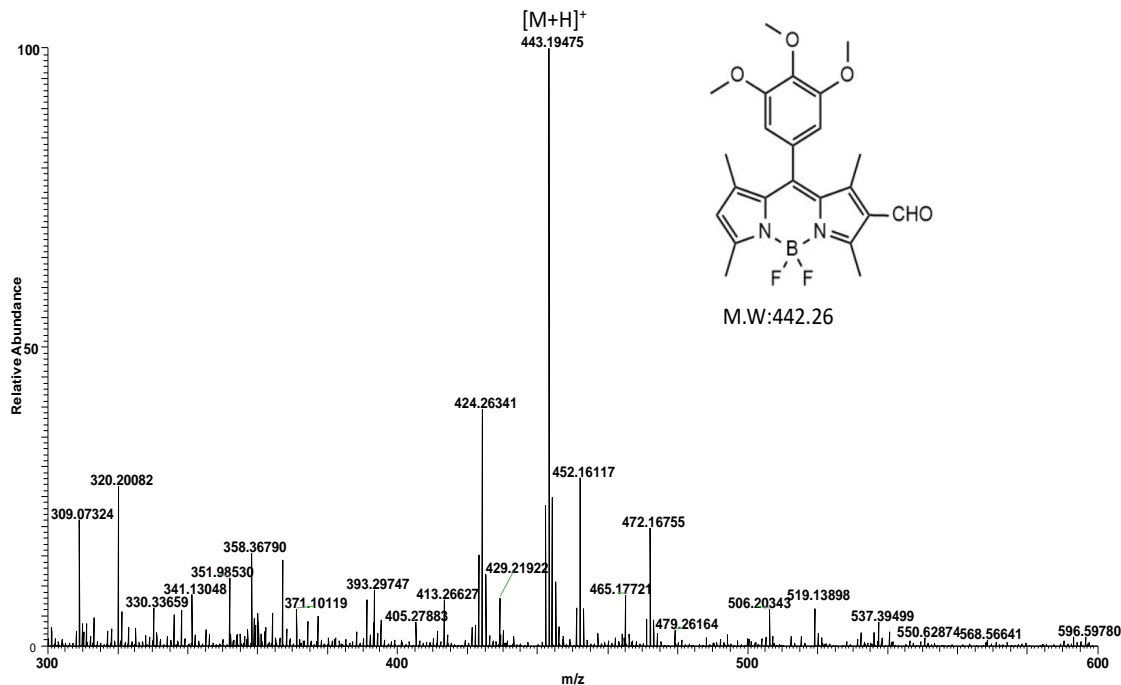


**Figure 4.17** MS spectrum of aldehyde BODIPY compound 1.

#### 4.3.4 Synthesis of BODIPY-oxime Parent Compound (2)

Compound 1 (100 mg) and hydroxylamine hydrochloride (41.4 mg) in absolute ethanol (20.0 mL) were stirred at reflux temperature for 1 h, the residue was purified by column chromatography (hexane/ethyl acetate (7/3)). BODIPY-oxime parent compound 2 was obtained as red solid (86.0 mg, 70.0% yield).  $^1\text{H}$  NMR (500 MHz,  $\text{CDCl}_3$ )  $\delta$ : 8.01 (s, 1H), 6.52 (s, 2H), 6.08 (s, 1H), 3.93 (s, 3H,  $\text{OCH}_3$ -4), 3.83 (s, 6H,  $2 \times \text{OCH}_3$ -3, 5), 2.70 (s, 3H), 2.58 (s, 3H), 1.62 (s, 3H), 1.55 (s, 3H).  $^{13}\text{C}$  NMR (126 MHz,  $\text{CDCl}_3$ )  $\delta$ = 158.2, 154.3, 144.8, 142.0, 139.9, 138.9, 130.4, 129.7, 122.4, 121.48, 105.1, 61.4, 56.4, 14.5, 12.3 ppm.

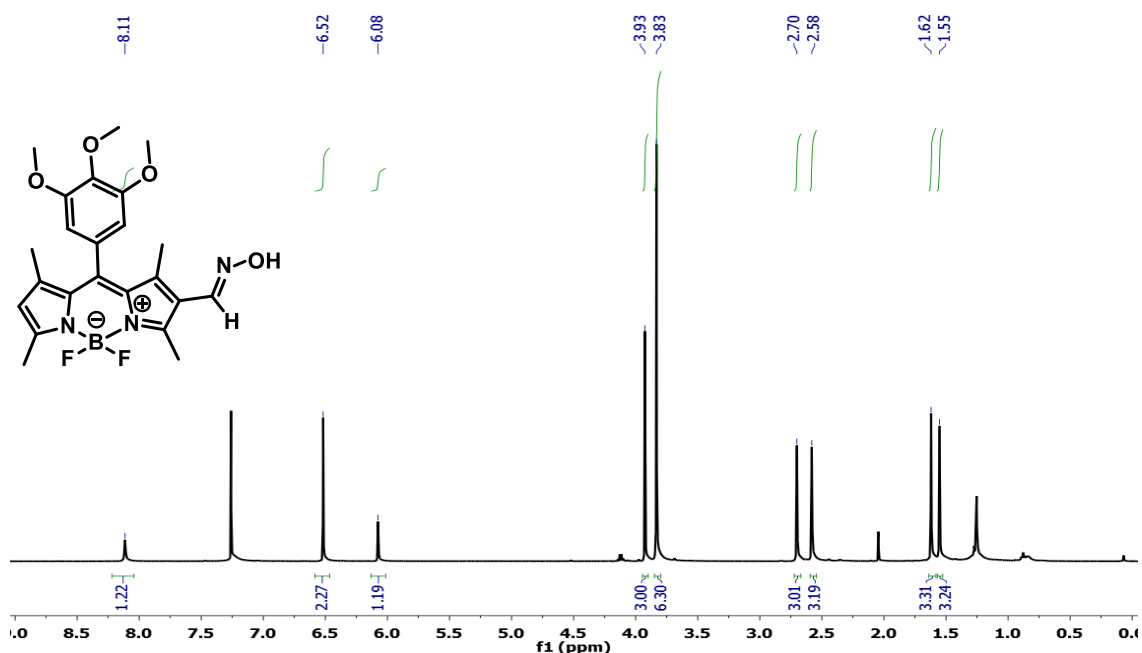


Figure 4.18  $^1\text{H}$  NMR of BODIPY compound 2.

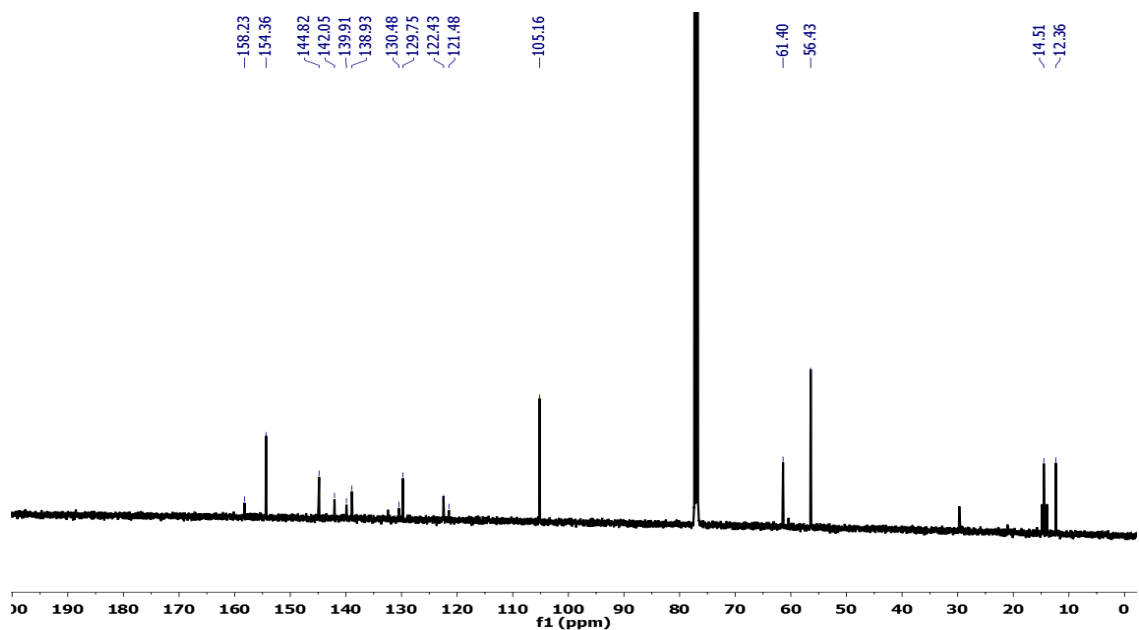


Figure 4.19  $^{13}\text{C}$  NMR of BODIPY compound 2.

#### 4.3.5 Synthesis of BODIPY Oxime Esters (3a, 3b)

A solution of BODIPY oxime (2) in dry dichloromethane was cooled to 0 °C under a nitrogen atmosphere, triethylamine (0.28 ml) was added followed by acid chloride (1.2eq) in dry dichloromethane and the mixture was allowed to stir for 4 h allowing the

temp to slowly rise to 25 °C. The organic phases were then washed with brine and the residue was purified by column chromatography (hexane/ethyl acetate 7/3 v/v). BODIPY oxime ester was obtained as red solid in good yield.

**(3a):**  $^1\text{H}$  NMR (500 MHz,  $\text{CDCl}_3$ )  $\delta$ : 8.32 (s, 1H), 6.51 (s, 2H), 6.11 (s, 1H), 3.91 (s, 3H,  $\text{OCH}_3$ -4), 3.83 (s, 6H,  $2 \times \text{OCH}_3$ -3, 5), 2.75 (s, 3H), 2.59 (s, 3H), 2.51-2.46 (m, 1H), 1.72 (s, 3H), 1.69-1.64 (m, 2H), 1.58 (s, 3H), 1.51-1.48 (m, 2H), 1.47-1.36 (m, 2H), 1.25-0.89(t, 6H).  $^{13}\text{C}$  NMR (126 MHz,  $\text{CDCl}_3$ )  $\delta$ : 180.6, 173.8, 159.7, 154.4, 150.0, 146.0, 142.4, 140.9, 139.0, 133.0, 130.5, 129.4, 123.1, 119.5, 105.0, 61.4, 60.3, 56.4, 43.9, 34.6, 20.6, 14.6, 13.9 ppm.  $\text{C}_{31}\text{H}_{40}\text{BF}_2\text{N}_3\text{O}_5$   $\text{H}^+$  Calculated Mass: 584.3007, Experimental mass:  $[\text{M}+\text{H}]^+$ : 584.3095.

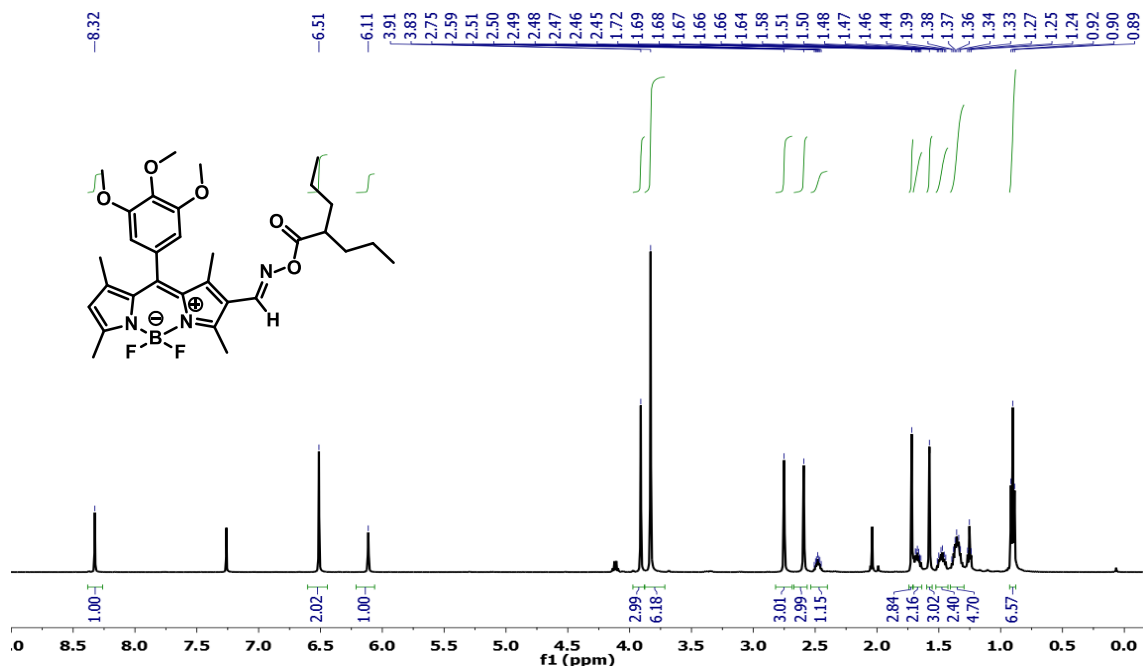


**Figure 4.20**  $^1\text{H}$  NMR of BODIPY compound **3a**.

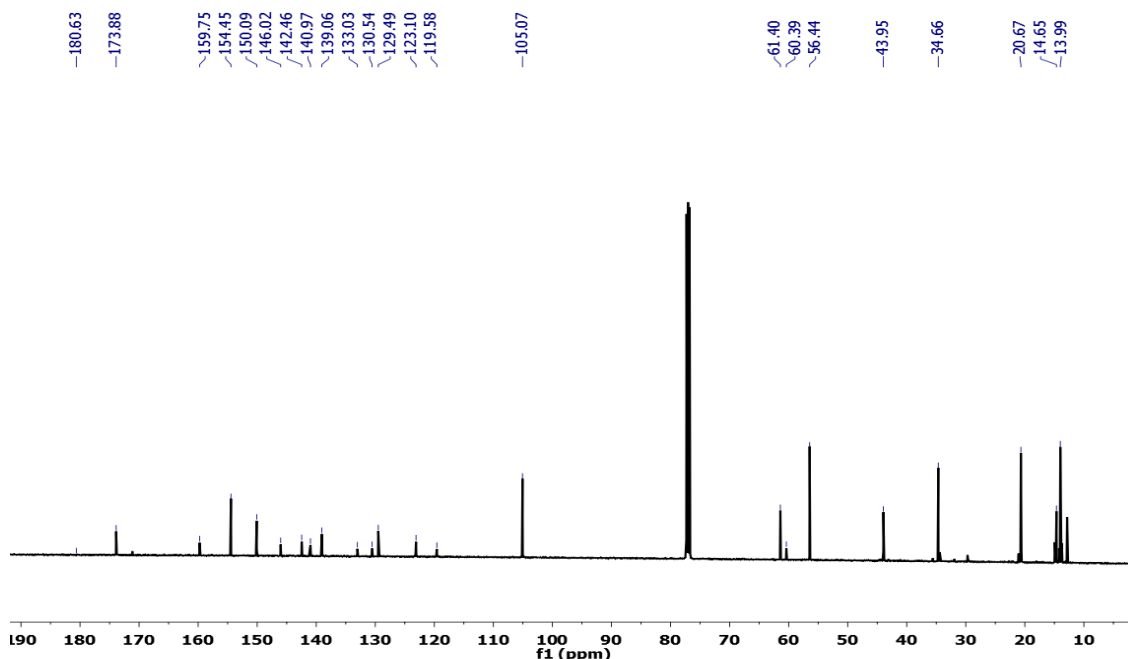


**Figure 4.21**  $^{13}\text{C}$  NMR of BODIPY compound **3a**.

karthik\_1 #90-159 RT: 2.36-4.16 AV: 70 NL: 9.49E7  
T: FTMS + p NSI Full.ms [100.0000-1500.0000]  
129.05225

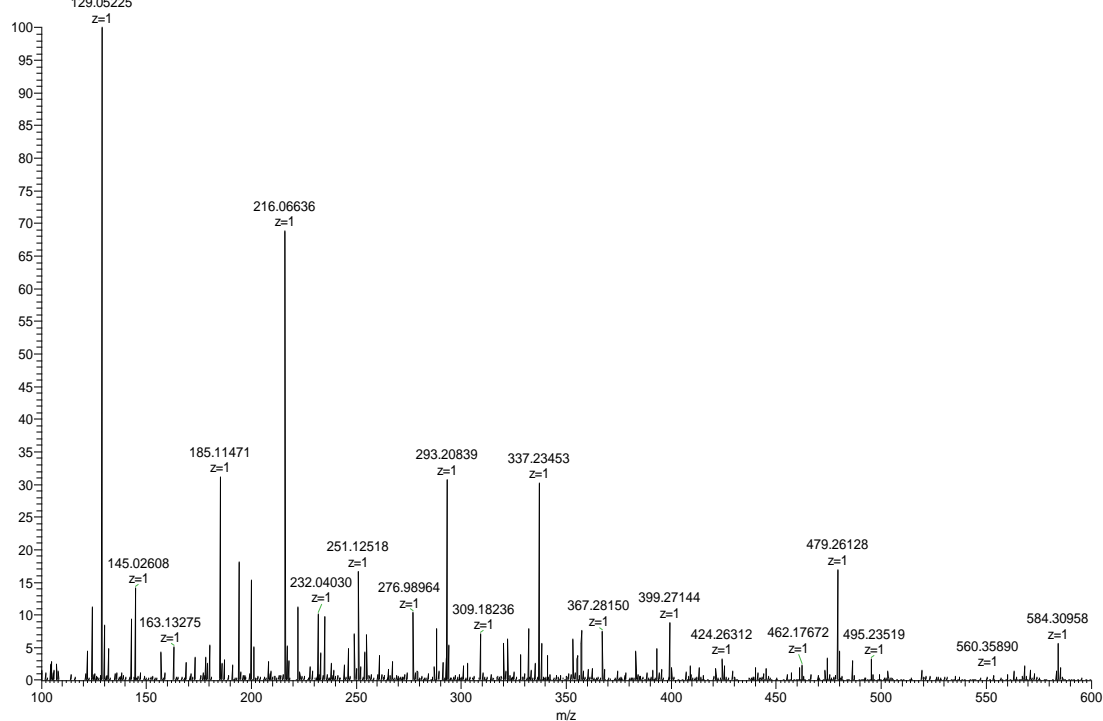


**Figure 4.22** MS spectrum of BODIPY compound **3a**.

**(3b):**  $^1\text{H}$  NMR (500 MHz,  $\text{CDCl}_3$ )  $\delta$ : 8.09 (d, 2H), 6.98 (d, 2H), 6.51 (s, 2H), 6.21 (s, 1H), 3.95 (s, 3H,  $\text{OCH}_3$ ), 3.90 (s, 3H,  $\text{OCH}_3$ -4), 3.87 (s, 6H,  $2 \times \text{OCH}_3$ -3, 5), 2.69 (s,

6H), 1.67 (s, 6H).  $^{13}\text{C}$  NMR (126 MHz,  $\text{CDCl}_3$ )  $\delta$ : 164.6, 162.3, 160.0, 154.4, 148.7, 145.9, 142.0, 139.0, 137.2, 134.4, 132.8, 129.2, 127.8, 122.7, 122.3, 114.1, 104.9, 61.4, 56.4, 55.6, 29.7, 14.5, 11.4 ppm.  $\text{C}_{31}\text{H}_{32}\text{BF}_2\text{N}_3\text{O}_6$   $\text{H}^+$  Calculated Mass: 592.2430, Experimental mass:  $[\text{M}-\text{F}^-]^+$ : 572.92718.

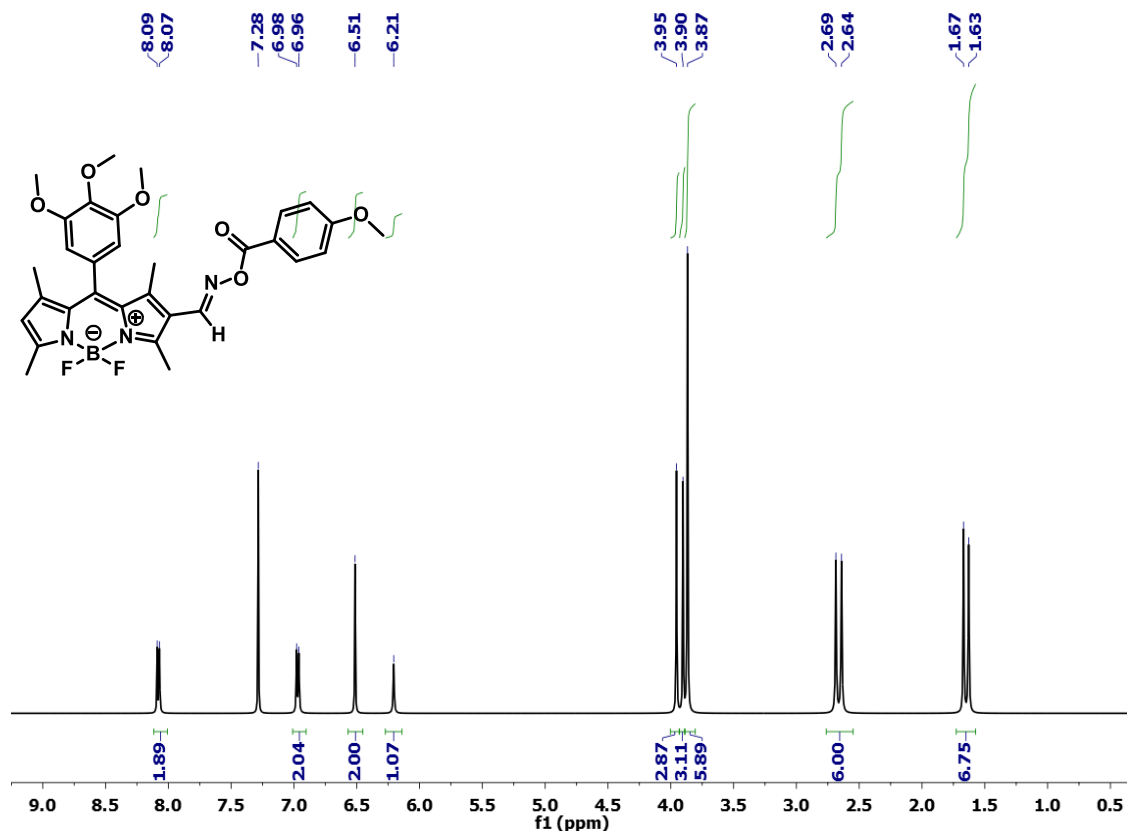


**Figure 4.23**  $^1\text{H}$  NMR of BODIPY compound **3b**.

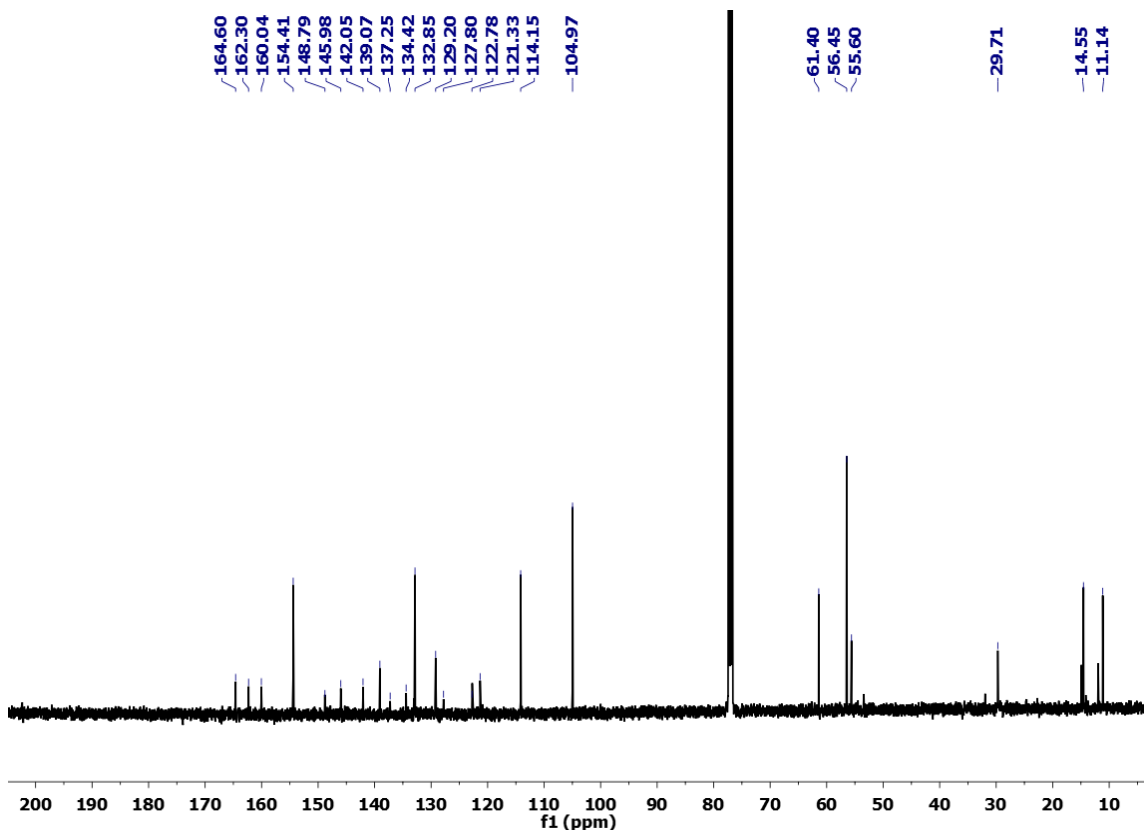


**Figure 4.24**  $^{13}\text{C}$  NMR of BODIPY compound **3b**.

#### 4.3.6 Photophysical Property Measurement

All steady-state absorption, fluorescence emission, of compound **3a** and **3b** were investigated in 10 mm path length quartz cuvettes at room temperature. The steady-state absorption was measured with Tecan Infinite M200 PRO plate reader spectrometer in 1 cm path length cuvettes. Fluorescence emission and excitation spectra were obtained using an Edinburgh Photonics FLS980 spectrometer equipped with a thermoelectric cooled photo multiplier detector (Hamamatsu) and a liquid-nitrogen cooled NIR-photomultiplier detector (Hamamatsu). All measurements were carried out with the optical density below 0.12 at the excitation wavelength to avoid reabsorption. The excitation and fluorescence emission spectra were corrected for the spectral sensitivity of

Edinburgh Photonics excitation and detection system using factory-measured correction files. Fluorescence lifetimes ( $\tau_F$ ) were determined with the single photon counting technique (TCSPC) and the same fluorescence spectrometer using a pulsed picosecond diode laser (EPL-505) as the excitation source. Molar absorption coefficients ( $\epsilon$ ) and maximum absorbance wavelengths ( $\lambda_{\max}$ ) were determined in acetonitrile using Beer's law, from plots of absorbance vs. concentration. Recordings were performed in 10 mm path length quartz cuvettes at room temperature.

Fluorescence quantum yields were determined by a reference point method. Fluorescein as standard / exc at 496nm in 0.1 M NaOH ( $\phi_f$ ) = 0.95 was used as a standard sample to calculate the QY of **3a** and **3b**. The equation as follow:  
(4.1)

$$\frac{\phi_s}{\phi_R} = \frac{A_s}{A_R} \frac{(\text{Abs})_R}{(\text{Abs})_s} \frac{\eta_s^2}{\eta_R^2}$$

where  $\Phi$  represents quantum yield, Abs represents absorbance,  $A$  represents area under the fluorescence curve, and  $\eta$  is refractive index of the medium. The subscripts S and R denote the corresponding parameters for the sample and reference, respectively.

Compound **3a** (2 mL of  $1 \times 10^{-5}$  M in MeOH/Water (7/3 v/v) and Compound **3b** (2 mL of  $1 \times 10^{-5}$  M in MeOH/Water (7/3 v/v)) was placed in quartz cuvette (10 mm path). Further the photolysis was followed by biological condition also Compound **3a** (2 mL of  $1 \times 10^{-5}$  M in PBS/DMSO (9.5/0.5 v/v)) was placed in quartz cuvette (10 mm path). The cuvette was placed in front of a light source (Thorlab's M505L3) mounted LED has a nominal wavelength  $503 \pm 30$  nm with a power density of  $\approx 80$  mW/cm<sup>2</sup>, at 1 cm distance and irradiated for the indicated times. At regular interval of time point, the cuvette was

analysis by UV-Vis spectrophotometer. The photochemical stability was investigated quantitatively by measuring the photochemical decomposition quantum yield,  $\Phi_{\text{ph}} = N_{\text{ph}}/N_{\text{hv}}$  ( $N_{\text{ph}}$  and  $N_{\text{hv}}$  are the numbers of decomposed molecules and absorbed photons, respectively). The values of  $\Phi_{\text{ph}}$  were determined by an absorption method using a mounted LED for excitation of the compound **3a** and **3b** (excitation wavelength  $\approx 503$  nm, average beam irradiance  $\approx 80$  mW/cm<sup>2</sup>). According to the well-developed absorption methodology, the values of  $\Phi_{\text{ph}}$  can be determined by the following equation:

$$\Phi_{\text{ph}} = (A_t - A_0)N_A/10^3 \times \epsilon \times I \times [1 - 10^{-(A_t + A_0)/2}] \times t \quad (4.2)$$

$A_t$  and  $A_0$  are absorbance maximum at time points  $t$  and  $t_0$ , respectively.  $N_A$  is Avogadro's number,  $\epsilon$  is the molar extinction coefficient (M<sup>-1</sup> cm<sup>-1</sup>),  $I$  is the irradiation intensity (photon cm<sup>-2</sup> s<sup>-1</sup>), and  $t$  is the irradiation time (sec).

5 mL of Compound **3a** ( $1 \times 10^{-5}$  M) in MeOH/Water (7/3 v/v) solution was placed in quartz cuvette (10 mm path). They were irradiated under mounted LED has a wavelength of  $503 \pm 30$  nm with the output power of  $\approx 80$  mW/cm<sup>2</sup>. At regular interval of time, 50  $\mu$ L of the aliquots was taken and analyzed by LC-MS using mobile phase acetonitrile/water (95/5 v/v), at a flow rate of 0.1 mL/min (detection: UV at wavelength of 500 nm). The reaction was followed until the consumption of the caged oxime ester of the initial area. The peak areas were determined by LC, which indicated gradual increase of peak area with time.

We also have followed the course of the photorelease by <sup>1</sup>H NMR spectroscopy. A known amount (1 mL) of aqueous suspension of the photolysate was taken at regular intervals of time and was extracted in dichloromethane (DCM), then solvent was

evaporated under vacuum and re-dissolved in  $\text{CDCl}_3$  and the  $^1\text{H}$  NMR was recorded.  $^1\text{H}$  NMR spectra showed a clean photocleavage of the **3a** into corresponding photoproducts.

#### 4.3.7 Preparative Photolysis

5 mg of Compound **3a** in MeOH/Water (7/3 v/v) solution were irradiated under mounted LED has a wavelength of  $503 \pm 30$  for 10 min. At regular interval of time, the reaction was monitored by TLC. After completion of reaction the photoproduct was isolated using preparative TLC using 15% EtOAc as a mobile phase. The photoproduct of 2-cyano-BODIPY was analyzed by  $^1\text{H}$ ,  $^{13}\text{C}$  NMR and mass analysis.  $^1\text{H}$  NMR (500 MHz,  $\text{CDCl}_3$ )  $\delta$ : 6.49 (s, 2H), 6.18 (s, 1H), 3.93 (s, 3H, OCH<sub>3</sub>-4), 3.87 (s, 6H, 2  $\times$  OCH<sub>3</sub>-3, 5), 2.66-2.62(s, 6H), 1.65-1.61 (s, 6H).  $^{13}\text{C}$  NMR (126 MHz,  $\text{CDCl}_3$ )  $\delta$ : 163.37, 154.94, 148.37, 143.01, 139.61, 134.68, 130.76, 129.05, 124.64, 115.32, 114.47, 105.12, 61.79, 56.86, 30.08, 15.57, 15.11.  $\text{C}_{23}\text{H}_{24}\text{BF}_2\text{N}_3\text{O}_3\text{H}^+$  Calculated Mass: 440.1951, Experimental mass: 440.1948.

#### 4.3.8 Cell Culture and Cellular Uptake

HeLa cell line was cultured in Dulbecco's Modified Eagle Medium (DMEM) supplemented with 10% fetal bovine serum, 1% penicillin/streptomycin at 37 °C in a humidified 5%  $\text{CO}_2$  incubator. To investigate the cellular of BDVPA, HeLa cells were employed. All cells were seeded on confocal dish (MatTek) at the density of  $4 \times 10^4$  cells per dish and incubated for 24 h at 37 °C. Stock solutions of **3a** dissolved in DMSO were prepared at a nominal concentration of  $10^4$   $\mu\text{M}$ . The stock solution was diluted to 1 and 10  $\mu\text{M}$  with the DMEM cell medium respectively and freshly placed over cells for 1 h and 4 h incubation period separately. Cells were washed three times with PBS and the live cell imaging solution (Molecular Probes) was added to confocal dishes. Fluorescent

images were obtained using an inverted Olympus IX70 microscope coupled with a FITC filter cube (Ex: 482/40; DM: 506; Em: 534/40). Bright field was obtained and **3a** fluorescent images were obtained and issued by Fiji, freely available image processing software.

#### 4.3.9 Cell Viability and Photolysis Cytotoxicity

To assess the cytotoxicity of **3a**, HeLa cells were cultured in the Dulbecco's modified Eagle's medium (DMEM) cell medium supplemented with 10% fetal bovine serum, 1% penicillin, and streptomycin at 37 °C and 5% CO<sub>2</sub>. Cells were placed in 96 well plates and incubated until there were no fewer than 5 × 10<sup>3</sup> cells per well for the experiments. Next, cells were incubated with different concentrations of **3a** (0.1, 0.5, 1, 2.5, 5, 10, 20, 40 μM) 4 h, where the values within parentheses refer to the nominal concentrations of the surfactants. Then, **3a** was removed and regular DMEM was added for 4 h washed + 24 h group, additional 22 h incubation was performed for both 4 h washed + 24 h and 4 h +24 h groups. After 22 h incubation, 20 μL of the Cell Titer 96 Aqueous One solution reagent (for MTS assay) was added into each well, followed by further incubation for 2 h at 37 °C. The respective absorbance values were read on a Tecan Infinite M200 PRO plate reader spectrometer at 490 nm. Cell viabilities were calculated based on the following equation:

$$Cell\ Viability\ (\%) = \frac{Abs_{490nm}^S - Abs_{490nm}^D}{Abs_{490nm}^C - Abs_{490nm}^{D2}} \times 100\% \quad (4.3)$$

where  $Abs_{490nm}^S$  is the absorbance of the cells incubated with different concentrations of experimental solutions,  $Abs_{490nm}^D$  is the absorbance of cell-free well containing only dye

at the concentration studied,  $Abs^C_{490nm}$  is the absorbance of cells only incubated in medium, and  $Abs^{D2}_{490nm}$  is the absorbance of the cell-free well.

To assess the photolysis cytotoxicity of **3a** and the photo-byproduct 2-cyano-BODIPY, HeLa cells were cultured in the Dulbecco's modified Eagle's medium (DMEM) cell medium supplemented with 10% fetal bovine serum, 1% penicillin, and streptomycin at 37 °C and 5% CO<sub>2</sub>. Cells were placed in 96 well plates and incubated until there were no fewer than  $5 \times 10^3$  cells per well for the experiments. Next, cells were incubated with 20 μM of **3a** and 2-cyano-BODIPY separately for 4 h, except control group which had no treatment. Then, **3a** was removed and regular DMEM was added for further incubation without **3a** group. After that, control, 2-cyano-BODIPY, further incubation with **3a** group, and further incubation without **3a** group were placed under the 505 nm LED lamp for various irradiation time (1, 3, 5, 10, 20 min). And an additional 22 h incubation was performed after the irradiation. 20 μL of the Cell Titer 96 Aqueous One solution reagent (for MTS assay) was added into each well, followed by further incubation for 2 h at 37 °C. The respective absorbance values were read on a Tecan Infinite M200 PRO plate reader spectrometer at 490 nm. Cell viabilities were calculated on the basis of above equation.

#### 4.4 Conclusion

In conclusion, we have developed a new BODIPY oxime ester photo-uncaging platform for light guided delivery of compounds containing carboxylic acid. The photochemistry and photo-physics of the uncaging were studied, and a possible photo-uncaging mechanism was proposed by identifying the structure of photo-byproduct. We

demonstrated that we can photo-uncage an anti-cancer drug (VPA) and observed enhanced therapeutic effects due to the increased cell uptake and localized release.

## REFERENCES

1. Chan, D. C. Mitochondria: dynamic organelles in disease, aging, and development. *Cell* **2006**, *125*, 1241-52.
2. Logan, D. C. The mitochondrial compartment. *J. Exp. Bot.* **2007**, *58*, 1225-43.
3. Frey, T. G.; Renken, C.W.; Perkins, G.A. Insight into mitochondrial structure and function from electron tomography. *Biochim. Biophys. Acta.* **2002**, *1555*, 196-203.
4. Becker, T.; Gebert, M.; Pfanner, N.; van der Laan, M. Biogenesis of mitochondrial membrane proteins. *Curr. Opin. Cell. Biol.* **2009**, *21*, 484-93.
5. Kühlbrandt, W. Structure and function of mitochondrial membrane protein complexes. *BioMed. Central Biol.* **2015**, *13*, 89.
6. Baker, M. J.; Frazier, A.E.; Gulbis, J.M.; Ryan, M.T. Mitochondrial protein-import machinery: correlating structure with function. *Trends Cell Biol.* **2007**, *17*, 456-64.
7. Dudkina, N. V.; Heinemeyer, J.; Sunderhaus, S.; Boekema, E. J.; Braun, H. P. Respiratory chain supercomplexes in the plant mitochondrial membrane. *Trends Plant Sci.* **2006**, *11*, 232-40.
8. Bauer, M. F.; Hofmann, S.; Neupert, W.; Brunner, M. Protein translocation into mitochondria: the role of TIM complexes. *Trends Cell Biol.* **2000**, *10*, 25-31.
9. Müller, V.; Grüber, G. ATP synthases: structure, function and evolution of unique energy converters. *Cell Mol. Life Sci.* **2003**, *60*, 474-94.
10. Song, W.; Bossy, B.; Martin, O. J.; Hicks, A.; Lubitz, S.; Knott, A. B.; Bossy-Wetzell, E. Assessing mitochondrial morphology and dynamics using fluorescence wide-field microscopy and 3D image processing. *Methods* **2008**, *46*, 295-303.
11. Okamoto, K.; Shaw, J. M. Mitochondrial morphology and dynamics in yeast and multicellular eukaryotes. *Annu. Rev. Genet.* **2005**, *39*, 503-36.
12. Karbowski, M.; Youle, R. J. Dynamics of mitochondrial morphology in healthy cells and during apoptosis. *Cell Death Differ.* **2003**, *10*, 870-80.
13. Liesa, M.; Palacín, M.; Zorzano, A. Mitochondrial dynamics in mammalian health and disease. *Physiol. Rev.* **2009**, *89*, 799-845.
14. Meyer, J.N.; Leuthner, T. C.; Luz, A. L. Mitochondrial fusion, fission, and mitochondrial toxicity. *Toxicology* **2017**, *391*, 42-53.

15. Chan, D. C. Fusion and fission: interlinked processes critical for mitochondrial health. *Annu. Rev. Genet.* **2012**, *46*, 265-87.
16. Youle, R. J.; van der Bliek, A. M. Mitochondrial fission, fusion, and stress. *Science* **2012**, *337*, 1062-5.
17. Hoppins, S. The regulation of mitochondrial dynamics. *Curr. Opin. Cell Biol.* **2014**, *29*, 46-52.
18. Chang, C. R.; Blackstone, C. Dynamic regulation of mitochondrial fission through modification of the dynamin-related protein Drp1. *Ann. N. Y. Acad. Sci.* **2010**, *1201*, 34-9.
19. Mishra, P.; Chan, D. C. Mitochondrial dynamics and inheritance during cell division, development and disease. *Nat. Rev. Mol. Cell Biol.* **2014**, *15*, 634-46.
20. Nazaret, C.; Heiske, M.; Thurley, K.; Mazat, J. P. Mitochondrial energetic metabolism: a simplified model of TCA cycle with ATP production. *J. Theor. Biol.* **2009**, *258*, 455-64.
21. Bartlett, K.; Eaton, S. Mitochondrial beta-oxidation. *Eur. J. Biochem.* **2004**, *271*, 462-9.
22. Skulachev, V. P. Uncoupling: new approaches to an old problem of bioenergetics. *Biochim. Biophys. Acta.* **1998**, *1363*, 100-24.
23. Srere, P. A. Citric acid cycle redux. *Trends Biochem. Sci.* **1990**, *15*, 411-2.
24. Osellame, L. D.; Blacker, T. S.; Duchen, M. R. Cellular and molecular mechanisms of mitochondrial function. *Best Pract. Res. Clin. Endocrinol. Metab.* **2012**, *26*, 711-23.
25. Efremov, R. G.; Baradaran, R.; Sazanov, L. A. The architecture of respiratory complex I. *Nature* **2010**, *465*, 441-5.
26. Vaux, D. L. Cell death in development. *Cell* **1999**, *96*, 245-54.
27. Li, Y. Z.; Li, C. J.; Pinto, A. V.; Pardee, A. B. Release of mitochondrial cytochrome C in both apoptosis and necrosis induced by beta-lapachone in human carcinoma cells. *Mol. Med.* **1999**, *5*, 232-9.
28. Hanahan, D. The hallmarks of cancer. *Cell* **2000**, *100*, 57-70.
29. Yu, L.; Liu, S. Autophagy contributes to modulating the cytotoxicities of Bcl-2 homology domain-3 mimetics. *Semin. Cancer Biol.* **2013**, *23*, 553-60.

30. Chipuk, J. E.; Moldoveanu, T.; Llambi, F.; Parsons, M. J.; Green, D. R. The BCL-2 family reunion. *Mol. Cell* **2010**, *37*, 299-310.
31. Tait, S. W.; Green, D. R. Mitochondria and cell death: outer membrane permeabilization and beyond. *Nat. Rev. Mol. Cell Biol.* **2010**, *11*, 621-32.
32. Tait, S. W.; Green, D. R. Mitochondria and cell signaling. *J. Cell Sci.* **2012**, *125*, 807-15.
33. Murphy, M. P. How mitochondria produce reactive oxygen species. *Biochem. J.* **2009**, *417*, 1-13.
34. Rigoulet, M.; Yoboue, E. D.; Devin, A. Mitochondrial ROS generation and its regulation: mechanisms involved in H<sub>2</sub>O<sub>2</sub> signaling. *Antioxid. Redox Signal* **2011**, *14*, 459-68.
35. Zorov, D. B.; Juhaszova, M.; Sollott, S. J. Mitochondrial reactive oxygen species (ROS) and ROS-induced ROS release. *Physiol. Rev.* **2014**, *94*, 909-50.
36. Weinberg, S. E.; Chandel, N. S. Targeting mitochondria metabolism for cancer therapy. *Nat. Chem. Biol.* **2015**, *11*, 9-15.
37. Fulda, S.; Galluzzi, L.; Kroemer, G. Targeting mitochondria for cancer therapy. *Nat. Rev. Drug Discov.* **2010**, *9*, 447-64.
38. Nunnari, J.; Suomalainen, A. Mitochondria: in sickness and in health. *Cell.* **2012**, *148*, 1145-59.
39. Twig, G.; Elorza, A.; Molina, A. J.; Mohamed, H.; Wikstrom, J. D.; Walzer, G.; Stiles, L.; Haigh, S. E.; Katz, S.; Las, G.; Alroy, J.; Wu, M.; Py, B. F.; Yuan, J.; Deeney, J. T.; Corkey, B. E.; Shirihai, O. S. Fission and selective fusion govern mitochondrial segregation and elimination by autophagy. *EMBO J.* **2008**, *27*, 433-46.
40. Carracedo, A.; Cantley, L. C.; Pandolfi, P. P. Cancer metabolism: fatty acid oxidation in the limelight. *Nat. Rev. Cancer* **2013**, *13*, 227-32.
41. Vander Heiden, M. G.; Cantley, L. C.; Thompson, C. B. Understanding the Warburg effect: the metabolic requirements of cell proliferation. *Science* **2009**, *324*, 1029-33.
42. Kasahara, A.; Scorrano, L. Mitochondria: from cell death executioners to regulators of cell differentiation. *Trends Cell Biol.* **2014**, *24*, 761-70.
43. Schrepfer, E.; Scorrano, L. Mitofusins, from mitochondria to metabolism. *Mol. Cell* **2016**, *61*, 683-94.

44. Youle, R. J.; van der Bliek, A. M. Mitochondrial fission, fusion, and stress. *Science* **2012**, *337*, 1062-5.
45. Chan, D. C. Fusion and fission: interlinked processes critical for mitochondrial health. *Annu. Rev. Genet.* **2012**, *46*, 265-87.
46. Vyas, S.; Zaganjor, E.; Haigis, M. C. Mitochondria and cancer. *Cell* **2016**, *166*, 555-66.
47. Senft, D.; Ronai, Z. Regulators of mitochondrial dynamics in cancer. *Curr. Opin. Cell Biol.* **2016**, *39*, 43-52.
48. Burté, F.; Carelli, V.; Chinnery, P. F.; Yu-Wai-Man, P. Disturbed mitochondrial dynamics and neurodegenerative disorders. *Nat. Rev. Neurol.* **2015**, *11*, 11-24.
49. Jendrach, M.; Mai, S.; Pohl, S.; Vöth, M.; Bereiter-Hahn, J. Short- and long-term alterations of mitochondrial morphology, dynamics and mtDNA after transient oxidative stress. *Mitochondrion* **2008**, *8*, 293-304.
50. Picard, M.; Shirihai, O. S.; Gentil, B. J.; Burrelle, Y. Mitochondrial morphology transitions and functions: implications for retrograde signaling? *Am. J. Physiol.: Regul., Integr. Comp. Physiol.* **2013**, *304*, R393-R406.
51. Lu, P.; Bruno, B. J.; Rabenau, M.; Lim, C. S. Delivery of drugs and macromolecules to the mitochondria for cancer therapy. *J. Controlled Release* **2016**, *240*, 38-51.
52. Battogtokh, G.; Choi, Y. S.; Kang, D. S.; Park, S. J.; Shim, M. S.; Huh, K. M.; Cho, Y. Y.; Lee, J. Y.; Lee, H. S.; Kang, H. C. Mitochondria-targeting drug conjugates for cytotoxic, anti-oxidizing and sensing purposes: current strategies and future perspectives. *Acta Pharm. Sin. B* **2018**, *8*, 862-80.
53. Lei, E. K.; Kelley, S. O. Delivery and release of small-molecule probes in mitochondria using traceless linkers. *J. Am. Chem. Soc.* **2017**, *139*, 9455-8.
54. Fonseca, S. B.; Pereira, M. P.; Mourrada, R.; Gronda, M.; Horton, K. L.; Hurren, R.; Minden, M. D.; Schimmer, A. D.; Kelley, S. O. Rerouting chlorambucil to mitochondria combats drug deactivation and resistance in cancer cells. *Chem. Biol.* **2011**, *18*, 445-53.
55. Hidaka, T.; Pandian, G. N.; Taniguchi, J.; Nobeyama, T.; Hashiya, K.; Bando, T.; Sugiyama, H. Creation of a synthetic ligand for mitochondrial DNA sequence recognition and promoter-specific transcription suppression. *J. Am. Chem. Soc.* **2017**, *139*, 8444-7.
56. Horton, K. L.; Stewart, K. M.; Fonseca, S. B.; Guo, Q.; Kelley, S. O. Mitochondria-penetrating peptides. *Chem. Biol.* **2008**, *15*, 375-82.

57. He, H.; Wang, J.; Wang, H.; Zhou, N.; Yang, D.; Green, D.; Xu, B. Enzymatic cleavage of branched peptides for targeting mitochondria. *J. Am. Chem. Soc.* **2018**, *140*, 1215-8.
58. Jean, S. R.; Ahmed, M.; Lei, E. K.; Wisnovsky, S. P.; Kelley, S. O. Peptide-mediated delivery of chemical probes and therapeutics to mitochondria. *Acc. Chem. Res.* **2016**, *49*, 1893-902.
59. Yousif, L. F.; Stewart, K. M.; Horton, K. L.; Kelley, S. O. Mitochondria-penetrating peptides: sequence effects and model cargo transport. *Chembiochem* **2009**, *10*, 2081-8.
60. Fulda, S.; Galluzzi, L.; Kroemer, G. Targeting mitochondria for cancer therapy. *Nat. Rev. Drug Discovery* **2010**, *9*, 447-64.
61. Longmire, M. R.; Ogawa, M.; Hama, Y.; Kosaka, N.; Regino, C. A.; Choyke, P. L.; Kobayashi, H. Determination of optimal rhodamine fluorophore for in vivo optical imaging. *Bioconjugate Chem.* **2008**, *19*, 1735-42.
62. Cerrato, C. P.; Pirisinu, M.; Vlachos, E. N.; Langel, Ü. Novel cell-penetrating peptide targeting mitochondria. *FASEB J.* **2015**, *29*, 4589-99.
63. Horobin, R. W.; Trapp, S.; Weissig, V. Mitochondriotropics: a review of their mode of action, and their applications for drug and DNA delivery to mammalian mitochondria. *J. Controlled Release* **2007**, *121*, 125-36.
64. Milane, L.; Trivedi, M.; Singh, A.; Talekar, M.; Amiji, M. Mitochondrial biology, targets, and drug delivery. *J. Controlled Release* **2015**, *207*, 40-58.
65. Jean, S. R.; Tulumello, D. V.; Wisnovsky, S. P.; Lei, E. K.; Pereira, M. P.; Kelley, S. O. Molecular vehicles for mitochondrial chemical biology and drug delivery. *ACS Chem. Biol.* **2015**, *9*, 323-33.
66. Kuntz, E. M.; Baquero, P.; Michie, A. M.; Dunn, K.; Tardito, S.; Holyoake, T. L.; Helgason, G. V.; Gottlieb, E. Targeting mitochondrial oxidative phosphorylation eradicates therapy resistant chronic myeloid leukemia stem cells. *Nature Med.* **2017**, *23*, 1234-40.
67. Moriya K.; Nagatoshi K.; Noriyasu Y.; Okamura T.; Takamitsu E.; Suzuki T.; Utsumi T. Protein N-myristoylation plays a critical role in the endoplasmic reticulum morphological change induced by overexpression of protein Lunapark, an integral membrane protein of the endoplasmic reticulum. *PLoS One* **2013**, *8*, e78235.

68. Liu, X.; Ardizzone, A.; Sui, B.; Anzola, M.; Ventosa, N.; Liu, T.; Veciana, J.; Belfield, K. D. Fluorenyl-loaded quatsome nanostructured fluorescent probes. *ACS Omega*. **2017**, *2*, 4112-22.
69. Fischer, R.; Waizenegger, T.; Köhler, K.; Brock, R. A quantitative validation of fluorophore-labelled cell-permeable peptide conjugates: fluorophore and cargo dependence of import. *Biochim. Biophys. Acta* **2002**, *1564*, 365-74.
70. Wallace, D. C. Mitochondria and cancer. *Nat. Rev. Cancer* **2012**, *12*, 685-98.
71. Westrate, L. M.; Drocco, J. A.; Martin, K. R.; Hlavacek, W. S.; MacKeigan, J. P. Mitochondrial morphological features are associated with fission and fusion events. *PLoS One* **2014**, *9*, e95265.
72. Wong, Y. C.; Ysselstein, D.; Krainc, D. Mitochondria-lysosome contacts regulate mitochondrial fission via RAB7 GTP hydrolysis. *Nature* **2018**, *554*, 382-6.
73. Böckler, S.; Chelius, X.; Hock, N.; Klecker, T.; Wolter, M.; Weiss, M.; Braun, R. J.; Westermann, B. Fusion, fission, and transport control asymmetric inheritance of mitochondria and protein aggregates. *J. Cell Biol.* **2017**, *216*, 2481-98.
74. Miettinen, T. P.; Björklund, M. Mitochondrial function and cell size: an allometric relationship. *Trends Cell Biol.* **2017**, *27*, 393-402.
75. Zhang, Q.; Raoof, M.; Chen, Y.; Sumi, Y.; Sursal, T.; Junger, W.; Brohi, K.; Itagaki, K.; Hauser, C. J. Circulating mitochondrial DAMPs cause inflammatory responses to injury. *Nature* **2010**, *464*, 104-7.
76. Quirós, P. M.; Langer, T.; López-Otín, C. New roles for mitochondrial proteases in health, ageing and disease. *Nat. Rev. Mol. Cell Biol.* **2015**, *16*, 345-9.
77. Youle, R. J.; Narendra, D. P. Mechanisms of mitophagy. *Nat. Rev. Mol. Cell Biol.* **2011**, *12*, 9-14.
78. Voos, W. Mitochondrial protein homeostasis: the cooperative roles of chaperones and proteases. *Res. Microbiol.* **2009**, *160*, 718-25.
79. Wiedemann, N.; Pfanner, N. Mitochondrial machineries for protein import and assembly. *Annu. Rev. Biochem.* **2017**, *86*, 685-714.
80. Chang, J. C.; Wu, S. L.; Hoel, F.; Cheng, Y. S.; Liu, K.H.; Hsieh, M.; Hoel, A.; Tronstad, K. J.; Yan, K. C.; Hsieh, C. L.; Lin, W. Y.; Kuo, S. J.; Su, S. L.; Liu, C. S. Far-infrared radiation protects viability in a cell model of spinocerebellar ataxia by preventing polyQ protein accumulation and improving mitochondrial function. *Sci. Rep.* **2016**, *6*, 304-36.

81. Brand, M. D.; Nicholls, D. G. Assessing mitochondrial dysfunction in cells. *Biochem. J.* **2011**, *435*, 297-312.
82. Pflieger, J.; He, M.; Abdellatif, M. Mitochondrial complex II is a source of the reserve respiratory capacity that is regulated by metabolic sensors and promotes cell survival. *Cell Death Dis.* **2015**, *6*, 1835.
83. Nicholls, D. G. Mitochondrial membrane potential and aging. *Aging Cell.* **2004**, *3*, 35-40.
84. Mookerjee, S. A.; Gerencser, A. A.; Nicholls, D. G.; Brand, M. D. Quantifying intracellular rates of glycolytic and oxidative ATP production and consumption using extracellular flux measurements. *J. Biol. Chem.* **2017**, *292*, 7189-207.
85. Milakovic, T.; Johnson, G. V. Mitochondrial respiration and ATP production are significantly impaired in striatal cells expressing mutant huntingtin. *J. Biol. Chem.* **2005**, *280*, 30773-82.
86. Ong, S. B.; Hausenloy, D. J. Mitochondrial morphology and cardiovascular disease. *Cardiovasc. Res.* **2010**, *88*, 16-29.
87. Su, B.; Wang, X.; Zheng, L.; Perry, G.; Smith, M. A.; Zhu, X. Abnormal mitochondrial dynamics and neurodegenerative diseases. *Biochim. Biophys. Acta* **2010**, *1802*, 135-42.
88. Chen, H.; Chan, D. C. Mitochondrial dynamics in regulating the unique phenotypes of cancer and stem cells. *Cell Metab.* **2017**, *26*, 39-48.
89. Henze, K.; Martin, W. Evolutionary biology: essence of mitochondria. *Nature* **2003**, *426*, 127-8.
90. Pfanner, N.; Warscheid, B.; Wiedemann, N. Mitochondrial proteins: from biogenesis to functional networks. *Nat. Rev. Mol. Cell Biol.* **2019**, *20*, 267-84.
91. Spinelli, J.; Haigis, M. C. The multifaceted contributions of mitochondria to cellular metabolism. *Nat. Cell Biol.* **2018**, *20*, 745-54.
92. Chen, L.B. Mitochondrial membrane potential in living cells. *Annu. Rev. Cell Biol.* **1988**, *4*, 155-81.
93. Gerencser, A. A.; Chinopoulos, C.; Birket, M. J.; Jastroch, M.; Vitelli, C.; Nicholls, D. G.; Brand, M. D. Quantitative measurement of mitochondrial membrane potential in cultured cells: calcium-induced de- and hyperpolarization of neuronal mitochondria. *J. Physiol.* **2012**, *590*, 2845-71.

94. Ward, M. W.; Rego, A. C.; Frenguelli, B. G.; Nicholls, D. G. Mitochondrial membrane potential and glutamate excitotoxicity in cultured cerebellar granule cells. *J. Neurosci.* **2000**, *20*, 7208-19.
95. Momcilovic, M.; Jones, A.; Bailey, S. T.; Waldmann, C. M.; Li, R.; Lee, J. T.; Abdelhady, G.; Gomez, A.; Holloway, T.; Schmid, E.; Stout, D.; Fishbein, M. C.; Stiles, L.; Dabir, D. V.; Dubinett, S. M.; Christofk, H.; Shirihai, O.; Koehler, C. M.; Sadeghi, S.; Shackelford, D. B. In vivo imaging of mitochondrial membrane potential in non-small-cell lung cancer. *Nature* **2019**, *575*, 380–4.
96. Zsurka, G.; Kunz, W. S. Mitochondrial dysfunction and seizures: the neuronal energy crisis. *Lancet Neurol.* **2015**, *14*, 956-66.
97. Knott, A. B.; Perkins, G.; Schwarzenbacher, R.; Bossy-Wetzel, E. Mitochondrial fragmentation in neurodegeneration. *Nat. Rev. Neurosci.* **2008**, *9*, 505-18.
98. Jeon, J. H.; Kim, D. K.; Shin, Y.; Kim, H. Y.; Song, B.; Lee, E. Y.; Kim, J. K.; You, H. J.; Cheong, H.; Shin, D. H.; Kim, S. T.; Cheong, J. H.; Kim, S. Y.; Jang, H. Migration and invasion of drug-resistant lung adenocarcinoma cells are dependent on mitochondrial activity. *Exp. Mol. Med.* **2016**, *48*, e277.
99. Vyas, S.; Zaganjor, E.; Haigis, M. C. Mitochondria and cancer. *Cell* **2016**, *166*, 555-66.
100. Chipuk, J. E.; Bouchier-Hayes, L.; Green, D. R. Mitochondrial outer membrane permeabilization during apoptosis: the innocent bystander scenario. *Cell Death Differ.* **2006**, *13*, 1396-402.
101. Kalkavan, H.; Green, D. R. MOMP, cell suicide as a BCL-2 family business. *Cell Death Differ.* **2018**, *25*, 46-55.
102. Bock, F. J.; Tait, S. W. G. Mitochondria as multifaceted regulators of cell death. *Nat. Rev. Mol. Cell Biol.* **2019**, doi:10.1038/s41580-019-0173-8.
103. Porporato, P. E.; Filigheddu, N.; Pedro, J. M. B.; Kroemer, G.; Galluzzi, L. Mitochondrial metabolism and cancer. *Cell Res.* **2018**, *28*, 265-80.
104. Gama, V.; Deshmukh, M. Life after MOMP. *Mol. Cell* **2015**, *58*, 199-201.
105. Reyna, D. E.; Garner, T. P.; Lopez, A.; Kopp, F.; Choudhary, G. S.; Sridharan, A.; Narayanagari, S. R.; Mitchell, K.; Dong, B.; Bartholdy, B. A.; Walensky, L. D.; Verma, A.; Steidl, U.; Gavathiotis, E. Direct activation of BAX by BTLA1 overcomes apoptosis resistance in acute myeloid leukemia. *Cancer Cell* **2017**, *32*, 490-505.

106. Zheng, H. C. The molecular mechanisms of chemoresistance in cancers. *Oncotarget* **2017**, *8*, 59950–64.
107. Rathore, R.; McCallum, J. E.; Varghese, E.; Florea, A. M.; Büsselberg, D. Overcoming chemotherapy drug resistance by targeting inhibitors of apoptosis proteins (IAPs). *Apoptosis* **2017**, *22*, 898-919.
108. Dai, Y.; Grant, S. BCL2L11/Bim as a dual-agent regulating autophagy and apoptosis in drug resistance. *Autophagy* **2015**, *11*, 416-8.
109. Gottesman, M. M. Mechanisms of cancer drug resistance. *Annu Rev Med.* **2002**, *53*, 615-27.
110. Kesarwani, M.; Kincaid, Z.; Gomaa, A.; Huber, E.; Rohrabough, S.; Siddiqui, Z.; Bouso, M. F.; Latif, T.; Xu, M.; Komurov, K.; Mulloy, J. C.; Cancelas, J. A.; Grimes, H. L.; Azam, M. Targeting c-FOS and DUSP1 abrogates intrinsic resistance to tyrosine-kinase inhibitor therapy in BCR-ABL-induced leukemia. *Nat. Med.* **2017**, *23*, 472-82.
111. Yanez, C. O.; Andrade, C. D.; Belfield, K. D. Characterization of novel sulfonium photoacid generators and their microwave-assisted synthesis. *Chem Commun.* **2009**, *7*, 827-9.
112. Murphy, M. P. Targeting lipophilic cations to mitochondria. *Biochim. Biophys. Acta.* **2008**, *1777*, 1028-31.
113. Zielonka, J.; Joseph, J.; Sikora, A.; Hardy, M.; Ouari, O.; Vasquez-Vivar, J.; Cheng, G.; Lopez, M.; Kalyanaraman, B. Mitochondria-targeted triphenylphosphonium-based compounds: syntheses, mechanisms of action, and therapeutic and diagnostic applications. *Chem. Rev.* **2017**, *117*, 10043-120.
114. De Waele, V.; Hamm, M.; Vergote, T.; Chaumeil, H.; Jin, M.; Malval, J. P.; Baldeck, P.; Poizat, O. Excited-state dynamics of a D- $\pi$ -A type sulfonium-based alkoxystilbene photoacid generator. *Chem. Mater.* **2015**, *27*, 1684-91.
115. Sambath, K.; Zhao, T.; Wan, Z.; Zhang, Y. Photo-uncaging of BODIPY oxime ester for histone deacetylases induced apoptosis in tumor cells. *Chem. Commun.* **2019**, *55*, 14162-5.
116. Trollinger, D. R.; Cascio, W. E.; Lemasters, J. J. Selective loading of rhod-2 into mitochondria shows mitochondrial Ca<sup>2+</sup> transients during the contractile cycle in adult rabbit cardiac myocytes. *Biochem. Biophys. Res. Commun.* **1997**, *236*, 738-742.
117. Wei-LaPierre, L.; Gong, G.; Gerstner, B. J.; Ducreux, S.; Yule, D. I.; Pouvreau, S.; Wang, X.; Sheu, S. S.; Cheng, H.; Dirksen, R. T.; Wang, W. Respective

- contribution of mitochondrial superoxide and pH to mitochondria-targeted circularly permuted yellow fluorescent protein (mt-cpYFP) flash activity. *J. Biol. Chem.* **2013**, *288*, 10567-77.
118. Balut, C.; vandeVen, M.; Despa, S.; Lambrichts, I.; Ameloot, M.; Steels, P.; Smets, I. Measurement of cytosolic and mitochondrial pH in living cells during reversible metabolic inhibition. *Kidney Int.* **2008**, *73*, 226-32.
119. Żurawik, T. M.; Pomorski, A.; Belczyk-Ciesielska, A.; Goch, G.; Niedźwiedzka, K.; Kucharczyk, R.; Krężel, A.; Bal, W. Revisiting mitochondrial pH with an improved algorithm for calibration of the ratiometric 5(6)-carboxy-SNARF-1 probe reveals anticooperative reaction with H<sup>+</sup> ions and warrants further studies of organellar pH. *PLoS One* **2016**, *11*, e0161353.
120. Lemasters, J. J.; Nieminen, A. L.; Qian, T.; Trost, L. C.; Herman, B. The mitochondrial permeability transition in toxic, hypoxic and reperfusion injury. *Mol. Cell Biochem.* **1997**, *174*, 159-65.
121. Lee, S. Y.; Cho, H. J. Mitochondria targeting and destabilizing hyaluronic acid derivative-based nanoparticles for the delivery of lapatinib to triple-negative breast cancer. *Biomacromolecules* **2019**, *20*, 835-45.
122. Santo-Domingo, J.; Demaurex, N. Perspectives on: SGP symposium on mitochondrial physiology and medicine: the renaissance of mitochondrial pH. *J. Gen. Physiol.* **2012**, *139*, 415-23.
123. Archer, S. L. Mitochondrial dynamics--mitochondrial fission and fusion in human diseases. *N. Engl. J. Med.* **2013**, *369*, 2236-51.
124. Suen, D. F.; Norris, K. L.; Youle, R. J. Mitochondrial dynamics and apoptosis. *Genes Dev.* **2008**, *22*, 1577-90.
125. Yang, J. L.; Mukda, S.; Chen, S. D. Diverse roles of mitochondria in ischemic stroke. *Redox Biol.* **2018**, *16*, 263-75.
126. Perfettini, J. L.; Roumier, T.; Kroemer, G. Mitochondrial fusion and fission in the control of apoptosis. *Trends Cell Biol.* **2005**, *15*, 179-83.
127. Matsuura, K.; Canfield, K.; Feng, W.; Kurokawa, M. Metabolic regulation of apoptosis in cancer. *Int. Rev. Cell Mol. Biol.* **2016**, *327*, 43-87.
128. Hüttemann, M.; Pecina, P.; Rainbolt, M.; Sanderson, T. H.; Kagan, V. E.; Samavati, L.; Doan, J. W.; Lee, I. The multiple functions of cytochrome c and their regulation in life and death decisions of the mammalian cell: From respiration to apoptosis. *Mitochondrion* **2011**, *11*, 369-81.

129. Garrido, C.; Galluzzi, L.; Brunet, M.; Puig, P. E.; Didelot, C.; Kroemer, G. Mechanisms of cytochrome c release from mitochondria. *Cell Death Differ.* **2006**, *13*, 1423-33.
130. Begleiter, A.; Mowat, M.; Israels, L. G.; Johnston, J. B. Chlorambucil in chronic lymphocytic leukemia: mechanism of action. *Leuk. Lymphoma* **1996**, *23*, 187-201.
131. Panasci, L.; Paiement, J. P.; Christodoulouopoulos, G.; Belenkov, A.; Malapetsa, A.; Aloyz, R. Chlorambucil drug resistance in chronic lymphocytic leukemia: the emerging role of DNA repair. *Clin. Cancer Res.* **2001**, *7*, 454-61.
132. Green, D. R.; Kroemer, G. The pathophysiology of mitochondrial cell death. *Science* **2004**, *305*, 626-9.
133. Fonseca, S. B.; Pereira, M. P.; Mourtada, R.; Gronda, M.; Horton, K. L.; Hurren, R.; Minden, M. D.; Schimmer, A. D.; Kelley, S. O. Rerouting chlorambucil to mitochondria combats drug deactivation and resistance in cancer cells. *Chem. Biol.* **2011**, *18*, 445-53.
134. Morrow, C. S.; Smitherman, P. K.; Diah, S. K.; Schneider, E.; Townsend, A. J. Coordinated action of glutathione S-transferases (GSTs) and multidrug resistance protein 1 (MRP1) in antineoplastic drug detoxification. Mechanism of GST A1-1- and MRP1-associated resistance to chlorambucil in MCF7 breast carcinoma cells. *J. Biol. Chem.* **1998**, *273*, 20114-20.
135. Ellis-Davies, G. C. Caged compounds: photorelease technology for control of cellular chemistry and physiology. *Nat. Methods* **2007**, *4*, 619-28.
136. Yu, H.; Li, J.; Wu, D.; Qiu, Z.; Zhang, Y. Chemistry and biological applications of photo-labile organic molecules. *Chem. Soc. Rev.* **2010**, *39*, 464-73.
137. Venkatesh, Y.; Rajesh, Y.; Karthik, S.; Chetan, A. C.; Mandal, M.; Jana, A.; Singh, N. D. Photocaging of single and dual (similar or different) carboxylic and amino acids by acetyl carbazole and its application as dual drug delivery in cancer therapy. *J. Org. Chem.* **2016**, *81*, 11168-75.
138. Klan, P.; Solomek, T.; Bochet, C. G.; Blanc, A.; Givens, R.; Rubina, M.; Popik, V.; Kostikov, A.; Wirz, J. Photoremovable protecting groups in chemistry and biology: reaction mechanisms and efficacy. *Chem. Rev.* **2013**, *113*, 119-91.
139. Loudet, A.; Burgess, K. BODIPY dyes and their derivatives: syntheses and spectroscopic properties. *Chem. Rev.* **2007**, *107*, 4891-932.
140. Raymo, F. M. Photoactivatable synthetic fluorophores. *Phys. Chem. Chem. Phys.* **2013**, *15*, 14840-50.

141. Umeda, N.; Takahashi, H.; Kamiya, M.; Ueno, T.; Komatsu, T.; Terai, T.; Hanaoka, K.; Nagano, T.; Urano, Y. Boron dipyrromethene as a fluorescent caging group for single-photon uncaging with long-wavelength visible light. *ACS Chem. Biol.* **2014**, *9*, 2242-6.
142. Kawatani, M.; Kamiya, M.; Takahashi, H.; Urano, Y. Factors affecting the uncaging efficiency of 500 nm light-activatable BODIPY caging group. *Bioorg. Med. Chem. Lett.* **2018**, *28*, 1-5.
143. Goswami, P. P.; Syed, A.; Beck, C. L.; Albright, T. R.; Mahoney, K. M.; Unash, R.; Smith, E. A.; Winter, A. H. *J. Am. Chem. Soc.* **2015**, *137*, 3783-6.
144. Peterson, J. A.; Wijesooriya, C.; Gehrman, E. J.; Mahoney, K. M.; Goswami, P. P.; Albright, T. R.; Syed, A.; Dutton, A. S.; Smith, E. A.; Winter, A. H. Family of BODIPY photocages cleaved by single photons of visible/near-infrared light. *J. Am. Chem. Soc.* **2018**, *140*, 7343-6.
145. Slanina, T.; Shrestha, P.; Palao, E.; Kand, D.; Peterson, J. A.; Dutton, A. S.; Rubinstein, N.; Weinstain, R.; Winter, A. H.; Klan, P. In search of the perfect photocage: structure-reactivity relationships in meso-methyl BODIPY photoremovable protecting groups. *J. Am. Chem. Soc.* **2017**, *139*, 15168-75.
146. Rubinstein, N.; Liu, P.; Miller, E. W.; Weinstain, R. meso-Methylhydroxy BODIPY: a scaffold for photo-labile protecting groups. *Chem. Commun.* **2015**, *51*, 6369-72.
147. Kand, D.; Pizarro, L.; Angel, I.; Avni, A.; Friedmann-Morvinski, D.; Weinstain, R. Organelle-targeted BODIPY photocages: visible-light-mediated subcellular photorelease. *Angew. Chem. Int. Ed.* **2019**, *58*, 4659-63.
148. Sitkowska, K.; Feringa, B. L.; Szymanski, W. Green-light-sensitive BODIPY photoprotecting groups for amines. *J. Org. Chem.* **2018**, *83*, 1819-27.
149. Stacko, P.; Muchova, L.; Vitek, L.; Klan, P. Visible to NIR light photoactivation of hydrogen sulfide for biological targeting. *Org. Lett.* **2018**, *20*, 4907-11.
150. Hwu, J. R.; Tsay, S.-C.; Hong, S. C.; Leu, Y.-J.; Liu, C.-F.; Chou, S.-S. P. Oxime esters of anthraquinone as photo-induced DNA-cleaving agents for single- and double-strand scissions. *Tetrahedron Lett.* **2003**, *44*, 2957-60.
151. Hwu, J. R.; Yang, J.-R.; Tsay, S.-C.; Hsu, M.-H.; Chen, Y.-C.; Chou, S.-S. P. Photo-Induced DNA cleavage by (heterocyclo)carbonyl oxime esters of anthraquinone. *Tetrahedron Lett.* **2008**, *49*, 3312-5.
152. Fast, D. E.; Lauer, A.; Menzel, J. P.; Kelterer, A.-M.; Gescheidt, G.; Barner-Kowollik, C. Wavelength-dependent photochemistry of oxime ester photoinitiators. *Macromolecules* **2017**, *50*, 1815-23.

153. Chowdhury, N.; Dutta, S.; Dasgupta, S.; Singh, N. D.; Baidya, M.; Ghosh, S. K. Synthesis, photophysical, photochemical, DNA cleavage/binding and cytotoxic properties of pyrene oxime ester conjugates. *Photochem. Photobiol. Sci.* **2012**, *11*, 1239-50.
154. Chiu, C. T.; Wang, Z.; Hunsberger, J. G.; Chuang, D. M. Therapeutic potential of mood stabilizers lithium and valproic acid: beyond bipolar disorder. *Pharmacol. Rev.* **2013**, *65*, 105-42.
155. Felix, F.; Fontenele, J. Valproic acid may be tested in patients with H3F3A-mutated high-grade gliomas. *J. Clin. Oncol.* **2016**, *34*, 3104-5.
156. Ji, M. M.; Wang, L.; Zhan, Q.; Xue, W.; Zhao, Y.; Zhao, X.; Xu, P. P.; Shen, Y.; Liu, H.; Janin, A.; Cheng, S.; Zhao, W. L. Induction of autophagy by valproic acid enhanced lymphoma cell chemosensitivity through HDAC-independent and IP3-mediated PRKAA activation. *Autophagy* **2015**, *11*, 2160-71.
157. Tomson, T.; Battino, D.; Perucca, E. Valproic acid after five decades of use in epilepsy: time to reconsider the indications of a time-honoured drug. *Lancet Neurology* **2016**, *15*, 210-8.
158. Duenas-Gonzalez, A.; Candelaria, M.; Perez-Plascencia, C.; Perez-Cardenas, E.; de la Cruz-Hernandez, E.; Herrera, L. A. Valproic acid as epigenetic cancer drug: preclinical, clinical and transcriptional effects on solid tumors. *Cancer Treat. Rev.* **2008**, *34*, 206-22.
159. Emrullahoglu, M.; Ucuncu, M.; Karakus, E. A BODIPY aldoxime-based chemodosimeter for highly selective and rapid detection of hypochlorous acid. *Chem. Commun.* **2013**, *49*, 7836-8.
160. Liu, T.; Liu, X.; Wang, W.; Luo, Z.; Liu, M.; Zou, S.; Sissa, C.; Painelli, A.; Zhang, Y.; Vengris, M.; Bondar, M. V.; Hagan, D. J.; Van Stryland, E. W.; Fang, Y.; Belfield, K. D. Systematic molecular engineering of a series of aniline-based squaraine dyes and their structure-related properties. *J. Phys. Chem. C* **2018**, *122*, 3994-4008.
161. Valentini, A.; Biancolella, M.; Amati, F.; Gravina, P.; Miano, R.; Chillemi, G.; Farcomeni, A.; Bueno, S.; Vespasiani, G.; Desideri, A.; Federici, G.; Novelli, G.; Bernardini, S. Valproic acid induces neuroendocrine differentiation and UGT2B7 up-regulation in human prostate carcinoma cell line. *Drug Metab. Dispos.* **2007**, *35*, 968-72.
162. Phiel, C. J.; Zhang, F.; Huang, E. Y.; Guenther, M. G.; Lazar, M. A.; Klein, P. S. Histone deacetylase is a direct target of valproic acid, a potent anticonvulsant, mood stabilizer, and teratogen. *J. Biol. Chem.* **2001**, *276*, 36734-41.

163. Chen, J.; Ghazawi, F. M.; Bakkar, W.; Li, Q. Valproic acid and butyrate induce apoptosis in human cancer cells through inhibition of gene expression of Akt/protein kinase B. *Mol. Cancer*. **2006**, *5*, 71.